東北大学機関リポジトリ
TOUR
Tohoku University Repository

Angular Measurement Based on Second Harmonic Generation

著者	Astuti Wijayanti Dwi
学位授与機関	Tohoku University
URL	http://hdl.handle.net/10097/00137510

博 士 学 位 論 文

Doctoral Thesis

論文題目

Thesis Title

Angular Measurement Based on Second Harmonic Generation

東北大学大学院工学研究科

Graduate School of Engineering,

TOHOKU UNIVERSITY

専攻/Department: Finemechanics

氏名/Name: Wijayanti Dwi ASTUTI

TOHOKU UNIVERSITY
Graduate School of Engineering

Angular Measurement Based on Second Harmonic Generation

（第二高調波発生を用いた角度計測に関する研究）

A dissertation submitted for the degree of Doctor of Philosophy (Engineering)

Department of Finemechanics

by

Wijayanti Dwi ASTUTI

July 6, 2022

Angular Measurement Based on Second Harmonic Generation

Wijayanti Dwi ASTUTI

Abstract

Angle is one of the fundamental parameters in many sectors, especially in manufacturing, for the quality controller of items or products. The research on angle sensors is continuously being developed with the increasing need for real-time, high precision, and high sensitivity measurement. Various studies have been carried out to improve the performance of angle sensors, including research on conventional angle sensors. However, the angle-sensing technology is still challenging to meet the need for current trends in technology that lead to the manufacturing of high-complexity products yet shrinking in dimensions. It requires a suitable angle sensor that is not limited by the type of material being measured, has minimal potential damage to the material during the measurement process, and is expected to have minimal maintenance costs. These reasons encourage more intensive research on new angle measurement methods, especially non-contact angle sensors, as the solution to bridge these problems.

A second harmonic wave (SHW) angle sensor offers a well-suited measurement configuration system to satisfy the aforementioned requirements. The second harmonic generation (SHG) is a phenomenon in which the optical wave source passes through a nonlinear optical material and generates an SHW with frequency-doubled that depends on the wavelength and the incident angle of the source toward the nonlinear material. The applications of SHG have been widely reported. However, the use of SHG in angle sensors is a new implementation. Therefore, this dissertation presents the angular measurement based on SHG and confirms the feasibility of the proposed angle sensor.

Chapter 1 describes the background and motivations of this research related to the angle sensor development and the explanation of the challenging problem in angular measurement that cannot be solved by using the conventional angle sensor.

Chapter 2 presents a proposal for an SHG-based angle sensor where the basic concepts and the implementation of SHG in angle sensors are introduced. Several requirements must be met to apply the SHG as an angle sensor, including selecting an adequate laser source, using a nonlinear optical crystal (NLO) with suitable characteristics, and considering the condition of the crystal phase-matching angle. To implement SHG as an angle sensor, a laser source with a wide-angle range and sufficient power is required, which tends to be high power. These characteristics can be obtained using a femtosecond (Fs) laser. Since the angle matching condition occurs at a certain angle for the specific wavelength indicated by the peak in the observed SHG spectrum, by using Fs laser as the laser source, the phase-matching conditions can occur at many angular positions of the crystal. If the matching angle is changed by rotating the NLO crystal, the peak of the SHG spectrum will also change. The characteristic of the SHG spectral peak shows the measurement trend of the angle sensor, which can be estimated theoretically. It should be noted that the negative uniaxial NLO crystals are the type of crystal that is employed in the angle sensor configuration due to the birefringence characteristic. In this chapter, BBO, $LiIO_3$, and $MgO:LiNbO_3$ crystals are theoretically evaluated. Calculations show that for a wavelength range from 1480 nm to 1640 nm, BBO, $LiIO_3$, and $MgO:LiNbO_3$ crystals have an angle dispersion of 0.08° between 19.85° and 19.93°, 1.50° between 20.55° and 22.05°, and 2.87° between 48.50° and 51.37°, respectively. These characteristics are used in selecting the appropriate NLO crystal for the angle sensor configuration.

Chapter 3 describes the proposal of an intensity-dependent SHG angle sensor. Through the theoretical calculation, the BBO crystal is suitable for this purpose. The feasibility of the proposed angle sensor is demonstrated experimentally by focusing the laser beam into the crystal using lens. It has been demonstrated theoretically and experimentally that a focused Fs laser is effective in realizing SHG-based angle measurement for an Fs laser source with relatively small output power. The angle detection is carried out by observing the change in SHG intensity response over the change in angular position of the BBO crystal. The sensitivity observed in the experiments is lower than the theoretical calculation. Investigations have been carried out based on ray tracing to clarify the reason for the discrepancy. It has been clarified that chromatic aberration has been present where the

shorter focal length of the focusing lens has made the influence of chromatic aberration stronger, made the effective crystal length shorter, and resulted in the degradation of the sensitivity.

Chapter 4 describes a proposed method of measuring high-precision angles in wavelength-dependent based on the SHG. The characteristics of the SHG in a certain wavelength range are associated with the angular shift of the NLO crystal representing the measurement target. The proposed angle sensor provides absolute angle measurement by relying on the evolution of the SHG spectral peaks upon changes in the angular position of the crystal. For this reason, NLO crystals with a wide phase matching dispersion angle are required, and MgO:$LiNbO_3$ is a suitable crystal to meet the need. Theoretical calculations estimate the measurement trend using a wave-plane approximation scheme. In the experiment, a focused Fs laser was demonstrated using a parabolic mirror to overcome the problem of chromatic aberration that arises when the lens is used. As a result, a measured range of ~20000 arcseconds and a measurement resolution of 3.03 arcseconds have been achieved. It is also explained that the difference in refractive index between air and nonlinear optical crystals must be considered because it has been proven to cause differences between theoretical calculations and experimental results.

Chapter 5 describes the optimization of the wavelength-dependent SHG angle sensor. A new configuration is proposed using the collimated beam of the Fs laser with a higher power. The angle detection is demonstrated by identifying the SHG spectrum peaks against the angular position of the rotating stage-mounted MgO:$LiNbO_3$ crystal representing the measurement object. The MgO:$LiNbO_3$ is rotated within the phase-matching angle over a range of 1480 nm to 1640 nm. Angle measurement is also carried out by placing the crystal at different positions along the laser beam propagation direction to confirm the feasibility of the angle sensor, where the measurement range, sensitivity, and resolution of the proposed method are also evaluated. The result shows that the proposed angle sensor can overcome the working distance limitation of conventional angle sensors and has no specific material target requirement. Since the configuration of the proposed angle sensor is not limited by the specification of the measurement target, it is expected to have wide potential applications, especially in the manufacturing process and inspection process.

Chapter 6 contains the conclusions of the research and shows the publication reports achieved within the research.

Keywords: angular measurement, second harmonic generation (SHG), phase-matching, birefringent, femtosecond laser (Fs laser), intensity-dependent angular measurement, wavelength-dependent angular measurement, BBO, MgO:$LiNbO_3$.

Contents

Chapter 3: The design and construction of intensity-dependent second harmonic generation angle sensor

Chapter 4: High-precision wavelength-dependent SHG angle detection

Chapter 5: Optimization of wavelength-dependent SHG angle sensor

Chapter 6: Conclusion

List of Figures

List of Table

Nomenclature

Abbreviations

FW	Fundamental wave
Fs	Femtosecond
NLO	Nonlinear optical
SHG	Second harmonic generation
SHW	Second harmonic wave

List of Symbols

$\mathbf{P}$	Polarization
$\mathbf{E}$	Electric field vector
μ_0	Permeability of the free space
σ	Conductivity
ε_0	Vacuum permittivity
c	Speed of light in vacuum
$\mathbf{r}$	Vector position
t	Time
ω	Angular frequency
I_ω	Intensity of fundamental wave
n	Refractive index
$\mathbf{P}_{2\omega}^{\mathrm{NL}}$	Nonlinear polarization
d_{eff}	Scalar effective nonlinear coefficient
E_ω	Scalar electric field of fundamental wave
$E_{2\omega}$	Scalar electric field of second harmonic wave
L	Length of crystal
$\boldsymbol{k}$	Wave vector
k	Wave number

Δk	Phase mismatching
k_ω ; k_1	Wave number of fundamental wavelength
$k_{2\omega}$; k_2	Wave number of fundamental wavelength
λ_ω ; λ_1	Fundamental wavelength
$\lambda_{2\omega}$; λ_2	Second harmonic wavelength
I_ω	Intensity of fundamental wave
$I_{2\omega}$	Intensity of second harmonic generation
p_ω ; p	Power of fundamental wave
$p_{2\omega}$; p'	Power of second harmonic generation
η	SHG efficiency
n_e ; N_e	Refractive index of extraordinary ray
n_o	Refractive index of ordinary ray
θ_m	Angle of phase matching
ϕ	Azimuthal angle of crystal
w_0	Beam spot radius
$w(z)$	Beam radius at z
f	Focal length of lenses/ off-axis parabolic mirror
d	Diameter of a collimated laser beam made incident to an objective lens/ off-axis parabolic mirror
b	Rayleigh length
ξ	Ration of nonlinear crystal length to the focal length or the parameter of focusing
μ	Relative position of focus inside the crystal
z_0	Coordinate of the minimum beam radius
s	Variable of integration
ρ	Walk-off angle

Chapter 1
Introduction

1.1 Background

1.1.1 Angle sensors in general

The angle is one of the fundamental parameters that determine the geometry of an object [1]. Angle measurement is thus very important for manufacturing and construction development [2] because it is a critical piece of equipment in the industry, especially for design, assembly, and quality control. In general, angle sensing technology is classified considering the method, field of application target, and sensor performance that accommodate the purpose of the measurement to the specific target. The angle sensors can also be classified into contact and contactless types according to the measurement principle and purpose [3]. Recently, the demand for angle sensors is increasing to fit the requirement of real-time, high precision, high sensitivity measurement, large range of angle, and high measurement resolution [4–6]. It is also important to have certain advantages of angle sensors, such as being easy to use and

having a minimum maintenance cost [7,8]. By this consideration, contactless angle measurement is a suitable method for implementing such an application.

Talking about contactless angle sensors, there are numerous methods in which an angle displacement can be measured, such as capacitive angle sensors [9–11], inductive angle sensors [12,13], Hall effect-based and magneto-resistance (MR) angle sensors [14,15], and optical angle sensor [16–18]. A capacitive angle sensor converts a change in angular displacement of the dielectric material into an electrical signal, whereas the contactless capacitive absolute angular-position sensor has a full-circle range of 360°. Most reported capacitive angular sensors employ disk-shaped electrodes, which are mounted parallelly on the shaft, as seen in Figure 1.1. This type of geometry can be used in applications where the available lateral space is limited, for example, the steering wheel sensor. However, this type of angle sensor has a major issue associated with its low performance in adverse environmental conditions, such as moisture, dust, oil, misalignments, and mechanical vibrations. Moreover, this type of angle sensor is unsuitable for measuring a very small shift of angular position [19].

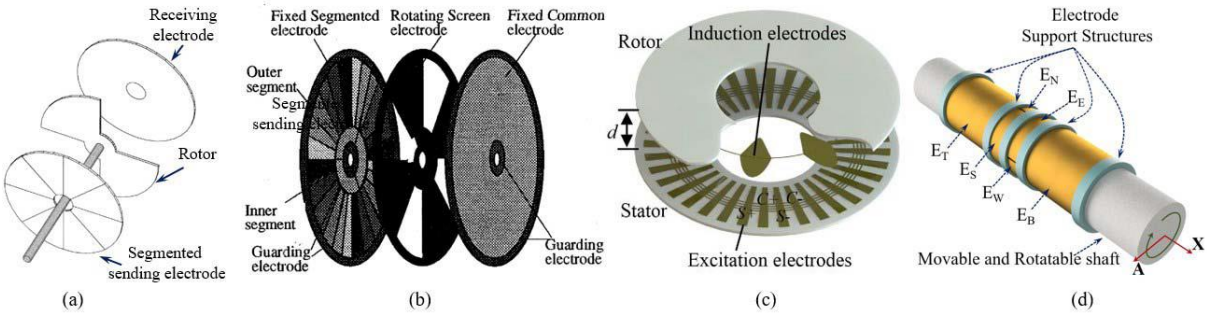

Figure 1.1 Capacitance based angle sensors. (a) a three-electrode capacitive angle sensor [20]. (b) modified configuration with a segmented electrode is composed of 24 outer segment and 3 inner segments [21]. (c) time-grating based angle sensor [22]. (d) structural model of a cylindrical capacitive sensor suitable for the combined measurement of angular and linear displacement [23].

The inductive angle sensor uses an inductor to generate a high-frequency magnetic field. When the measured metal object is placed near the inductor, the object induces a current, which reduces the amplitude of the original magnetic field. Therefore, the

inductive sensor can determine the displacement of the object being measured. Figure 1.2 shows several inductive angle sensors based on the reported magnetic fields. However, this type of sensor has limitations because most of the existing magnetic resistance-based angle sensors require permanent magnets in rotating parts, require large power requirements, and are sensitive to external disturbances.

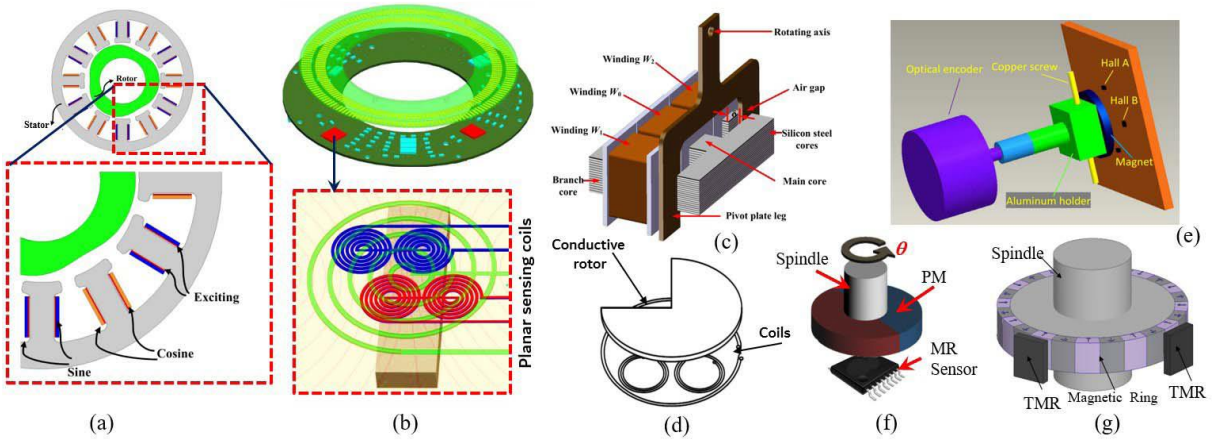

Figure 1.2 Inductive angle sensors. (a)-(d) represent popular inductive and eddy current sensors and (e)-(g) show magnetic resistance and Hall effect-based angle sensors. (a) the permanent magnet resolver [24]. (b) planar coil based absolute magnetic rotary sensor [25]. (c) eddy current sensor for small angle measurement [26]. (d) Planar coil-based eddy current sensor [27]. (e) angle sensor based on four hall elements [28]. (f) basic structure of a typical magnetic resistor-based angle sensor. (g) time-grating magnetic encoder [29].

Another type of noncontact angle sensor is the optical-based angle sensor that works with the principle of measuring the physical quantity of light and translating it into the readable form of the instrument. Compared with inductive and magnetic resistance-based angle sensors, optical sensors are highly immune to magnetic interferences and are well accepted owing to their ability to measure angular position in a noncontact way with high accuracy and excellent resolution. As a comparison, Figure 1.3 shows the resolution of several angle measurement methods. The optical angle sensor can achieve a resolution of ~(10–5)°, making this angle measurement method suitable for measuring a very small angular displacement.

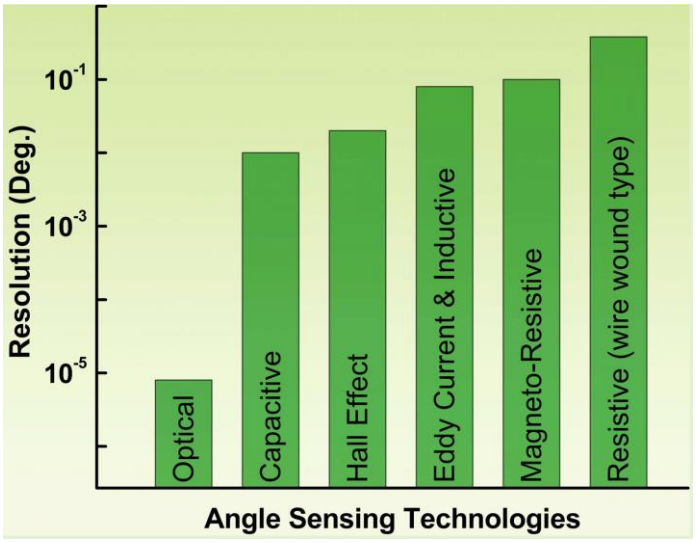

Figure 1.3 The resolution comparison of several angle measurement method [19].

In recent years, precision small-angle measurement based on optically principle has been extensively used in different fields, such as the semiconductor industry, precision machinery industry, surface profile, measuring instrument calibration, and precision motion monitoring [30]. Several optical angle sensors are widely employed for angular displacement detection because they provide high measurement sensitivity, high resolution, and high accuracy. The angle measurement methods and techniques based on optical principles can be divided into autocollimation and interference methods. The measurement technique in each optical angle sensor has developed with its own merits. For example, the commercial autocollimator can be applied to dynamic or static small-angle detection, precision alignment, verification of angle standards, and various other processes. The autocollimator employs a planar mirror as angle-sensitive that is mounted on a moving stage and uses light reflection as the basic principle. During the measurement, a collimated light beam from the autocollimator is projected onto the planar mirror. The reflected light beam from the mirror is received by the autocollimator unit composed of a collimator objective and a two-directional light position-sensing detector. The conventional autocollimator can detect the pitch and yaw angle by detecting the X- and Y-directional linear displacements of the light spot on the detector. Figure 1.4 shows the schematic of the pitch and yaw (XY-direction) angle measurement system in an autocollimator where

the pitch and yaw of the mirror (SCM) are denoted as α and β. If there is a change in the pitch and yaw position of the mirror, the pitch and yaw angle of the mirror can be expressed as

$$\sin 2\alpha = \frac{\Delta x_1}{f} \quad . \tag{1.1}$$

$$\sin 2\beta = \frac{\Delta y_1}{f} \tag{1.2}$$

Where f is the focal length of lens 1 in the figure, and Δx_1 and Δy_1 are the light spot deviation on the position sensing detection 1 (PSD1) along with the horizontal and vertical directions, respectively.

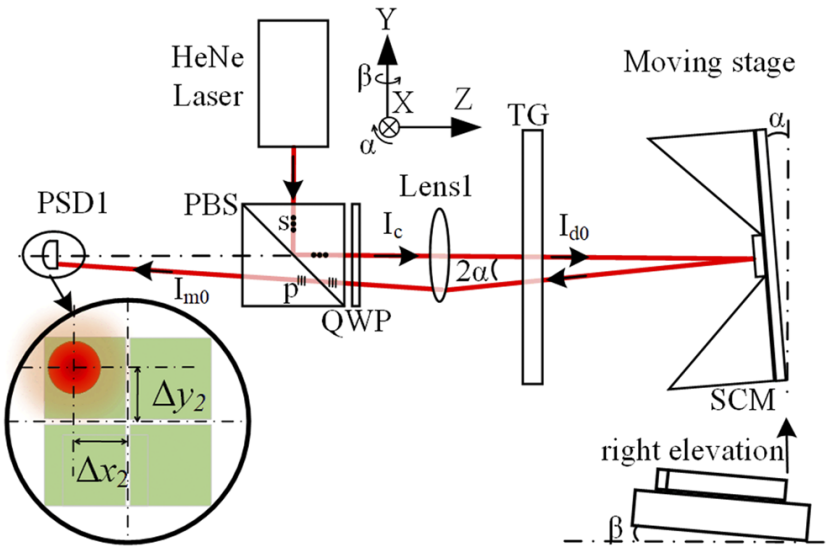

Figure 1.4 The schematic of pitch and yaw angle measurement in autocollimator system [30].

The reflected beam from the plane mirror in the traditional autocollimator does not respond to the roll angle (Z-direction). Numerous reports have proposed a new design of autocollimator in order to detect three-axial angular displacement [31,32]. Figure 1.5 shows the schematic of the three-axis autocollimator system that has been reported in [30].

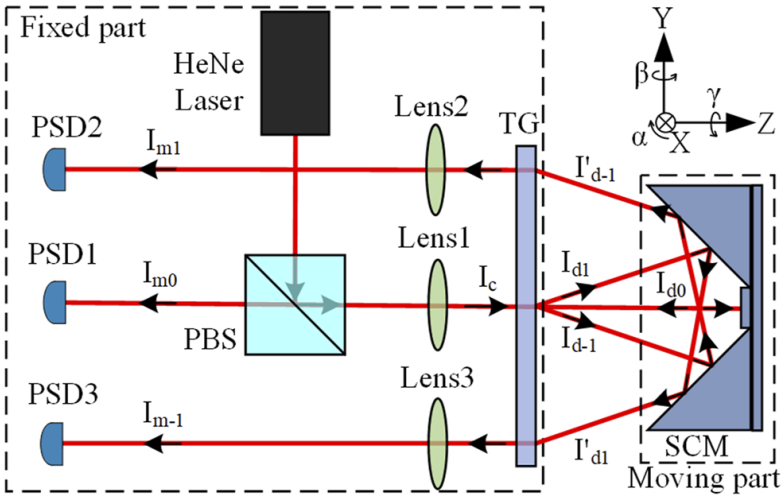

Figure 1.5 The schematic of three-axis autocollimator system [30].

According to various effects, the angular displacement sensing systems have been reported, including the total internal reflection, surface plasmon resonance, two-beam interference, multi-beam interference, and birefringence effects. These sensing systems can convert the angular displacement information into the optical phase variation, which can be detected using the optical interferometer. The high sensitivity of the angular sensing system integrated with the interferometer can offer a high measurement resolution for the angular displacement.

The birefringence effect is a new preference effect to be used as the angle sensor. The variation of the phase difference between the two orthogonal polarization states of the light beam is a function of the birefringence, propagation distance, and direction of the light beam in the birefringent crystal. Therefore, suitable crystal thickness and birefringence can be selected to build an angular sensing system with a large measurement range and high sensitivity. According to the birefringence effect, an angular displacement sensor with high sensitivity and a large measurement range was developed in ref. [6]. The sensor consisted of two prisms and a calcite plate, and it was designed as a sandwich, as shown schematically in Figure 1.6. The heterodyne interferometry was used to detect the phase variation resulting from the angle sensor. The angular displacement could be determined according to the birefringence characteristics of the sensor and the measured phase variation. Based on the

experimental results, the system retained a maximum measurement range. The experimental results demonstrate that our proposed method can be used to measure long-range angular displacement with high resolution while maintaining high system stability. Furthermore, these results show that the measurement resolution and speed can reach 2° × 10−4 and 2°/s, respectively.

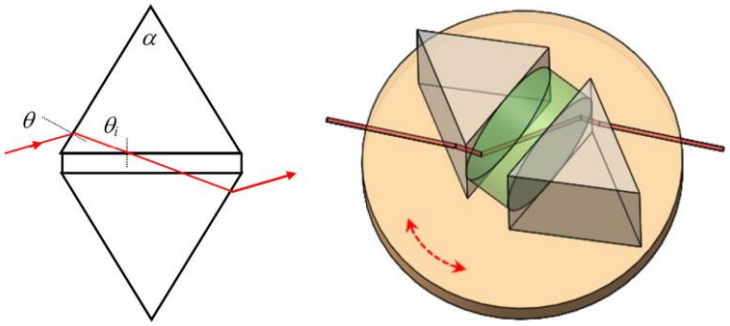

(a)

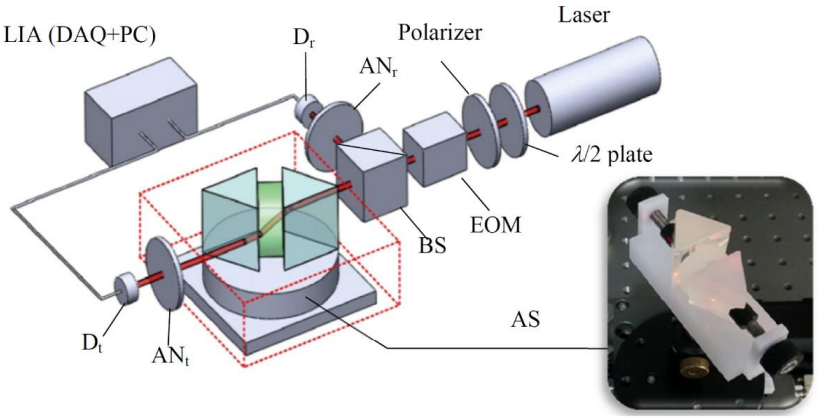

(b)

Figure 1.6 (a) Schematic diagram of the angular sensor; (b) Relationship between the phase difference and incident angle (θ) with different refractive indices (np) of the equilateral triangle prism [6].

1.1.2 Second harmonic generation in general measurement applications

Second-harmonic generation (SHG) is a phenomenon of the nonlinear optic from a fundamental laser beam discovered by Franken et al. in 1961 [33]. They found light at doubled frequency was generated from the interaction of a strong laser beam with

the nonlinear medium (quartz crystal). This optical phenomenon has been used for various applications. First, it can be used to characterize short and ultrashort pulsed lasers. Dantzig et al. proposed an organic salt dimethylamino-4-N-methylstilbazolium tosylate (DAST) to generate the second harmonic of pulses in the far-infrared region (30-55 μm) in order to characterize ultrashort in a spectral region where no other materials are available [34]. Panda et al. showed that SHG in ZnO nanorods could be used to characterize ultrashort pulse, as its schematic diagram is shown in Figure 1.7 [35]. The experimental result showed that the measured pulse width closely matches with theoretically predicted pulse width. Therefore, the reported characterization system is cost-effective and can be used to characterize fs laser of the broad wavelength range. Li yanyan et al. demonstrated that ultrashort mid-infrared laser pulse could be accurately characterized using a second harmonic generation frequency-resolved optical gating apparatus [36]. The result showed that a mid-infrared pulse at 3580 nm was measured with a good agreement between the retrieved and measured spectrum. This provided a reliable tool for developing the potential applications of these long-wavelength laser sources.

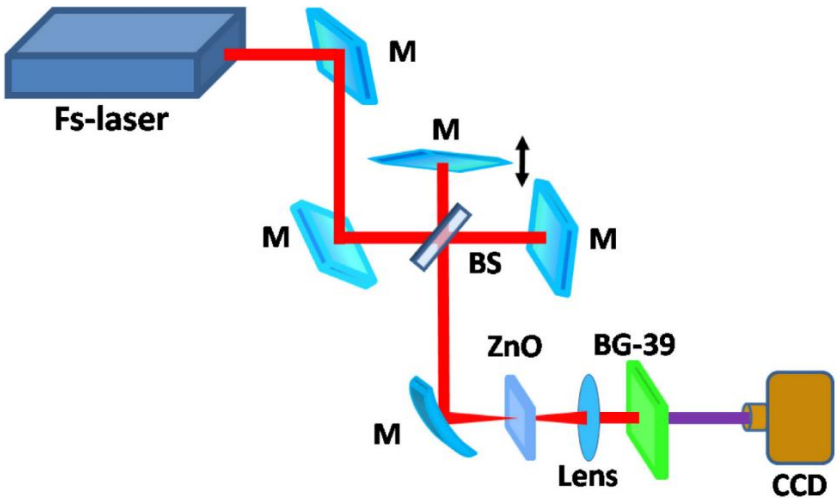

Figure 1.7 Schematics of the experimental setup used for pulse characterization of fs pulses using SHG of ZnO nanorods proposed by Panda et al [35].

Another application of SHG is for surface characterization. Ionica et al. proposed a technique to characterize dielectric semiconductor interfaces used in

microelectronics and photovoltaics using SHG, as shown in Figure 1.8 [37]. The result shows that this technique is nondestructive and well adapted for thin-film testing. Also, it was perfectly accommodated to study charging and discharging dynamics in dielectric/silicon stacks. Lüpke demonstrated second harmonic generation to characterize semiconductor interfaces [38]. Specifically, Si/SiO2 interfaces have been studied to understand the sensitivity of SHG to interface defects, steps, strain, roughness, electric fields, carrier dynamics, and chemical modifications. Vanbel et al. presented SHG as a characterization tool for Ge/high-k dielectric interfaces [39], whereas Nakamura et al. introduced in-situ surface and interface characteristics by optical SHG of silicon dioxide fabrication with high purity ozone [40].

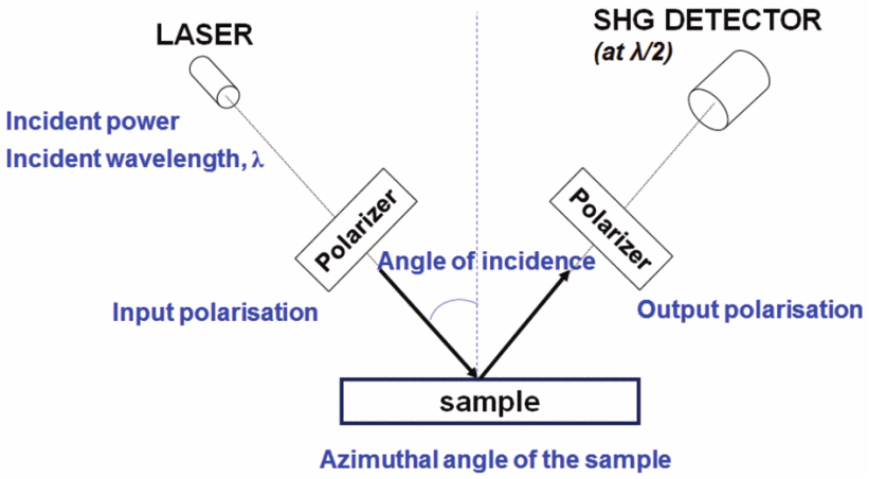

Figure 1.8 Schematic of the experimental configuration for SHG measurement, with the key parameters reported by Ionica et al [37].

The second Hamonic Generation also can be used in image sensing techniques called SHG microscopy (shown in Figure 1.9), which is a powerful tool for imaging fibrillar collagen in a diverse range of tissues [41]. Biological SHG imaging was first reported in 1986 when Freund investigated the polarity of collagen fibers in rat-tail tendons at a resolution of ~50 μm [42]. In 2002, Mohler and Campagnola reported practical implementation of tissue imaging at high resolution and rapid data acquisition using laser scanning. Since then, SHG microscopy has been an increasingly used imaging tool [43]. Schmeltz et al. employed SHG to sense fibrillar collagen

architecture in connective tissues [44]. They successfully depicted an image in human cornea sections and confirmed that this technique efficiently reveals collagen fibrils oriented out of the focal plane. Kato demonstrated an SHG microscope could be used as a real-time bioimaging observation on how toxins induce damage to the cell membranes or how the cells reconstruct the damaged membranes [45].

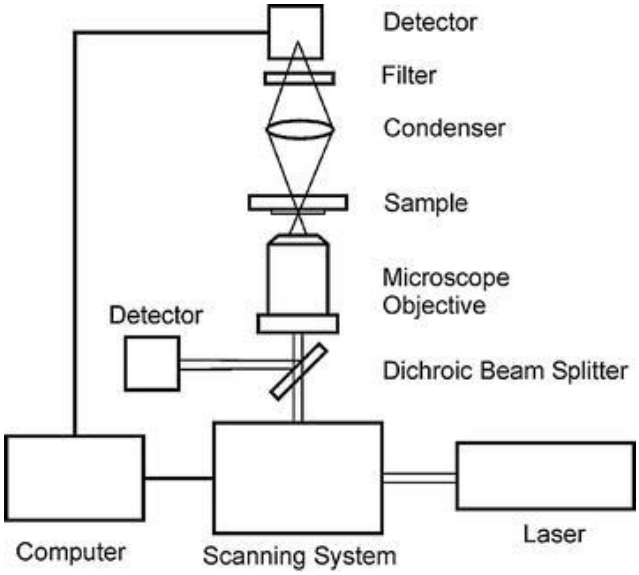

Figure 1.9. General optical scheme of a second harmonic microscope setup [41].

1.2 Motivation and objectives

Many kinds of methods with high-precision angle measurement have been presented and commercially produced; however, the research in optimizing the angle sensor is still a challenging and sustained research core to meet the need for the current trend of technology that leads to the manufacturing of high complexity products, yet shrinking in dimensions. It requires a suitable angle sensor that is not limited by the type of material being measured, has minimal potential damage to the material during the measurement process, and is expected to have minimal maintenance costs. However, several issues have been found in using conventional angle sensors. An inductive angle positioning sensor, for example, has limitations for detecting the metal target only. Meanwhile, the autocollimator is time-consuming as it is hardly positioned and requires regular maintenance. The rotational magnetic encoder

commonly contains fine parts that are sensitive to contamination. These reasons encourage more intensive research on new angle measurement methods, especially non-contact angle sensors, as the solution to bridge these problems.

Based on the explanation above, this study aims to propose a novel angle measurement based on second harmonic generation with high precision and resolution that can detect very small angular displacement. As mentioned in the previous section, the SHG is commonly implemented in imaging technology. Even though the generating second harmonic wave (SHW) is closely related to the angle due to the phase-matching angle characteristic to achieve high efficiency of SHG, the implementation of SHG as the angle sensor has not been reported. The SHG-based-angle sensor offers a contactless angle sensor that works with Fs laser as the laser source. Unlike a monochromatic laser, an Fs laser provides a wide range of wavelengths with high output power. The Fs laser characteristic and the nonlinear characteristic in material (NLO crystal is used in this study) can realize the high precision angle measurement.

In order to achieve the aim of the research, this study focuses on the following specific objectives:

1 To design a high precision angle measurement method by implementing the SHG phenomenon and Fs laser.
2 To confirm the feasibility of the proposed angle sensor theoretically and experimentally.
3 To evaluate the performance of the proposed angle sensor.

1.3 Outlines of this dissertation

The overall structure of the thesis takes the form of six chapters, including this introductory chapter.

Chapter 2 presents the theoretical concepts related to SHG and their implementation in angle sensors. Important aspects of SHG-based angle sensors such as phase-matching conditions, NLO crystal characteristics, and light source characteristics will

also be discussed.

Chapter 3 presents a proposed design of an intensity-dependent SHG-based angle sensor with a focused beam of Fs used as the laser source. The theoretical calculations of the focused beam scheme are presented, and experiments to clarify the feasibility of the proposed angle sensor will be discussed. The ray-tracing method is also presented to track and confirm the chromatic aberration.

Chapter 4 presents the proposed SHG-based angle sensor with wavelength-dependent. Different configurations will be introduced to solve the chromatic aberration problem in the previous method. Theoretical calculations will be discussed to estimate the measurement trend of the proposed method. The feasibility of the proposed angle sensor is confirmed experimentally, where the results will be discussed further.

Chapter 5 presents the optimization of the wavelength-dependent SHG angle sensor to extend the working distance and overcome the problem of misalignment in the direction of laser propagation using a collimated Fs laser. Experiments were carried out at several crystal positions along the Z-axis. Theoretical calculations and experimental results regarding the performance and feasibility of the method will be discussed further.

Chapter 6 presents the summary and the conclusion of every chapter in this study.

1.4 References

1. Shimizu, Y.; Matsukuma, H.; Gao, W. Optical angle sensor technology based on the optical frequency comb laser. *Appl. Sci.* **2020**, *10*, 4047.
2. Mou, J.; Su, J.; Miao, L.; Huang, T. Misalignment angle measurement and angle measurement deviation compensation of fiber optic gyroscope based on tilt sensor. *Optical Fiber Technology* **2021**, *63*, 102509.
3. Dornfeld, D.; Lee, D.E. *Precision Manufacturing* 2008. Springer: New York, USA, pp. 73–84.
4. Javaid, M.; Haleem, A.; Singh, R.P.; Rab, S.; Suman, R. Significance of sensors for industry 4.0: Roles, capabilities, and applications. Sens. Int. 2021, 2, 100110.
5. Kalsoom, T.; Ramzan, N.; Ahmed, S.; Ur-Rehman, M. Advances in sensors

technologies in the era of smart factory and industry 4.0. Sensors 2020, 20, 6783.

6. Hsieh, H.L.; Lee, J.Y.; Chen, L.Y.; Yang, Y. Development of an angular displacement measurement technique through birefringence heterodyne interferometry. Optic Express 2016, 24(7), 257292.
7. Smith, S.T.; Seugling, R.M. Sensor and actuator considerations for precision, small machines. Precis. Eng. 2006, 30, 245–264
8. Zhang, Z.; Yan, J.; Kuriyagawa, T. Manufacturing technologies toward extreme precision. Int. J. Extrem. Manuf. 2019, 1, 022001.
9. Fulmek, P.L.; Wandling, F.; Zdiarsky, W.; Brasseur, G. Capacitive sensor for relative angle measurement. *IEEE Transactions on Instrumentation and Measurement* **2002**, *51(6)*, 1145–1149.
10. Sauter, T. A smart capacitive angle sensor. *IEEE Transactions on Instrumentation and Measurement* **2005**, *1(4)*, 250–258.
11. Fu, Y.; Fan, W.; Jin, H.; Chen, Q. A new capacitance angle sensor of concentric ring multi-layer differential. *Measurement* **2020**, *158*, 107625.
12. Brajon, B.; Lugani, L.; Close, G. Hybrid magnetic-inductive angular sensor with 360º range and stray-field immunity. *Sensors* **2022**, *22(6)*, 2153.
13. Luo, P.; Tang, Q. Design anddevelopment of a self-calibration-based inductive absolute angular position sensor. *IEEE Sensors Journal* **2019**, *19(14)*, 5446–5453.
14. Wu, Z.; Bian, L.; Wang, S.; Zhang, X. An angle sensor based on magnetoelectric effect. *Sensors and Actuators A* **2017**, *265*, 108–113.
15. Zhang, Z.; Ni, F.; Dong, Y.; Guo, C.; Jin, M.; Liu, H. A novel absolute magnetic rotary sensor. *IEEE Transactions on Industrial Electronics* **2015,** *65(7)*, 4408–4419.
16. Twu, R.C.; Yan, N.Y. Immersion-type KTP sensor for angular displacement measurement. *Optics and Laser Technology* **2019**, *120*, 105690.
17. Rana, M.; Mrazib, M.; Saleh, T.; Muthalif, A.G.A. Development of an angle sensor using optical polarizer. *ARPN* **2015**, *20(23)*, 17416–17420.
18. Lin, W.Y.; Huang, C.W. Absolute rotary encoder system based on optical sensor for angular measurement. *The Journal of Supercomputing* **2021**, *77*, 8355–8373.
19. Kumar, A.S.A.; George, B. Technology and applications of angle sensors: A review. *IEEE Sensors Journal* **2021**, *21(6)*, 7195–7206.
20. Sauter, T.; Kero, N. System analysis of a fully-integrated capacitive angular sensor. *IEEE Trans. Instrum. Meas* **2002**, *51(6)*, 1328–1333.

21. Li, X.; Meijer, G. C. M.; de Jong, G. W.; Spronck, J. W. An accurate low-cost capacitive absolute angular-position sensor with a full-circle range. *IEEE Trans. Instrum. Meas*. *45(2)*, 516–520.

22. Yu, Z.; Peng, K.; Liu, X.; Chen, Z.; Huang, Y. A high-precision absolute angular-displacement capacitive sensor using three-stage time grating in conjunction with a remodulation scheme. *IEEE Trans. Ind. Electron.* **2019**, *66*(*9*), 7376–7385.

23. Kumar, A.S.A.; Anandan, N.; George, B.; Mukhopadhyay, S. C. Improved capacitive sensor for combined angular and linear displacement sensing. *IEEE Sensors J*. **2019,** *19*(22), 10253–10261.

24. Xiao, L,; Li, Z.; Bi, C. An optimization approach to variable reluctance resolver. *IEEE Trans. Magn*. **2020**, *56*(*2*).

25. Zhang, Z.; Ni, F.; Dong, Y.; Guo, C.; Jin, M.; Liu, H. A novel absolute magnetic rotary sensor. *IEEE Trans. Ind. Electron*. **2015**, *62(7)*, 4408–4419.

26. Li, S.; He, Q.; Zhang, Z.: Han, B.; Li, Z.; Lan, J. Simple eddy current sensor for small angle measurement. *Proc. Precis. Electromagn. Meas.* **2012**, 496–497.

27. Reddy, B. P.; Murali, A.; Shaga, G. Low-cost planar coil structure for inductive sensors to measure absolute angular position. *Proc. 2nd Int. Conf. Frontiers Sensors Technol. (ICFST)*, Shenzhen, China, Apr. 2017, 14–18

28. Wu, S.-T.; Chen, J.-Y.; Wu, S.-H. A rotary encoder with an eccentrically mounted ring magnet. *IEEE Trans. Instrum. Meas*. **2014**, *63*(8), 1907–1915.

29. Wang, S.; Wu, Z.; Peng, D.; Chen, S.; Zhang, Z.; Liu, S. Sensing mechanism of a rotary magnetic encoder based on time grating. *IEEE Sensors J*. **2018**, *18(9)*, 3677–3683.

30. Ren, W.; Cui, J.; Tan, J. A three-dimensional small angle measurement system based on autocollimation method. *Sci. Instrum.* **2022**, *93*, 055102.

31. Yin, Y.; Cai, S.; Qiao, Y. Design, fabrication, and verification of a three-dientional autocollimator. *Applied Optics* **2016**, *55(35)*, 9986–9991.

32. Li, R.; Zhen, Y.; Di, K.; Wang, W.; Nikitin, M.; Tong, M.H.; Zhang, Y.; Zou, X.; Konyakhin, I. Three-degree-of-freedom autocollimator with large angle-measurement range. *Meas. Sci. Technol.* **2021**, *32*, 115005.

33. Franken, P.A.; Hill, A.E.; Peters, C.W.; Weinreich, G. Generation of Optical Harmonics, Phys. Rev. Lett. **1961**, *7*, 118–119.

34. Dantzig, N.A. Planken, P.C.M; Bakker, H.B. Far-infrared second-harmonic generation and pulse characterization with the organic salt DAST. *Opt. Lett.* **1998**,

23, 466–468.

35. Panda, R.; Das, S.K. Fringe resolved autocorrelator for characterization of ultrashort laser pulses using second harmonics of ZnO nanorods, Optics Communications **2017**, *402*, 398–400.
36. Li, Y.; Chen, Y.; Li, W.; Wang, P.; Shao, B.; Peng, Y.; Leng, Y. Accurate characterization of mid-infrared ultrashort pulse based on second-harmonic-generation frequency-resolved optical grating. *Opt. Laser Technol*. **2019**, *120*, 105671.
37. Ionica, I. Second harmonic generation: A non-destructive characterization method for dielectric-semiconductor interfaces. International Semiconductor Conference (CAS) **2018**, 35–42.
38. Lüpke, G. Characterization of semiconductor interfaces by second-harmonic generation. *Surface Science Reports* **1999**, *35*, 75–161.
39. Vanbel, M.K.; Delabie, A.; Sioncke, S.; Adelmann, C.; Afanas'ev, V.V.; Locquet, J.P.; Elshocht, S.V.; Caymax, M.; Verbiest, T. Second-harmonic generation as characterization tool for Ge/high-k dielectric interfaces. *Proc. SPIE* **2012,** 8434.
40. Nakamura, K.; Kurokawa, A.; Ichimura, S. In-situ surface and interface characterization by optical second harmonic generation (SHG) of silicon dioxide fabrication with high purity ozone. *AIP Conference Proceedings* **1998**, *449*, 326–330.
41. Bianchini, P.; Diaspro, A. *Second Harmonic Generation Microscopy (SHG)*. In: Roberts G.C.K. (eds) Encyclopedia of Biophysics. Springer: Berlin, Heidelberg, 2013.
42. Freund, I.; Deutsch, M.; Sprecher, A. Optical second harmonic microscopy, crossed-beam summation, and small-angle scattering in Rat-tail tendon. *Biophys. J*. **1986**, *50*, 693
43. Campagnola, P. J.; Millard, A. C.; Terasaki, M.; Hoppe, P. E.; Malone, C. J.; Mohler, W. A. Three-dimensional high-resolution second-harmonic generation imaging of endogenous structural proteins in biological tissues, *Biophys. J*. **2002**, *82*, 493.
44. Schmeltz, M.; Teulon, C.; Latour, G.; Ghoubay, D.; Borderie, V.; Aimé, C.; Klein, M.C.S. Implementation of artifact-free circular dichroism SHG imaging of collagen. *Opt. Express* **2019**, *27*, 22685–22699
45. Kato, N. Optical second harmonic generation microscopy: application to the sensitive detection of cell membrane damage. *Biophys Rev* **2019**, *11*, 399–408.

Chapter 2
Proposal of the second harmonic generation angle sensor and theoretical analysis

2.1 Introduction

This chapter will explain the proposal of an angle sensor utilizing the second harmonic generation (SHG) phenomenon in the nonlinear optical (NLO) crystal as the fundamental principle in detecting angular displacement. As briefly mentioned in the previous chapter, SHG is a nonlinear optical phenomenon in which the fundamental wave (FW) at a specific frequency passes through the NLO crystal. The second harmonic wave (SHW) at frequency-doubled is generated. However, the generation of SHG in the NLO crystal can only occur in a specific condition. In particular, the selection of the laser source, the characteristics of the NLO crystal, and the angular position of the NLO crystal play an essential role in generating the SHG, which is then applied to the proposed angle sensor. By considering the appropriate parameter, the measurement trend of the proposed angle sensor can be estimated. The detailed principle and parameter of the SHG angle sensor and the theoretical analysis will be described further.

2.2 Basic equations of second harmonic generation

The process of SHG involves the interaction of two waves at frequency ω to produce a wave with the frequency 2ω inside nonlinear optic material, such as nonlinear optical (NLO) crystal. Material properties can generally be classified based on crystallography as isotropic and anisotropic material. Isotropic refers to material that is direction-independent or has the same properties in all directions; meanwhile, anisotropic is direction-dependent material that shows different properties in different directions. Anisotropic crystals can be further classified into uniaxial and biaxial crystals based on the number of the optic axis where the uniaxial crystals have one optic axis, and biaxial crystals have two optic axes. The optic axis of the crystal is a direction in which a ray of transmitted light suffers no birefringence. Birefringence is an optical property of the crystal with a refractive index that depends on the polarization and direction of light propagation.

In this study, the proposed angle sensor works based on SHG generated by traveling the light source into uniaxial crystals. The basic equation of SHG and the characteristic of the uniaxial crystal will be explained further in this section.

The analysis of SHG follows from the differential equations that describe the interaction between the fundamental and harmonic fields, and it is appropriate to describe the development of these coupled equations. Let's start with the general wave equation obtained from Maxwell's equation below [1-4]

$$\nabla_2 \mathbf{E}(\mathbf{r}.t) - \mu_0 \sigma \frac{\partial \mathbf{E}(r,t)}{\partial t^2} - \mu_0 \varepsilon_0 \frac{\partial^2 \mathbf{E}(\mathbf{r},t)}{\partial t 2} = \mu_0 \frac{\partial^2 \mathbf{P}(\mathbf{r},t)}{\partial t^2}, \tag{2.1}$$

where **P** is the polarization, **E** is the magnetic field vector, μ_0 is the permeability of the free space, σ is conductivity, **r** is vector position, t is time, ε_0 is vacuum permittivity in which the relation of $(\varepsilon_0\mu_0)^{-1/2}$ is equal to the speed of light in vacuum c. The electric field of the planewave at angular frequency ω is expressed in complex notation as the product of slowly varying complex amplitude and carrier wave with the formulation is shown in the following equation.

$$\mathbf{E}_{\omega}\left(\mathbf{r}.t\right)=\frac{1}{2}\left\{\mathbf{E}_{\omega}\exp\mathrm{i}\left(\mathbf{k}_{\omega}\cdot\ \mathbf{r}-\omega t\right)+\mathrm{c.c.}\right\}, \tag{2.2}$$

The intensity of the planewave is formulated as follows

$$I_{\omega}=\left(\frac{nc\varepsilon_{0}}{2}\right)\left|E_{\omega}\right|^{2}, \tag{2.3}$$

Here n is the refractive index of the material in which E is satisfied. The nonlinear polarization resulting from the second-order susceptibility driven by the plane wave $\mathbf{E}_{\omega}(\mathbf{r},t)$ is expressed as

$$\mathbf{P}_{2\omega,i}^{\mathrm{NL}}\left(\mathbf{r},t\right)=\frac{1}{2}\left\{\mathbf{P}_{2\omega}^{\mathrm{NL}}\exp\mathrm{i}\left(\mathbf{2k}_{\omega}\cdot\ \mathbf{r}-2\omega t\right)+\mathrm{c.c.}\right\}, \tag{2.4}$$

The individual components of the polarization amplitude vector are formulated below

$$P_{2\omega,i}^{\mathrm{NL}}=\varepsilon_{0}\sum_{j,k}d_{ijk}\left(-2\omega;\omega;\omega\right)E_{\omega,j}E_{\omega,k}\ , \tag{2.5}$$

A number of simplifications are used to arrive at the coupled equations for harmonic generation with monochromatic plane waves. All waves are assumed to be propagating collinearly in the z direction. Only the vector components involved in the interaction are retained, and the nonlinear optical tensor is replaced by the scalar effective nonlinear coefficient d_{eff}. Finally, the slowly varying envelope approximation is invoked and the higher-order derivatives of the amplitudes are ignored, as are time derivatives of the envelopes. The wave equation can be simplified as follows

$$\frac{\mathrm{d}E\left(z\right)}{\mathrm{d}z}+\alpha E\left(z\right)=\mathrm{i}\frac{\mu_{0}c\omega}{2n}P\left(z\right), \tag{2.6}$$

The optical absorption coefficient α later be used to express $\mu_{0}\sigma c/2$.

In the case of type-I SHG, the fundamental field consist of only a single eigen polarization, and there are two coupled equations as follows.

$$\frac{\mathrm{d}E_{2\omega}(z)}{\mathrm{d}z}+\alpha_{2\omega}E_{2\omega}(z)=\mathrm{i}\frac{\omega d_{eff}}{n_{2\omega}c}E_{\omega}(z)E_{\omega}(z)\exp(-\mathrm{i}\Delta kz), \tag{2.7}$$

$$\frac{\mathrm{d}E_{\omega}(z)}{\mathrm{d}z}+\alpha_{\omega}E_{2\omega}(z)=\mathrm{i}\frac{\omega d_{eff}}{n_{\omega}c}E_{\omega}(z)E_{\omega}^{*}(z)\exp(\mathrm{i}\Delta kz), \tag{2.8}$$

Here $n_{2\omega}$ and n_{ω} denote the refractive index at the harmonic and the refractive index at the fundamental, respectively; $\alpha_{2\omega}$ and α_{ω} are respective absorption coefficients. The wave vector mismatch Δk is formulated as follows

$$\Delta k=k_{2\omega}-2k_{\omega}, \tag{2.9}$$

where k is corresponding to the wave frequency ω in the crystal with the following relation

$$k_{\omega,2\omega}=\frac{2\pi n_{\omega,2\omega}}{\lambda_{\omega,2\omega}}, \tag{2.10}$$

The solution of the coupled Equation (2.7) and (2.8) can be expressed by treating $E_{\omega}(z)$ as constant with no significant absorption. The initial condition is set as $I_{\omega}(0)$ when the light incident on the crystals and SHG intensity in crystal surface $I_{2\omega}(0)$ is equal to 0. Then the following equation is the expression for electric field after propagation for a distance L in the crystal.

$$E_{2\omega}(L)=\frac{\omega d_{\mathrm{eff}}E_{\omega}^{2}(0)}{n_{2\omega}c}\frac{1}{\Delta k}\left\{\exp\mathrm{i}(k_{2\omega}L)-\exp\mathrm{i}(2k_{\omega}L)\right\}, \tag{2.11}$$

If the solution is expressed as the intensity, it can be formulated as shown in Equation (2.12) below.

$$I_{2\omega}(L)=\frac{2\omega^{2}d_{\mathrm{eff}}^{2}L^{2}}{n_{2\omega}n_{\omega}^{2}c^{3}\varepsilon_{0}}I_{\omega}^{2}(0)\frac{\sin^{2}(\Delta kL/2)}{(\Delta kL/2)^{2}}, \tag{2.12}$$

The expression of SHG intensity at Equation (2,12) in the term of wavelength is given by the following equation

$$I_{2\omega}(L) = \frac{8\pi^2 d_{\text{eff}}^2 L^2}{n_{2\omega} n_\omega^2 c\varepsilon_0 \lambda_\omega^2} I_\omega^2(0) \frac{\sin^2(\Delta kL/2)}{(\Delta kL/2)^2}, \tag{2.13}$$

In the term of power, the SHG power can be determined by the following equation

$$p_{2\omega}(L) = \frac{2\pi^2 d_{\text{eff}}^2 L^2}{n_{2\omega} n_\omega^2 c\varepsilon_0 \lambda_\omega^2} \frac{p_\omega^2(0)}{A} \frac{\sin^2(\Delta kL/2)}{(\Delta kL/2)^2}, \tag{2.14}$$

where A is the cross-sectional area of the laser beam, p_ω and $p_{2\omega}$ denote the fundamental power and SHG power, respectively. From ration of the SHG power and fundamental power, the efficiency of the SHG η(L) can be determined as follows

$$\eta(L) = \frac{p_{2\omega}(L)}{p_\omega(0)}, \tag{2.15}$$

As mentioned before, the uniaxial crystal has a special direction called the optic axis. If there is a light passing through the crystal, the light containing the optical axis (c-axis) and the wavevector k of the light is in a plane termed as the principal plane as shown in Figure 2.1. In the condition when the light is polarized normal to the principal plane it is called an ordinary ray (o-ray) in which the refractive index does not depend on the propagation direction. Meanwhile, if the light is polarized in the principal plane, it is called an extraordinary ray (e-ray) whereas it depends on the propagation direction. The o-ray always suffers the refractive index n_o that depends on wavelength λ, meanwhile e-ray will always experience the refractive index n_e that depends on λ and angle θ. This kind of condition in which an incident ray of light splits into two rays is called the birefringence phenomenon. With adequate birefringence, it may be possible to obtain phase matching $\Delta k = 0$ by selecting the direction of propagation in the NLO crystal.

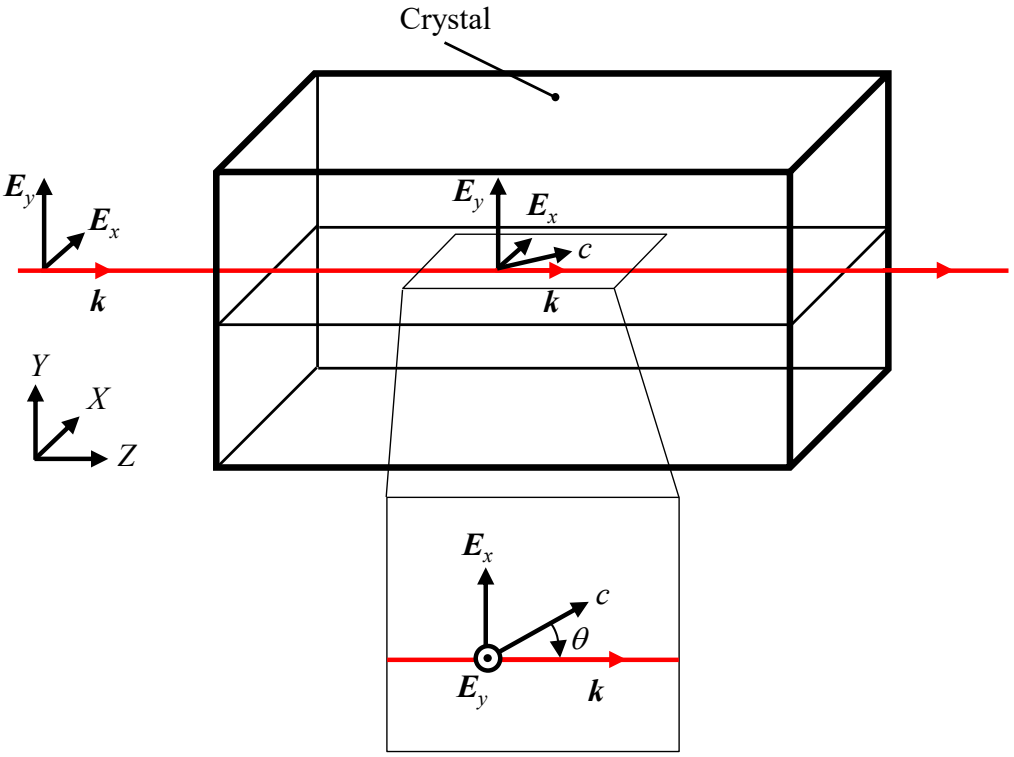

Figure 2.1 Illustration of the light propagation in the crystal.

In the use of uniaxial crystal with type-I phase matching, Figure 2.2a shows the refractive index in two-dimensional projection. The phase-matching condition is shown in Figures 2.2b and 2.2d, in which the constructive interference of SHW is satisfied. On the other hand, Figure 2.2c and 2.2e shows the case of phase mismatching condition where the interference of SHW is destructive to each other. As shown in figure 2.2b, to have phase matching, it is necessary to choose a direction of propagation that makes an angle θ with the optic axis that satisfies the Equation (2.16).

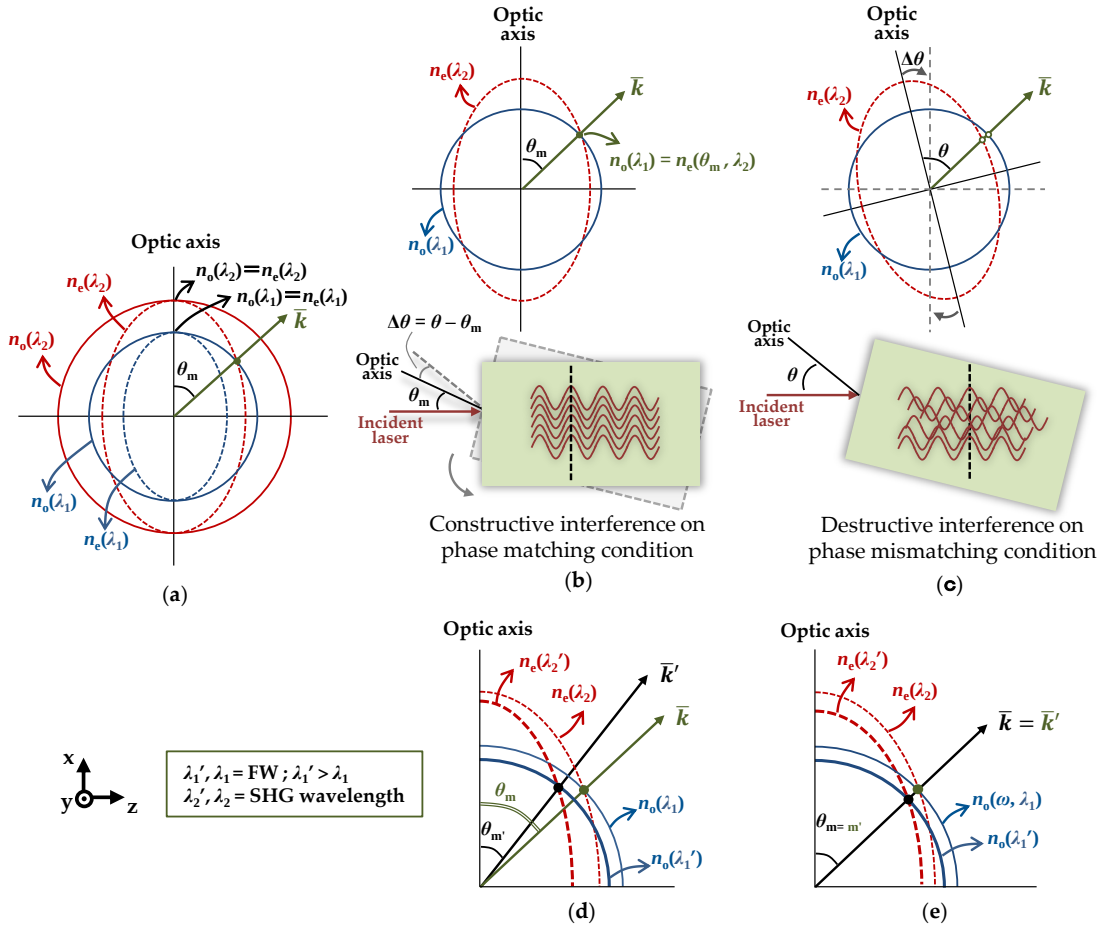

Figure 2.2 (**a**) Two-dimensional perspective of the refractive indices surface for type-I negative uniaxial crystal; (**b**) phase mismatching condition; (**c**) phase matching condition; (**d**) the change on refractive indices surface followed by the change of phase matching angle; (**e**) the change of refractive indices surface with the same phase matching angle at a certain range of wavelengths. [5]

$$n_e\left(\theta, \lambda_{2\omega}\right) = n_o\left(\lambda_\omega\right), \tag{2.16}$$

where $n_o(\lambda_\omega)$ denotes the ordinary index for fundamental wave (FW) propagation λ_ω, meanwhile $n_e(\theta,\lambda_{2\omega})$ denotes the extraordinary index for SHG wavelength propagation $\lambda_{2\omega}$ at an angle of θ to the optical axis that given by [6, 7]

$$\frac{1}{n_e^2\left(\theta, \lambda_{2\omega}\right)} = \frac{\cos^2\theta}{n_o^2\left(\lambda_{2\omega}\right)} + \frac{\sin^2\theta}{n_e^2\left(\lambda_{2\omega}\right)}, \tag{2.17}$$

$$n_e\left(\theta, \lambda_{2\omega}\right) = \left\{ \left[\frac{\cos\theta}{n_o\left(\lambda_{2\omega}\right)} \right]^2 + \left[\frac{\sin\theta}{n_e\left(\lambda_{2\omega}\right)} \right]^2 \right\}^{-1/2}, \tag{2.18}$$

The phase-matching angle is obtained by the identity $\cos^2\theta = 1 - \sin^2\theta$ and phase-matching angle can be formulated as

$$\theta_{\mathrm{m}} = \sin^{-1}\left(\sqrt{\frac{n_{\mathrm{o}}^{-2}\left(\lambda_{\omega}\right) - n_{\mathrm{o}}^{-2}\left(\lambda_{2\omega}\right)}{n_{\mathrm{e}}^{-2}\left(\lambda_{2\omega}\right) - n_{\mathrm{o}}^{-2}\left(\lambda_{2\omega}\right)}} \right), \tag{2.19}$$

From Figure 2-2, it is known that $n_{\mathrm{e}}(\lambda_{2\omega})$ is equal to extraordinary index for propagation at 90º to the optic axis $n_{\mathrm{e}}(90º,\lambda_{\omega})$. Later let it mentioned as $N_{\mathrm{e}}(\lambda_{2\omega})$.

As previously mentioned, the nonlinear optical tensor in the solution of the coupled-wave equations is replaced by scalar effective nonlinear d_{eff}. This parameter depends on the polarization of the field, type of phase matching, propagation direction, the crystallographic point group of the crystal, and the presence of absorption. For the crystal of point group *3m* with negative birefringence, such as beta barium borate (BBO) and lithium niobate ($LiNbO_3$), the effective nonlinear coefficient for type-I phase matching is given by

$$d_{\mathrm{eff}} = d_{22}\cos^2\theta\cos 3\phi, \tag{2.20}$$

where d_{22} are tensors components that have respective value for NLO. From the equation, it is noticed that the propagation of the light is related to two crystallographic angles, θ and ϕ; θ is the angle between optical axis and the direction of vector *k* and this angle is strictly determined by the phase-matching condition, as it has discussed before. On the other hand, ϕ is the azimuthal angle that related to the crystal orientation and does not influence phase matching for the case of a uniaxial crystal [8].

By using the requirement in Equation (2.16), the Equation (2.9) to express the phase mismatching can be formulated in Equation (2.21) to predict the SHG power in Equation (2.14).

$$\Delta k = \frac{4\pi}{\lambda_{\omega}}\left[n_o\left(\lambda_{\omega}\right) - n_e\left(\theta, \lambda_{2\omega}\right)\right], \tag{2.21}$$

For generating the efficient SHG, there are features that must mainly be fulfilled. First, the fundamental wave intensity must be sufficiently high over a certain propagation length because for small conversion efficiencies at least SHG is proportional to I^2. This condition can be achieved by using a high-power laser source. Second, the nonlinear medium must have a high second-order nonlinear coefficient, therefore a careful choice of the NLO crystal is necessary. Lastly, the light beams involved need to preserve their phase relation over the propagation length. This condition requires additional measures since dispersion generally leads to a phase mismatching between the FW and SHW. The phase mismatching leads to destructive interference of second harmonic wave generated at the very beginning of the NLO crystal with that generated further inside the NLO. Thereby, it is limiting the maaximum output power. However, this problem can be overcome in the birefringence crystal by choosing a particular orientation [9].

2.3 Gaussian beam characteristic

In this study, a mode-locked femtosecond laser is used as the laser source to generate the second harmonic wave. The output of a mode-locked femtosecond laser is highly collimated where light propagates in a straight line on a homogeneous medium but the laser beam diverges during propagation due to diffraction effects. On the other hand, the beam from a laser typically has a Gaussian intensity profile in the transverse plane with respect to propagation wherein the laser beam will behave along the direction of propagation (z-axis) almost like a plane wave but instead of having a constant amplitude, as for a plane wave, the amplitude slowly varies over the direction of propagation along the z-axis [10].

As shown in the Figure 2.3, the beam is initially collimated and converges until they reach a minimum point inside the Gaussian beam envelope instead of a single point and then begins to slowly diverge. Let w_0 be the beam radius at its beam waist point and the coordinate position of the beam waist point is z = 0, then the maximum intensity I_0 occurs on-axis at z_0. The intensity I of the Gaussian beam can be expressed

in Equation (2.22) [11–13].

$$I(r,z) = I_0 \left(\frac{W_0}{W(z)} \right)^2 \mathrm{e}^{-\frac{2r^2}{w^2(z)}}. \tag{2.22}$$

The beam radius at distance z, from the waist is shown below

$$w(z) = w_0 \left[1 + \left(\frac{z}{z_0} \right)^2 \right]^{1/2}, \tag{2.23}$$

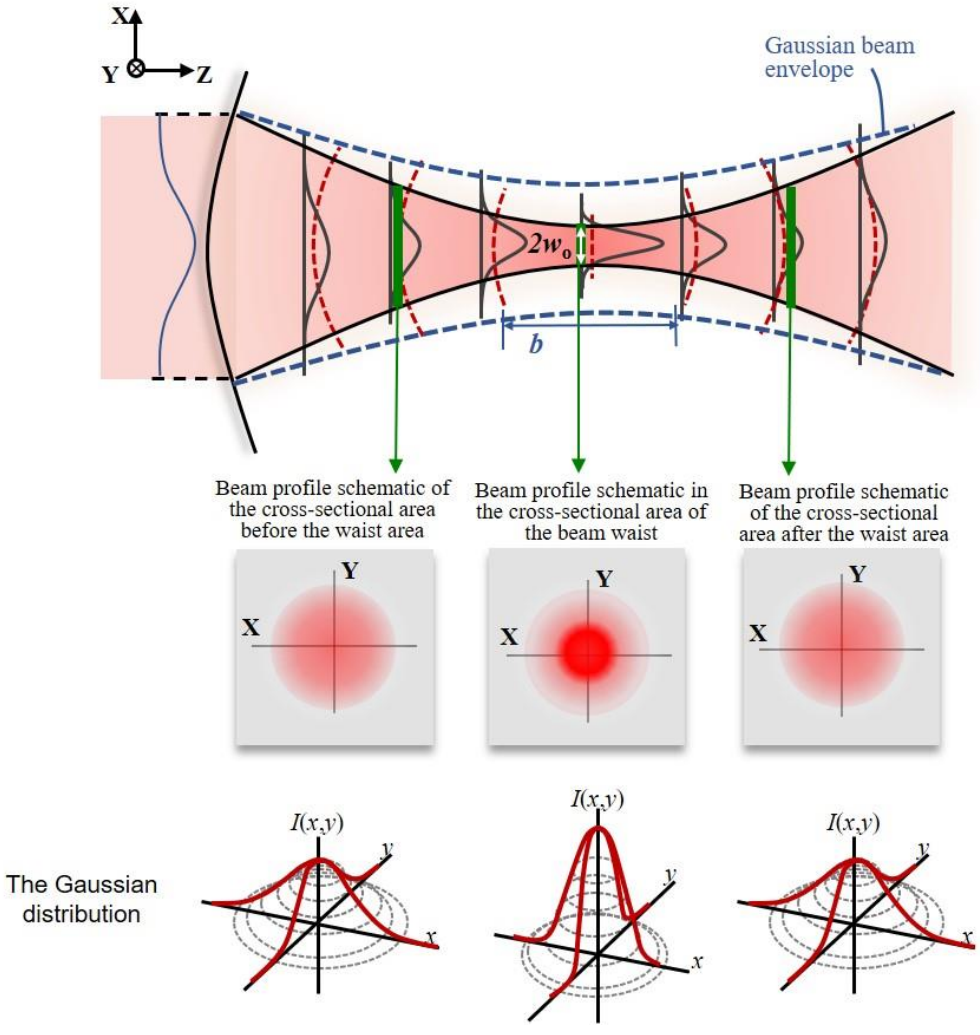

Figure 2.3 The illustration of focused Gaussian beam

Imagine that the laser beam is focused using converging lens or an off-axis parabolic mirror, to intensify the beam in the focal point area inside the nonlinear

optical crystal, the shape of the beam as it propagates along the *z*-axis can be illustrated in Figure 2.4. If focal distance of converging lens or off-axis parabolic mirror is f, the diameter of the incident collimated beam in the lens or parabolic mirror is d, and the wavelength of the incident beam is λ, then the focused beam diameter in term of input beam and focusing lens or parabolic mirror parameter is expressed as follows **[14]**

$$2w_0 = \frac{4f\lambda_0}{\pi d}, \tag{2.24}$$

The depth of focus (or confocal parameter), known as Rayleigh length is expressed as shown in Equation (2.25) in which n denotes the refractive index.

$$b = 2z_0 = \frac{2\pi w_0^2 n}{\lambda_0}. \tag{2.25}$$

By substituting Equation (2.24) to Equation (2.25), the Rayleigh length in the term of optical parameter is shown below.

$$b = \frac{8f^2\lambda_0 n}{\pi d^2}. \tag{2.26}$$

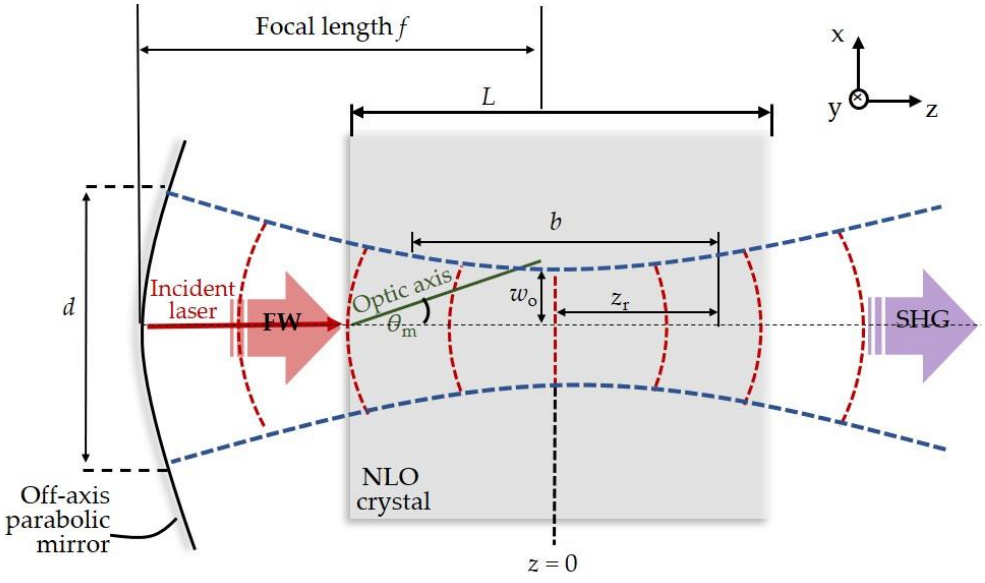

Figure 2.4 The focused laser beam in the nonlinear optical crystal

As shown in the Figure 2.4, the second harmonic wave is generated by focusing the Gaussian beam to the NLO crystal. When the focused beams are used, there are two opposite processes, first, the laser power density in the crystal increase due to focusing of the laser radiation into the NLO crystal as well as the vector phase matching should be taken into account. This condition leads to the increasing of SHG efficiency. Seconds, the influence of laser divergence and crystal birefringence also increase, hence the phase mismatch appear that leads to the decrease of SHG efficiency. In all practically important cases, the fixed-field approximation or the plane wave approximation can be used for the Gaussian beams. Hence, the following expression for the output of SHG power can be deduced

$$p_{2\omega}(L) = CkLp_{\omega}^{2}(0)h(\nu,\alpha,\xi,\mu). \tag{2.27}$$

where $h(\nu,\alpha,\xi,\mu)$ is the aperture function that given by

$$h(\nu,\alpha,\xi,\mu) = \frac{2\pi\sqrt{\pi}}{\xi}\int_{-\infty}^{\infty}\exp\left(-4s^{2}\right)\left|H(\nu',\alpha,\xi,\mu)\right|^{2}ds, \tag{2.28}$$

$$H(\nu',\alpha,\xi,\mu) = \frac{1}{2\pi}\int_{-\xi(1-\mu)}^{\xi(1-\mu)}\frac{\exp(\mathrm{i}\nu' T)}{1+\mathrm{i}T}dT. \tag{2.29}$$

where

$$\nu = \frac{kw_{0}^{2}\Delta k}{2} \tag{2.30}$$

$$\nu' = \nu + 4\alpha s, \tag{2.31}$$

$$\alpha = \frac{\rho k w_{0}}{2}, \tag{2.32}$$

$$\xi = \frac{L}{kw_{0}^{2}}, \tag{2.33}$$

$$T = \frac{2(z-f)}{b} \tag{2.34}$$

$$\mu = \frac{L-2z_0}{L} \tag{2.35}$$

$$C = \frac{2^7 \pi^4 d_{\text{eff}}^2}{n_{2\omega} n_\omega^2 c \lambda_\omega^2} \tag{2.36}$$

Here, ξ is the ratio of nonlinear crystal length L to the focal length or the parameter of focusing, μ is the relative position of focus inside the crystal, z_0 is the coordinate of the minimum beam radius, s is the variable of integration, and ρ is walk-off angle that can be determined by the following equation.

$$\rho = \arctan\left[\left(\frac{n_o}{n_e}\right)^2 \tan\theta\right] - \theta \tag{2.37}$$

There are two extreme cases when the angle matching θ_m equal to 90º, $\rho = 0$, $\alpha = 0$, and the focused beam is in the center of the crystal, $\mu = 0$, that can be obtained in the simple analytical expression. First, the condition of weak focusing, $\xi >> 1$, the aperture function has the following condition

$$h(\nu, 0, \xi, 0) = \xi \text{sinc}^2(\Delta kL/2). \tag{2.38}$$

Thus, the efficiency of SHG is given by

$$\eta(L) = \frac{p_{2\omega}(L)}{p_\omega(0)} = C p_\omega(0) L^2 \frac{\text{sinc}^2(\Delta kL/2)}{w_0^2} \tag{2.39}$$

The above SHG efficiency expression in this case is the same as for the SHG condition by the Gaussian beam phase mismatching in the plane wave fixed-field approximation. Another extreme case is the strong beam focusing in which $\xi << 1$, the aperture function for $\Delta k < 0$ is given by

$$h(\nu,0,\xi,0)=\xi^{-1}\left|\pi\exp(\nu)+\mathrm{Si}(-\Delta kL/2)-\pi/2\right|^2. \tag{2.40}$$

And for $\Delta k > 0$, the aperture function is given by

$$h(\nu,0,\xi,0)=\xi^{-1}\left|\mathrm{Si}(\Delta kL/2)-\pi/2\right|^2. \tag{2.41}$$

where Si(ΔkL/2) is the integration of sinc function.

2.4 Femtosecond laser source for angle sensor

In this section, fundamentals of the Fs laser, especially the mechanism of laser generation and other specification, is going to be introduced. The laser pulse has the order of femtosecond that generated by the excited active laser medium in the laser cavity, making the light of many frequency modes satisfying the Equation (2.42) and oscillates between reflectors in the cavity by stimulated emission [11].

$$\nu_i = \frac{ic}{2hn} \tag{2.42}$$

Here, h is the distance between the reflectors in the cavity, c is the speed of light in a vacuum, n is the refractive index of the medium in the laser cavity, i is an integer, and ν_i is the frequency mode corresponding to i. Through this mechanism, the continuous wave (CW) laser extracts the light. Meanwhile, an Fs laser is generated by matching the phase relation of many frequency modes oscillated in a CW laser as shown in Figure 2.5. The phase-matching relationship between the oscillation modes is called mode locking.

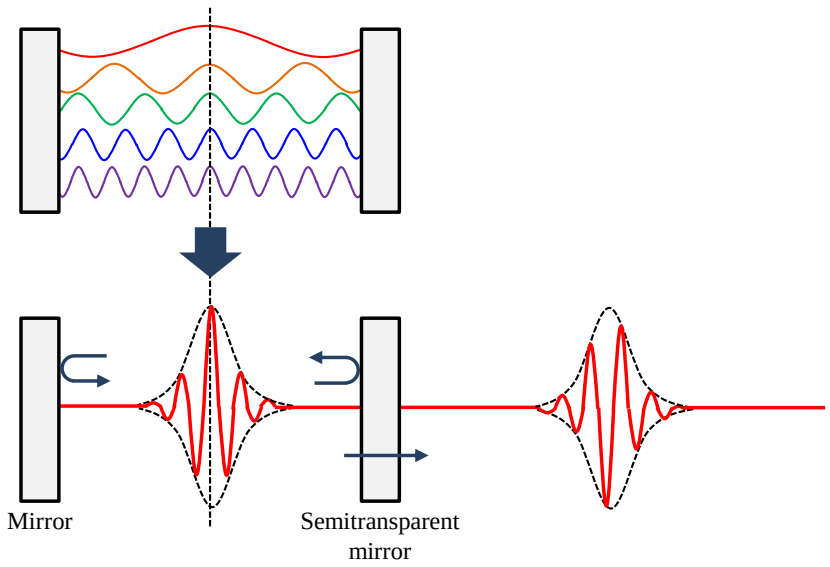

Figure 2.5 Conceptual diagram of mode locking femtosecond laser.

An Fs laser generated by mode-locking has electric field amplitude in the time domain as shown in Figure 2.6. The carrier is the actual electric field amplitude, and the pulse contour is called the envelope. The duration of the pulse is called the pulse width. The wider the frequency width of the laser, the smaller the pulse width, and generally the order of pulse is picosecond or femtosecond values.

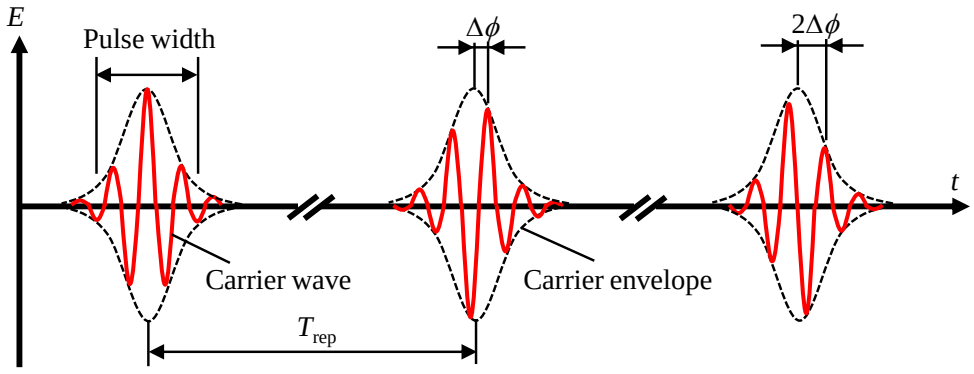

Figure 2.6 Schematic of femtosecond laser.

Mode locking can be roughly divided into active mode locking and passive mode locking [15]. Active mode locking is a method in which an amplitude modulator is placed in a resonator, correlation is forcibly formed in each longitudinal mode by the modulator, and a pulse is output. In this method, the optical frequency interval

(repetition frequency which is described later) is limited by the operating speed of the modulator, and the pulse width remains on the order of picoseconds. In addition, the polarization state changes due to environmental changes such as temperature and humidity, and it is difficult to obtain long-term output without stabilization control. On the other hand, the femtosecond pulse laser used in this study is generated by passive mode locking. Passive mode-locking is a method of generating a pulse by arranging an element whose transmittance changes depending on the light intensity in a resonator and allowing components with high peak intensity to survive naturally. In passive mode locking, a pulse width on the order of femtoseconds is feasible. The elements to be arranged include fiber type nonlinear elements, saturable absorbers, and their composites. Here, as an example, a method using a nonlinear optical element called a saturable absorber will be described [16, 17]. A saturable absorber is a substance that acts as an absorber for incident light with low intensity and acts as a transparent body for incident light with high intensity.

Figure 2.7 shows a schematic diagram of ultrashort pulse generation by a saturable absorber. Without a saturable absorber, light with multiple phases exists for each frequency mode in the resonator. If the saturable absorber is placed in the resonator, the light whose phase is shifted is absorbed by the saturable absorber because the light intensity of each frequency mode is low. It passes through the saturable absorber as a high intensity ultrashort pulse. As a result, only the light with the same phase of each mode remains in the resonator and is emitted to the outside as an ultrashort pulse through the translucent mirror. The mode-locking method of the light source used in this study is a method based on nonlinear polarization rotation using a fiber, and a passive mode-locking method applying the nonlinear phenomenon that polarization changes according to the intensity.

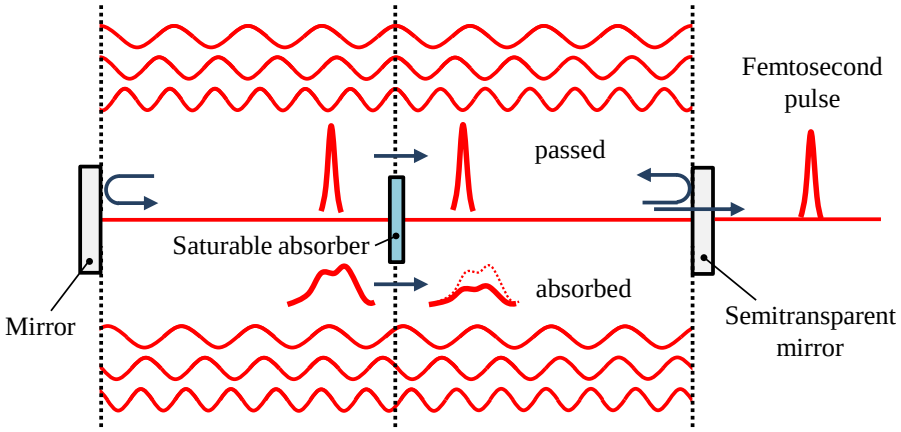

Figure 2.7 Mechanism of mode locking by a saturable absorber.

As mentioned above, the Fs pulse laser is composed of light groups of equal intervals. Hence, in the frequency order, a comb-like optical spectrum called an optical frequency comb is obtained. Figure 2.8 shows the femtosecond pulse laser in the frequency domain. Here, the comb of each frequency is called a mode, and the i-th mode frequency ν_i is represented by the following Equation [18].

$$\nu_i = i\nu_{\mathrm{rep}} + \nu_{\mathrm{CEO}} \tag{2.43}$$

Where ν_{rep} is called the repetition frequency and ν_{CEO}, the carrier envelope offset frequency. As shown in Figure 2.8, the repetition frequency represents the interval between each comb, and is equal to the reciprocal of the repetition period T_{rep} of the pulse train in the time domain. The offset frequency is the surplus frequency when the mode interval is extrapolated at a constant repetition frequency. This offset frequency is caused by the phase of the optical pulse, that is, the shift of the carrier with respect to the envelope. By stabilizing the repetition frequency and offset frequency, the absolute frequencies of all modes are stabilized, and an optical frequency comb with accurate frequencies can be obtained. The repetition frequency and offset frequency can be controlled and stabilized by synchronizing with an external frequency standard. By guaranteeing the low frequency repetition frequency and offset frequency (generally on the order of MHz) with an external standard having uncertainty of the order of 10^{-12}-10^{-15} the uncertainty of the frequency of each mode (generally on the

order of THz) is ensured. It enables to enlarge larger uncertainty of the frequency of each mode than that of the external standard. Generally, a rubidium standard or a cesium atomic clock is used as the external standard. In other words, by stabilizing the repetition frequency and offset frequency, the femtosecond laser becomes an optical frequency comb in the frequency spectrum band. This optical frequency comb is used in optical clocks [19] and so on because of its mode frequency accuracy.

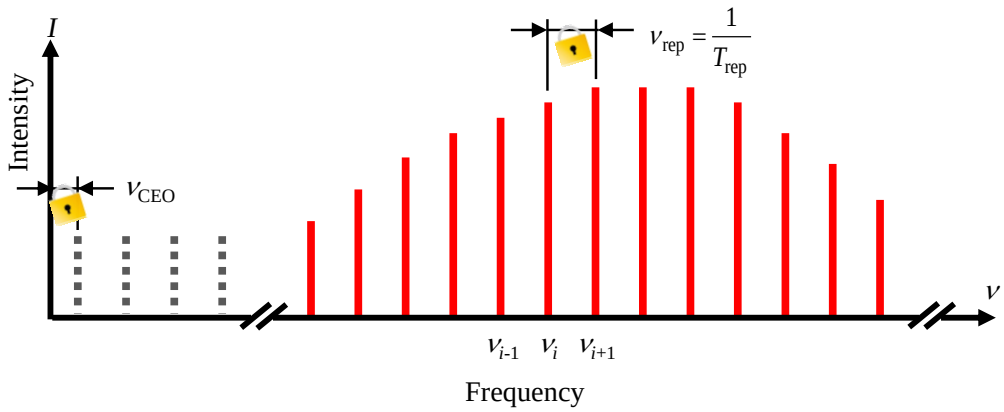

Figure 2.8 Schematic of the optical frequency comb.

However, most of conventional angle measurement methods utilize a single-frequency laser as a light source. There are some problems when a femtosecond laser with a broad frequency band is simply applied to the conventional principle. For example, in the case of the laser autocollimation method, it is necessary to form a small light spot on the detector using a condensing lens, but if femtosecond laser is used, the light spot is enlarged due to chromatic aberration, as shown in Figure 2.9, which causes decrease of sensitivity. In addition, in the critical angle method, as shown in Figure 2-6, there is an optical frequency where the amount of change in the reflectance with respect to the change in the incident angle is small, so the sensitivity may be reduced as a whole. In addition, in the method using interference fringes, interference fringes generated by a plurality of light beams of different frequency modes having different intervals are overlapped with each other as shown in Figure 2.11. In the same principle as the white light interferometer, the problem that interference fringes occur only when the optical path difference between the two beams is equal occurs. From the

above, it is necessary to develop a new angle measurement principle to which femtosecond lasers with characteristics different from monochromatic lasers can be applied.

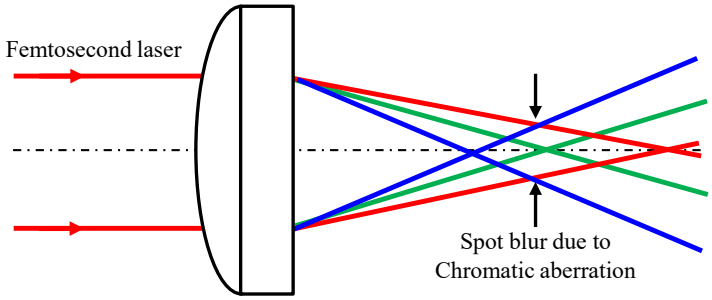

Figure 2.9 Schematic of chromatic aberration in the autocollimator.

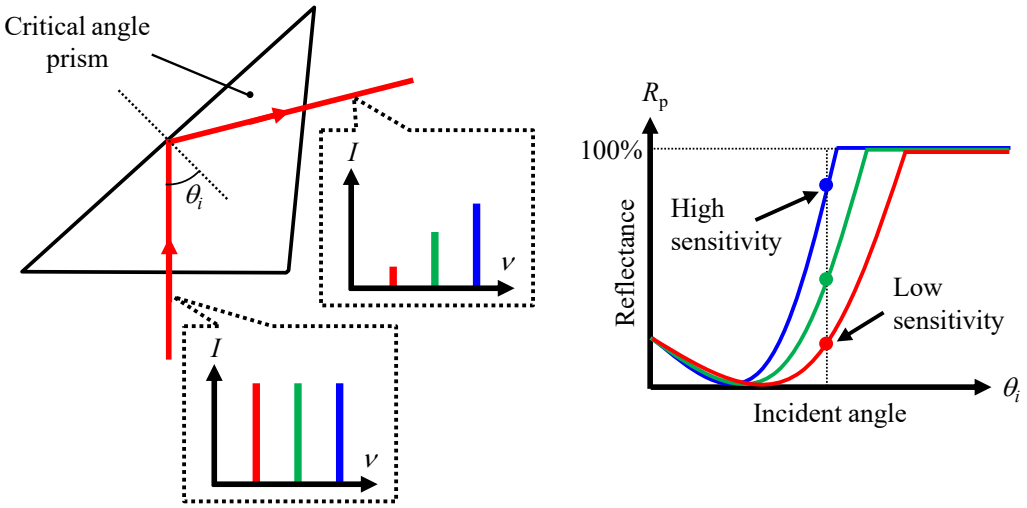

Figure 2.10 Sensitivity decrease by a difference of frequency.

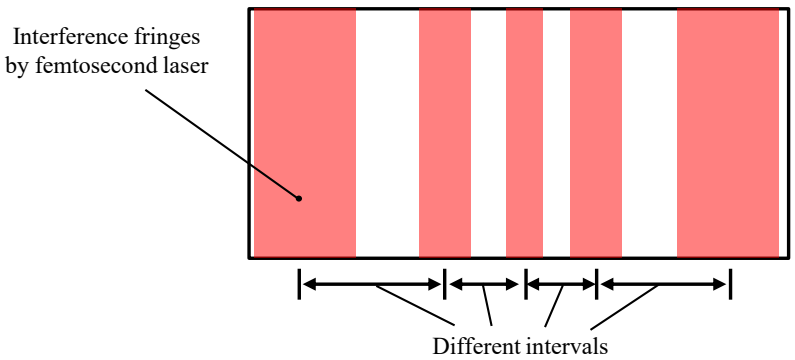

Figure 2.11 Interference fringes by a femtosecond laser.

2.5 Angle measurement principle based on SHG with femtosecond laser

The conventional angle measurement method that utilizes the laser in the configuration uses the laser with a radiation width of less than 0.1 nm. Such an emitted laser is included as the monochromatic laser due to its narrow radiation width. If the monochromatic laser irradiates toward the NLO crystal to generate the second harmonic wave, the phase-matching occurs at one specific angle and the dynamics of the SHG wave as the output can be done by varying the input power only. Femtosecond laser, as it is mentioned in the previous section, has a wide range of angle and high output power that makes it possible to be employed as laser source. Especially, since the output power of second harmonic wave correlates with an angle in between the wave vectors and the optical axis of the crystal, it is expected to be employed for angle measurement.

Figure 2.12 shows the illustration of the setup and the expected SHG spectrum in the use of monochromatic wavelength (see Figure 2.12a) and Fs wavelength that contains many wavelengths as it is emitted (see Figure 2.12.b). Let the monochromatic be used for the measurement system, the angular position of the NLO crystal can only detect by the change of SHG intensity, in which the highest intensity indicates the phase-matching angle of the given monochromatic wavelength. On the other hands, by using the wide range of angle, the angular position displacement of the crystal that represents the measurement target can be detected by the series of the spectrum. Each spectrum has a peak indicating that the angular position of the NLO crystal is the phase-matching angle of a specific wavelength within the wide range of wavelengths, and at the same time, the other wavelength will suffer phase-mismatching indicated by the lesser power of around the peak as can be seen in the spectra illustration in Figure 2.12b. If the NLO crystal rotates between the phase match angles of a given wavelength range, the spectrum will change and the SHG power peak shifted due to the change in the phase matching angle.

The implementation of the SHG-based angle measurement principle in the angle

sensor results in measurements that can be displayed in intensity dependent and wavelength dependent, regarding the configuration of the angle sensor. The feasibility of implementing SHG on angle sensors in both intensity-dependent and wavelength-dependent will be discussed in subsequent chapters.

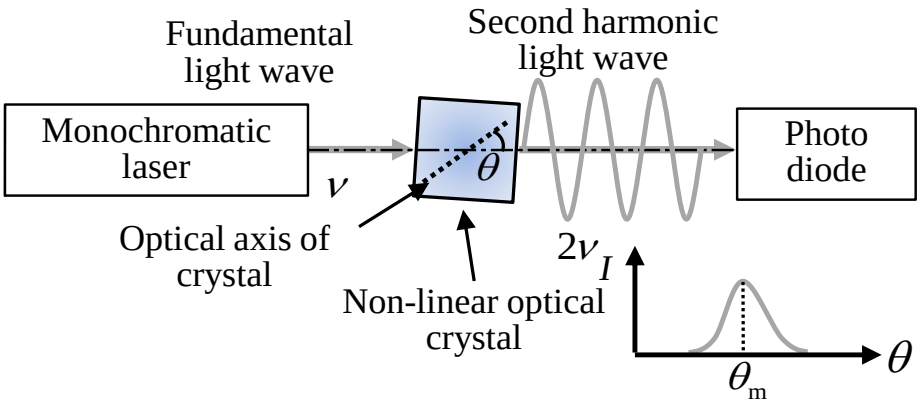

(a)

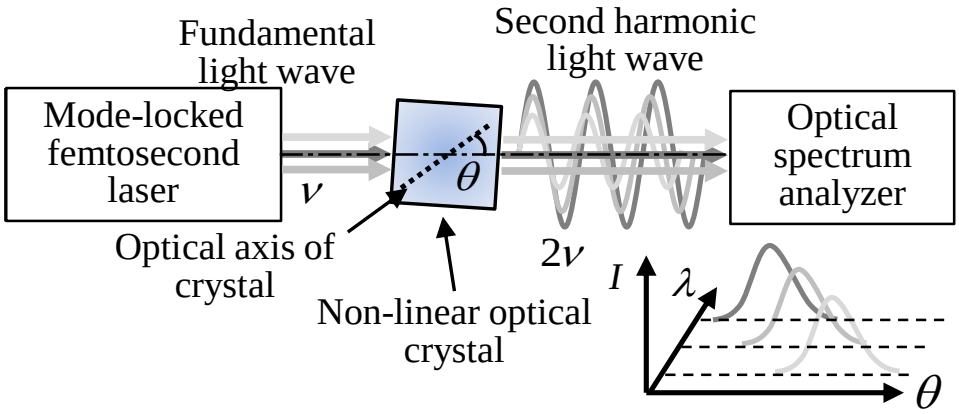

(b)

Figure 2.12 (a) Relationship between incident angle and intensity of second harmonic wave by monochromatic laser; (b) Relationship between incident angle and intensity of second harmonic wave by femtosecond laser.

2.6 Theoretical analysis

2.6.1 Beam radius characteristics at different focal lengths of the lens

As explained in the previous section, beam focusing serves to intensify the beam and obtain a higher power density to produce SHG. This is an effective method to

implement, especially in the use of an Fs laser with a relatively small output power as the laser source. To realize it, a parabolic lens or mirror can be used to focus the beam where the focal lengths of both optical devices need to be considered to obtain the appropriate beamwidth. To estimate the beamwidth of the focal beam, Equation (2.24) is used in which the focal length of the lens plays an important role in focusing the Fs laser beam.

Figure 2.13 shows the characteristic beam radius that half of the beamwidth at different focal lengths of the lens with parameters L, d, and λ set at 2 mm, 3.6 mm, and 1560 nm, respectively. The wavelength λ in this calculation is the central wavelength of the Fs wavelength range. As can be seen in the figure, the beam radius increases as a longer focal length are used. In other words, the strong focus can be realized with the use of a shorter focal length.

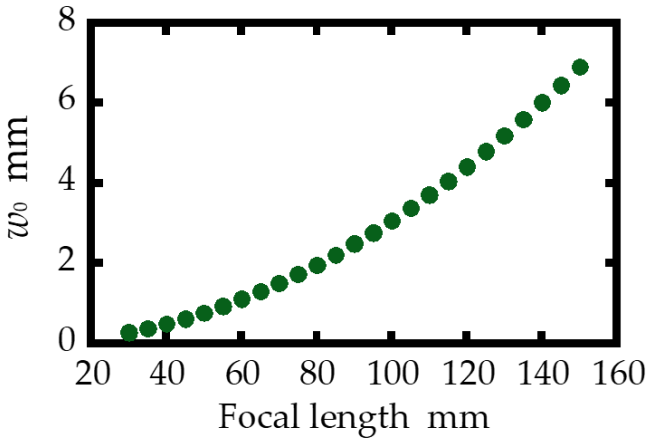

Figure 2.13 Beam radius characteristic over the different focal lengths of lens

It should be noted that the different focal length can influence the Rayleigh length and effective length of the crystal in the focal area inside the crystal. Figure 2.14 shows the relationship between the Rayleigh length and focusing ratio (effective length of the crystal) over the different focal length of the lens. It can be seen that the strong focused beam leads to the narrow Rayleigh length. The narrower Rayleigh length can generate the higher SHG however, the angle of divergence is getting bigger that can reduce the SHG power. This opposite condition is unavoidable in the use of focused beam and

must be considered in order to gain higher fundamental wave intensity experimentally.

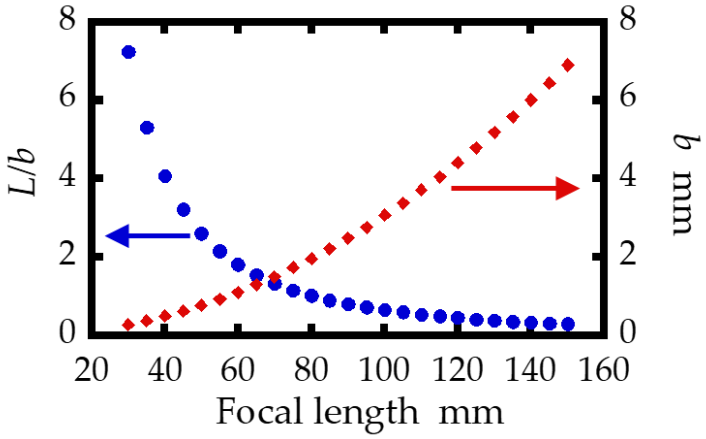

Figure 2.14 The relationship between Rayleigh length (red sign) and the focusing ratio (blue sign) over the focal length of the lens

2.6.2 Nonlinear optical crystal characteristic in generating second harmonic wave

The characteristics of SHG depend on the phase-matching condition of the material. As it is mentioned in the previous section, in the use of NLO crystals, the phase-matching condition of different NLO crystals requires a different phase-matching angle. Let λ_{ω} and $\lambda_{2\omega}$ be rewritten as λ and λ' to describe the fundamental wavelength and the second harmonic wavelength, respectively, with the relation of both wavelength is $\lambda' = \lambda/2$. Then the Equation (2.19) can also be rewritten as

$$\theta_{\mathrm{m}} = \sin^{-1}\left(\sqrt{\frac{n_{\mathrm{o}}^{-2}(\lambda) - n_{\mathrm{o}}^{-2}(\lambda')}{N_{\mathrm{e}}^{-2}(\lambda') - n_{\mathrm{o}}^{-2}(\lambda')}}\right). \tag{2.44}$$

The refractive index of the o-ray and e-ray can be calculated using the Sellmeier equation. The Sellmeier equation shows the empirical relationship between refractive index and wavelength for a particular transparent medium such as NLO crystal given by the following form [20]

$$N_e\left(\lambda'\right), n_o\left(\lambda'\right) = \sqrt{A + \frac{B}{\lambda'^{\,2} - C} - D\lambda'^{\,2}} \tag{2.45}$$

$$n_o\left(\lambda\right) = \sqrt{A + \frac{B}{\lambda^2 - C} - D\lambda^2} \tag{2.46}$$

.

Here, the coefficients A, B, C, and D, are the medium-specific constants for specific NLO crystals. Since the Fs laser is used as the laser source, the fundamental wavelength is ranging from 1480 nm to 1640 nm. In this chapter, we introduce several uniaxial crystals, beta barium borate (BBO), lithium niobate ($LiNbO_3$) coated by MgO, and lithium iodate ($LiIO_3$) confirm the phase matching characteristics of those crystals related to the given fundamental wavelength. From the reference [21] the medium-specific constants to calculate the refractive index, are tabulated in Table 2.1.

Table 2.1 The medium-specific constants for several NLO crystals.

Coefficients		**Crystals**		
		BBO	$LiIO_3$	MgO: $LiNbO_3$
A [-]	For n_o (θ=0°)	2.7359	3.4132	4.91296
	For N_e (θ=90°)	2.3753	2.9211	4.54528
B [μm^{-2}]	For n_o (θ=0°)	0.01878	0.0476	0.116275
	For N_e (θ=90°)	0.01224	0.0346	0.091649
C [μm^2]	For n_o (θ=0°)	0.01822	0.0338	0.048398
	For N_e (θ=90°)	0.01667	0.0320	0.046079
D [μm^{-2}]	For n_o (θ=0°)	0.01354	0.0077	0.0273
	For N_e (θ=90°)	0.01516	0.0042	0.0303

Figure 2.15a shows the refractive indices characteristic of BBO crystal over the wide range of wavelength in which the inset figure shows the refractive indices for the given wavelength range from 1480 nm to 1640 nm. By the given wavelength, it is expected to generate the second harmonic in the wavelength range from 740 nm to 820

nm. Figure 2.15b shows the characteristic of the phase-matching angle of BBO over each mode of a given wavelength. It can be seen in the Figure that the dispersion range of the phase-matching angle for BBO is 0.08° between the phase-matching angle range from 19.85° to 19.93°.

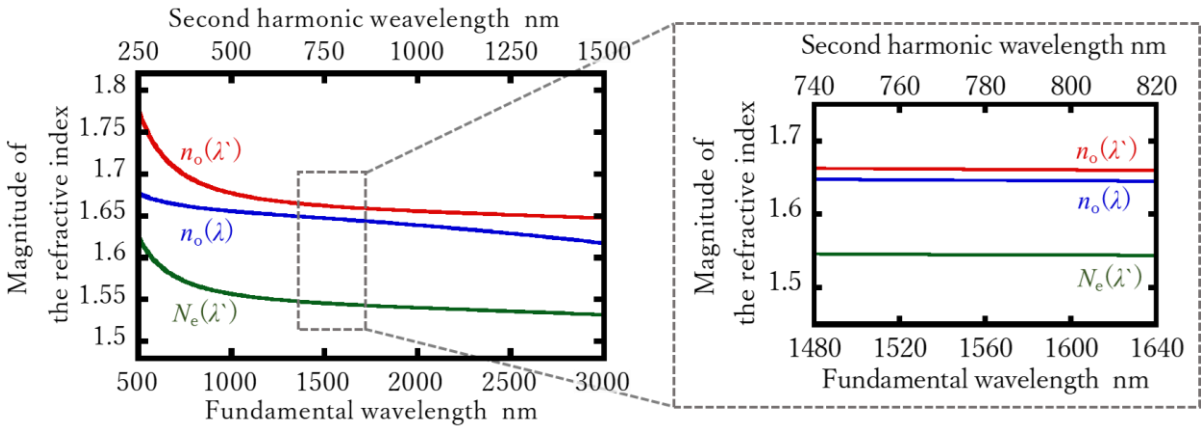

(a)

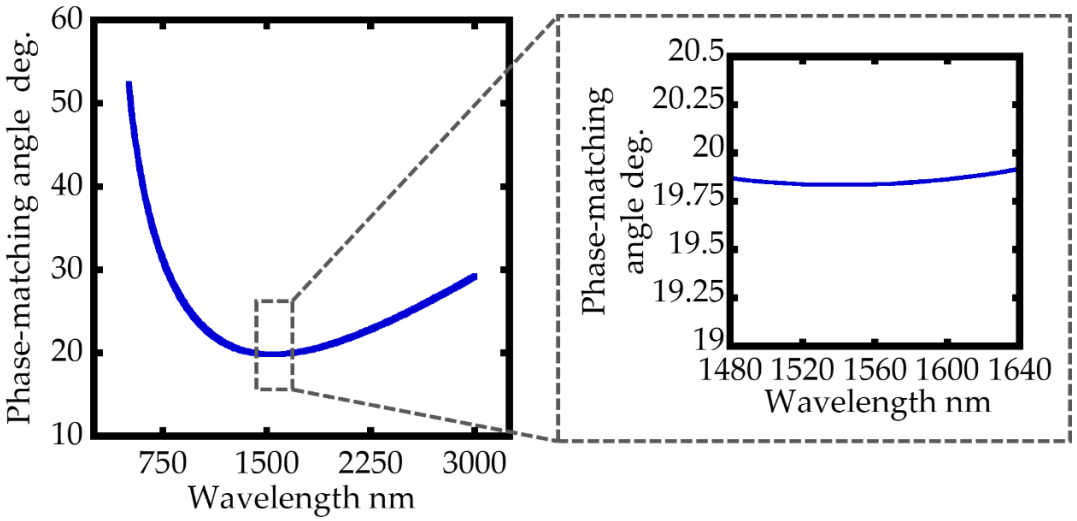

(b)

Figure 2.15 The nonlinearity of BBO crystal over the given wavelength from 1480 nm to 1640 nm; (a) The refractive indices characteristics of o-beam and e-beam inside the crystal; (b) The phase-matching angle characteristics.

Figure 2.16a shows the refractive indices characteristic of $LiIO_3$ crystal with respect to the change of fundamental wavelength. Meanwhile, Figure 2.16b shows the characteristic of the phase-matching angle of $LiIO_3$ over each mode of a given

wavelength. The angular dispersion of calculated phase matching angle is approximately 2.50° between the angular positions of 20.55° and 22.05° from the optical axis of the crystal, can be observed in the wavelength range from 1480 nm to 1640 nm which is wider that the dispersive angle of BBO crystal.

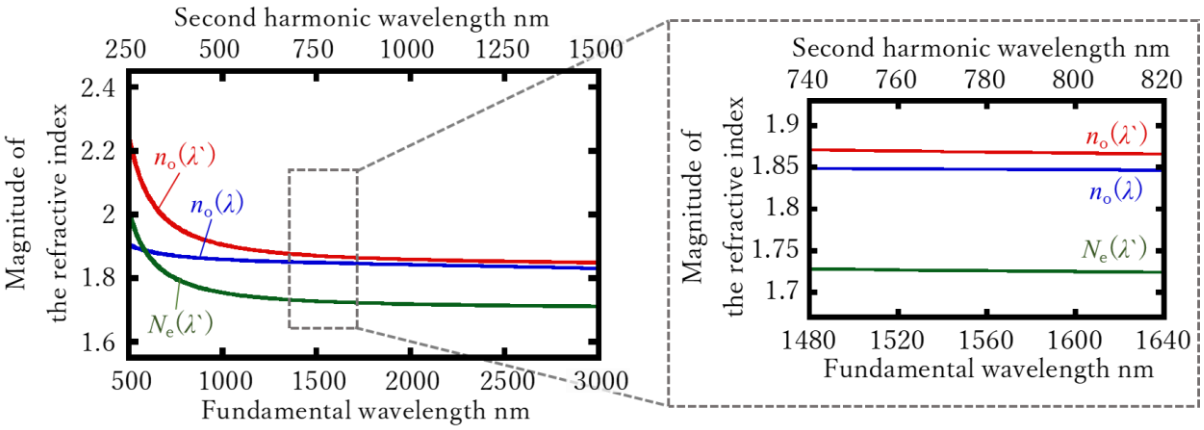

(a)

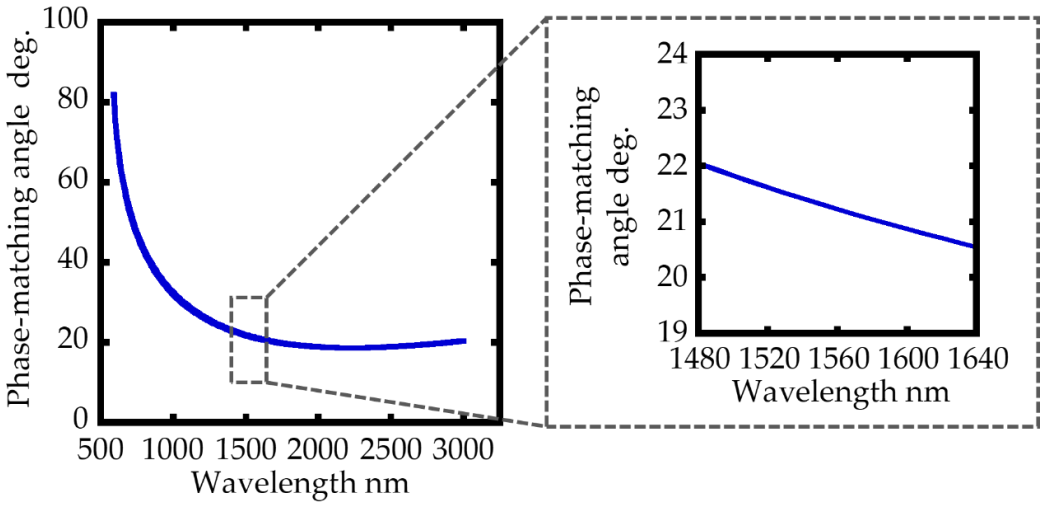

(b)

Figure 2.16 The nonlinearity of $LiIO_3$ crystal over the given wavelength from 1480 nm to 1640 nm; (a) The refractive indices characteristics of o-beam and e-beam inside the crystal; (b) The phase-matching angle characteristics.

Figure 2.17a shows the refractive indices characteristic of MgO:$LiNbO_3$ crystal over the change of wavelength. Meanwhile, Figure 2.17b shows the characteristic of the phase-matching angle of MgO:$LiNbO_3$ over each mode of a given wavelength. As can

be seen in the figure, an angular dispersion of approximately 2.87° between the angular positions of 48.50° and 51.37° from the optical axis of the crystal, can be observed in the wavelength range from 1480 nm to 1640 nm.

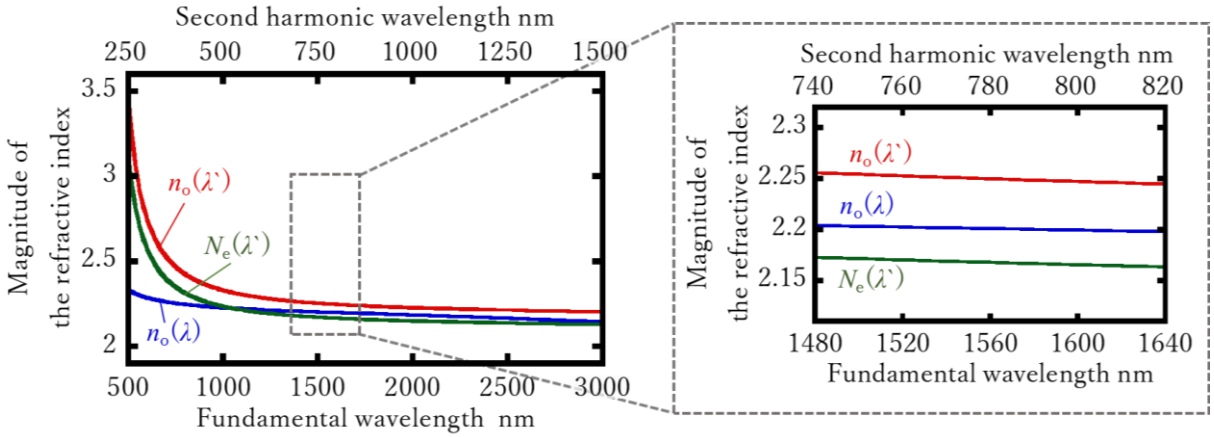

(a)

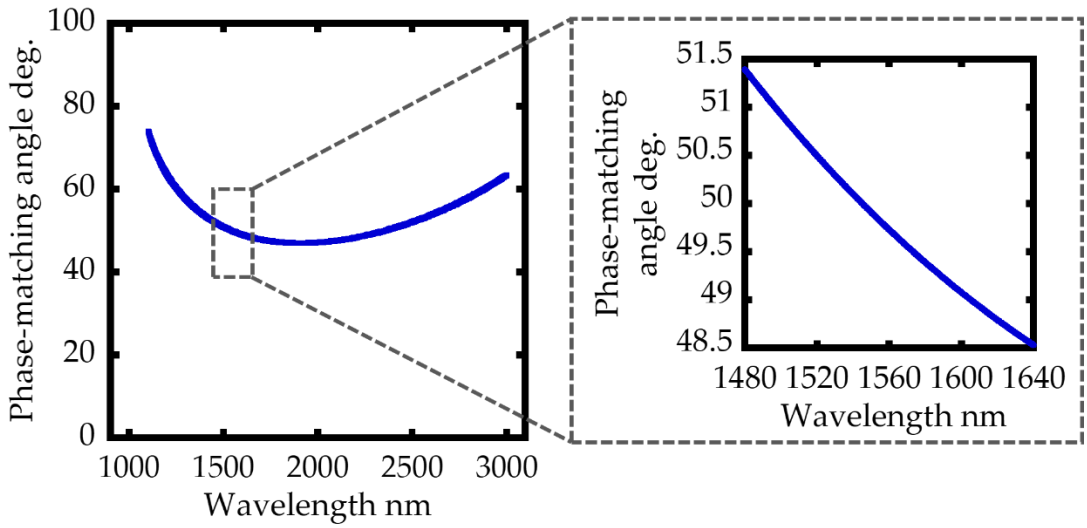

(b)

Figure 2.17 The nonlinearity of MgO:$LiNbO_3$ crystal over the given wavelength from 1480 nm to 1640 nm; (a) The refractive indices characteristics of o-beam and e-beam inside the crystal; (b) The phase-matching angle characteristics.

2.7 Summary

SHG is one nonlinear optical phenomenon in which a fundamental wavelength interaction with nonlinear material can generate the second harmonic wave with

doubled frequency. For generating the efficient SHG, there are features that must be fulfilled. First, the fundamental wave intensity must be sufficiently high over a certain propagation length because for small conversion efficiencies at least SHG is proportional to I_2. This condition can be achieved by using a high-power laser source. Second, the nonlinear medium must have a high second-order nonlinear coefficient, therefore a careful choice of the NLO crystal is necessary. Lastly, the light beams involved need to preserve their phase relation over the propagation length. This condition requires additional measures since dispersion generally leads to a phase mismatching between the FW and SHW. However, this problem can be overcome in the birefringence crystal by choosing a particular orientation. Since the phase-matching can be occurred in the one angle matching for respective wavelength, the Fs laser that contains of wide range of wavelength is the suitable laser source for the proposed angle sensor instead of the monochromatic laser source. Based on that, the change in SHG spectrum can be used to indicate the change of angular position of the target that represented by NLO crystals. In this chapter, BBO, $LiIO_3$, and $MgO:LiNbO_3$ crystals are theoretically evaluated. Calculations show that for a wavelength range from 1480 nm to 1640 nm, BBO crystals have a dispersion angle of 0.08° between 19.85° to 19.93°. LiIO3 crystals have a dispersion angle of 2.50° between the angular positions of 20.55° and 22.05°, and $MgO:LiNbO_3$ has a dispersion angle of approximately 2.87° between 48.50° and 51.37°. These characteristics are used in selecting the appropriate NLO crystal for the angle sensor configuration.

2.8 References

1. Mills, D.L. *Nonlinear Optics*. Springer-Verlag: Berlin, Heidelberg, 1991.
2. Shen, Y.R. *The Principles of Nonlinear Optics.* A Wiley-Interscience Publication: New York, 1984
3. Boyd, R.W. *Nonlinear Optics*, 2nd ed. Academic Press: San Diego, USA, 2003.
4. Hu, C.Y.; He, H.J.; Chen, B.Q.; Wei, Z.Y.; Li, Z.Y. Theoretical solution to second-harmonic generation of ultrashort laser pulse. *J. Appl. Phys.* **2017**, *122*, 243105.

5. Astuti, W.D.; Matsukuma, H.; Nakao, M.; Li, K.; Shimizu, Y.; Gao, W. An optical frequency domain angle measurement method based on second harmonic generation. *Sensors* **2021**, *21*, 670
6. Guenther, B.D. *Encyclopedia of Modern Optics*. Elsevier: Amsterdam, 2005
7. Dmitriev V.G.; Gurzadyan G.G.; Nikogosyan D.N. *Handbook of nonlinear optical crystals*, 3rd ed. Springer; Berlin 1999.
8. Manzoni, C. Cerullo, G. Design criteria for ultrafast optical parametric amplifiers. *J.Opt.* **2016**, *18*, 103501.
9. Trager, F. *Handbook of Laser and Optics*. Springer: New York, USA 2007
10. Sutherland, R.L. *Handbook of Nonlinear Optics*, 2nd ed. Marcel Dekker, Inc.: New York, USA, 2003.
11. Simon, D.S. *A guided tour of light beams*; Morgan & Claypool Publisher; Bristol, UK; 2016.
12. Hecht, E. *Optics*, 5th ed.; Pearson; London, UK; 2017
13. Simon, D.S. *A Guide Tour of Light Beams.* Morgan & Claypool Publisher: Bristol, UK, 2016.
14. Yu, H.; Kim, B.; Jang, S.G.; Kim, K.H.; Yoh, J.J. Performance characterization of a miniaturized exploding foil initiator via modified VISAR interferometer and shock wave analysis. *Journal of Applied Physics* **2017**, *121*, 215901.
15. U. Keller, "Recent developments in compact ultrafast lasers", Nature 424(6950), 831-838 (2003).
16. A. Yariv, and P. Yeh, "Photonics: Optical Electronics in Modern Communications, Sixth edition", Oxford University Press (2007).
17. S. Y. Set, H. Yaguchi, Y. Tanaka, and M. Jabionski, "Laser Mode Locking Using a Saturable Absorber Incorporating Carbon Nanotubes", Journal of Lightwave Technology 22(1), 51- 56 (2004).
18. D. J. Jones, S. A. Diddams, J. K. Ranka, A. Stentz, R. S. Windeler, J. L. Hall, and S. T. Cundiff, "Carrier-Envelope Phase Control of Femtosecond Mode-Locked Lasers and Direct Optical Frequency Synthesis", Science 288(5466), 635-639 (2000).
19. J. Zhu, P. Cui, Y. Guo, L. Yang, and J. Lin, "Pulse-to-pulse alignment based on interference fringes and the second-order temporal coherence function of optical frequency combs for distance measurement", Optics Express 23(10), 13069-13081 (2015).

20. Available online: https://www.castech.com/product/MgO%3ALiNbO3-113.html

21. Boyd, G.D.; Kleinman, D.A. Parametric interaction of focused Gaussian light beams. *J. Appl. Phys.* **1968**, *39(8)*; 3597–3639

Chapter 3
The design and construction of intensity-dependent second harmonic generation angle sensor

3.1 Introduction

In this chapter, a new principle of angle measurement based on intensity-dependent SHG with a femtosecond (Fs) laser is proposed. The characteristics of Fs in which it has the frequency comb over a wide spectral range with equally spaced (repetition rate) of each mode as well as high peak power and high-intensity electric field, are expected to have a merit to be applied in angle sensor [1]. To develop the angle measurement configuration with Fs laser as the source, the new measurement principle is required. Measurement based on a non-linear optical phenomenon on non-linear materials called second harmonic generation (SHG) [2,3], are proposed to be implemented in angle sensors with Fs lasers as laser source. Therefore, the motivation of this research is to explore the second harmonic wave generated by Fs laser in which it is known that the output power of the second harmonic wave correlates with an angle between wave vector and the crystal optic [1,2,4,5], called phase-matching angle, as it has explained in Chapter 2.

The fundamental characteristics of the proposed method are at first investigated through theoretical analysis, followed by basic experiments of angle measurement for demonstrating the feasibility of the proposed method. Since the incident angle between the nonlinear optical element and the laser beam axis is an important parameter, the incident angular characteristics of second harmonic generation are calculated for several nonlinear optical elements. In addition, the dependence of the SHG intensity on the angular displacement is also calculated. For the basic experiments of angle measurement, a prototype optical setup employing a beta barium borate (BBO) crystal as the nonlinear crystal is designed and constructed. A raytracing calculation is carried out to further investigate the validity of the experimental results.

3.2 An intensity-dependent angle measurement principle

The principle of the angle sensor based on SHG with intensity-dependet is presented in this section. The Fs laser as the fundamental laser source that passed on the NLO crystal will generate the second harmonic wave if the phase-matching condition is satisfied. As previously mentioned in Chapter 2, the phase-matching condition requires the matching angle, the angle between the light wave vector and the optical axis of the uniaxial NLO crystal. Since the Fs laser consist of wide range of wavelength, it is possible to make a series of angle matching as the NLO crystal rotated. It must be noted that the uniaxial NLO crystals have respective characteristics of angle matching, therefore it is necessary to choose the suitable NLO crystal for the proposed angle sensor.

Figure 3.1 shows a schematic of the optical setup for the proposed optical angle measurement method in the intensity-dependent based on SHG with a femtosecond laser. The optical setup is mainly composed of a Fs laser source, a photodetector, and a nonlinear crystal mounted on a measurement target, which rotates about the Y-axis in the figure. The optic axis of the nonlinear crystal is aligned to be parallel to the XZ plane in the figure. A collimated beam from a femtosecond laser with a beam diameter of d as the fundamental wave from the laser source, which is also aligned to be parallel

to the XZ plane, is made incident to the nonlinear crystal to generate second-harmonic waves. Since the power of the generated second harmonic wave $p_{2\omega}$ depends on the angle θ between the optic axis of the nonlinear crystal and the axis of the incident laser beam, θ can be obtained by detecting $p_{2\omega}$ with the photodetector.

Assume that the ordinary and extraordinary axes of the nonlinear crystal are aligned to be parallel to the Y and X-axes, respectively, while the incident fundamental wave and the second harmonic wave are polarized in the Y- and X-directions, respectively. Denoting the power of the incident fundamental wave as p_{ω}, the relationship between $p_{2\omega}$ and θ can be expressed by Equation (2.14) in Chapter 2

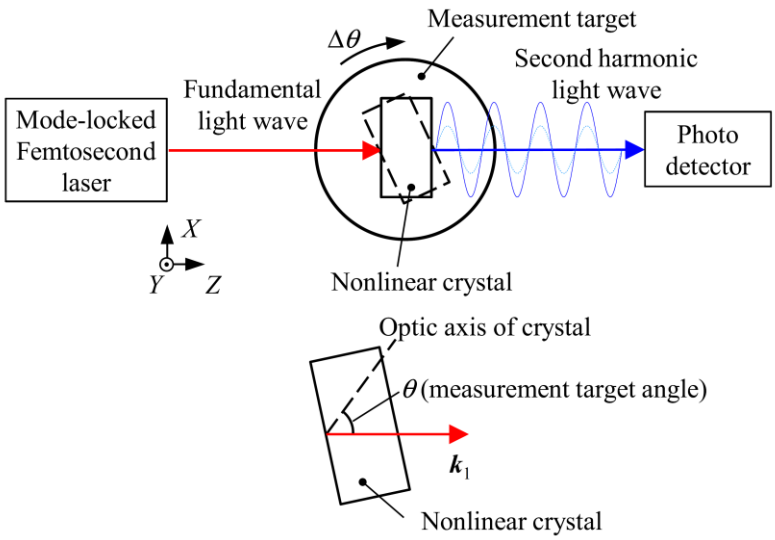

Figure 3.1 The schematic of the optical setup for the proposed optical angle measurement method based on SHG with a collimated femtosecond laser beam [6].

In the case with a uniaxial birefringent crystal such as beta barium borate (BBO), regarding the refractive index ellipse shown in Figure 3.2a, the angle θ_m referred to as the matching angle that satisfies $n_o(\lambda_1)=n_e(\theta_m, \lambda_2)$, as well as $\Delta k(\theta_m)=0$, can be found; this procedure is known as the index matching.

It should be noted that $p_{2\omega}$, which is the sum of the second harmonic waves generated in the nonlinear crystal, is also proportional to the square of p_{ω}, as can be seen in Equation (2.14) in Chapter 2. At a position where the incident fundamental wave generates the second harmonic wave, the two are coherent with each other. The fundamental wave continues to generate additional contributions of the second

harmonic wave while propagating through the nonlinear crystal. In the case where the phase is mismatched $n_o(\lambda_1) \neq n_e(\theta_m, \lambda_2)$, as shown in Figure 3.2b, effective SHG cannot be accomplished due to the different propagating speeds of the fundamental and second harmonic waves in the crystal. Meanwhile, in the case where the phase is matched, as shown in Figure 3.2c, all the second harmonic waves are combined totally constructively, and $p_{2\omega}$ can be maximized. As described above, efficient SHG can be accomplished by the index matching. Although the angle-dependence of SHG is a well-known phenomenon, in this paper an attempt is made to utilize the phenomenon for detecting small angular displacement of the nonlinear crystal.

It is noted that, in addition to mode-locked femtosecond lasers, other pulsed laser sources such as *Q*-switched Nd: YAG lasers can also generate second harmonic waves. However, femtosecond lasers are more stable in output powers, and therefore more suitable for angle measurement based on SHG than other pulsed laser sources. Therefore, a femtosecond laser is more suitable for stable angle measurement based on SHG, which is a nonlinear process associated with optical power.

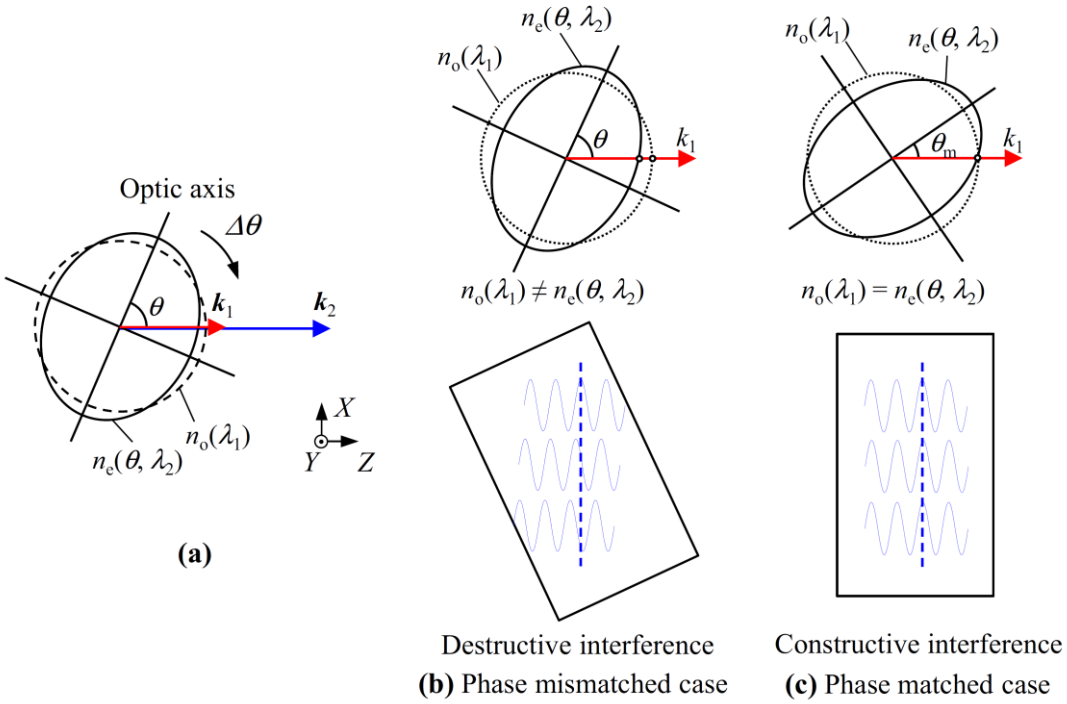

Figure 3.2 The schematic of the second harmonic generation; (**a**) Refractive index ellipse of a negative uniaxial crystal; (**b**) The phase mismatching condition; (**c**) The phase matching condition [6].

3.3 Theoretical calculation on the angle measurement sensitivity

To estimate the sensitivity of angle measurement by the proposed method based on SHG, theoretical calculations are carried out in the wavelength range from 1500 nm to 1640 nm. The selection a nonlinear crystal that appropriate for the proposed optical angle measurement method with a specific mode-locked femtosecond laser source is conducted. The sensitivity of the proposed angle sensor depends on the phase matching angle characteristic of NLO crystal with respect to the given wavelength. The characteristic of several uniaxial crystal has been mentioned in the previous Chapter. As the comparison, Figure 3.3 exhibits the wavelength dependence of phase-matching angle mentioned in Chapter 2, BBO, $LiIO_3$ and $MgO:LiNbO_3$. As can be seen in the figure, the dispersion of the phase matching angle of BBO is found to be smaller than those of $LiIO_3$ and $MgO:LiNbO_3$ in the wavelength range; this wavelength-independent characteristic of the phase matching angle of BBO is ideal for the proposed optical angle measurement method based on the SHG.

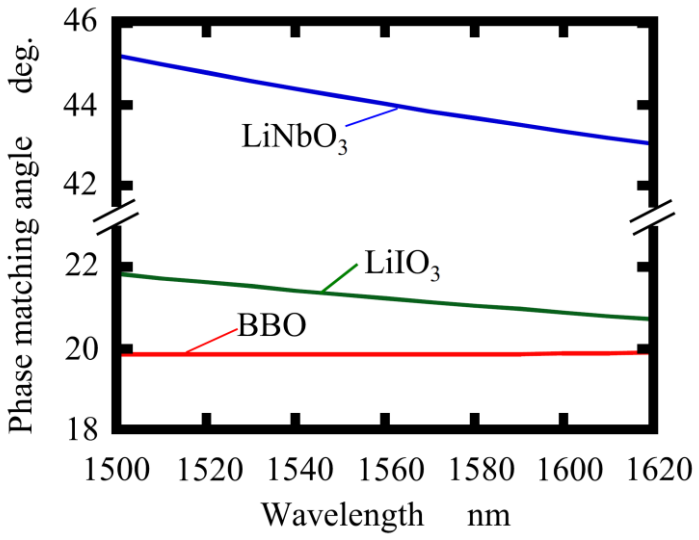

Figure 3.3 The wavelength dependence of phase matching angle for several uniaxial crystals.

By using the calculated phase matching angles shown in Figure 3.3, The sinc quadratic function in Equation (2.14) for each crystal is also calculated. Figure 3.4a

shows the results, which are referred as the response curves showing the relationship between the power of the second harmonic wave $p_{2\omega}$ and the angle θ. In the figure, the sinc quadratic function term is calculated for the cases with wavelengths of 1500, 1560, and 1620 nm. As can be seen in the figure, peaks of the curves for several wavelengths are almost overlapped with each other for the case with BBO crystal, while the peaks of the curves for the cases with $LiIO_3$ and $MgO:LiNbO_3$ are not. In the proposed angle measurement method, the photo detector detects the power of second harmonic waves regardless of the wavelength. The integrated values of the sinc quadratic function in the spectral range are therefore calculated to simulate the photodetector output. Figure 3.4b shows the result. The peak of the response curve for BBO crystal is several times higher than those for $LiIO_3$ and $MgO:LiNbO_3$. In addition, the variation of the photodetector output with BBO crystal is similar to the $\mathrm{sinc}^2[\Delta k(\theta)L/2]$ curve shown in Figure 3.4a. Meanwhile, those for $LiIO_3$ and $MgO:LiNbO_3$ are significantly different from the $\mathrm{sinc}^2[\Delta k(\theta)L/2]$ curves. Here, the sensitivity of the angle measurement system is defined as the slope of second harmonic wave power to angular displacement. The relative sensitivities of the second harmonic wave to angular displacement in the range between 45 and 55% of the peaks at the left shoulders of the curves in Figure 3.4b. The BBO crystal has relative sensitivity of 1 arbitrary unit, meanwhile $LiIO_3$ and $MgO:LiNbO_3$ have the relative sensitivity of 0.16 and 0.091, respectively. BBO crystal is therefore suitable for the optical setup with the erbium-doped fiber laser employed in the following experiments

The calculations are also carried out to obtain the response SHG power for several focal length; 40 mm, 75 mm, and 150 mm in the case of focused beam using Equation (2.27). The parameter used in the calculation is tabulated in Table 3.1. Need to be noted that the wavelength used in calculation is the central wavelength of the Fs laser. The fundamental power in the parameter is the highest output power of Fs laser.

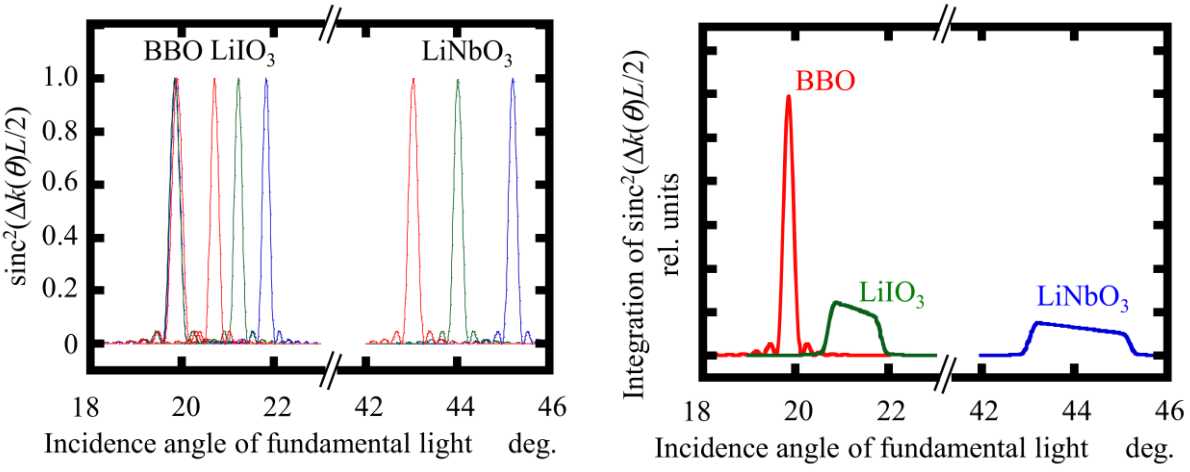

(a) (b)

Figure 3.4 The calculated response curves of second harmonic wave power with respect to angular displacement for a collimated Fs laser beam; (**a**) $\mathrm{sinc}^2[\Delta k(\theta)L/2]$ for wavelengths of 1500 nm (blue lines), 1560 nm (green lines), and 1620 nm (red lines); (**b**) The integrated value of $\mathrm{sinc}^2[\Delta k(\theta)L/2]$ with respect to a wavelength between 1500 nm and 1620 nm.

Table 3.1 Parameter used in the simulation of SHG.

C [W^{-1}]	p_ω [W]	λ [nm]	L [mm]	d [mm]	f [mm]
					40
3.66×10^{-9}	1000	1560	2.0	3.6	75
					150

Figure 3.5 shows the calculated response curve of SHG power over the angular change of the BBO crystal. It can be seen that the response curves showed a similar trend to the result of BBO shown in Figure 3.4b where a collimated beam with a large power is employed, indicating the possibility of angle measurement based on SHG with a focused laser beam. On the other hand, the full width at half maximum (FWHM) of the response curve in Figure 3.5 is wider than that of BBO in Figure 3.4b. It means that the sensitivity of angle measurement based on SHG with a focused laser is lower than that with a collimated beam. The second harmonic wave power in Figure 3.5 is found to be increased as the decrease of the focal length. This was mainly due to the smaller laser spot diameter with smaller focal length, since the irradiance of second

harmonic wave is proportional to the square of irradiance of the fundamental wave. This can be utilized to improve the sensitivity of angle measurement based on SHG with a focused laser beam.

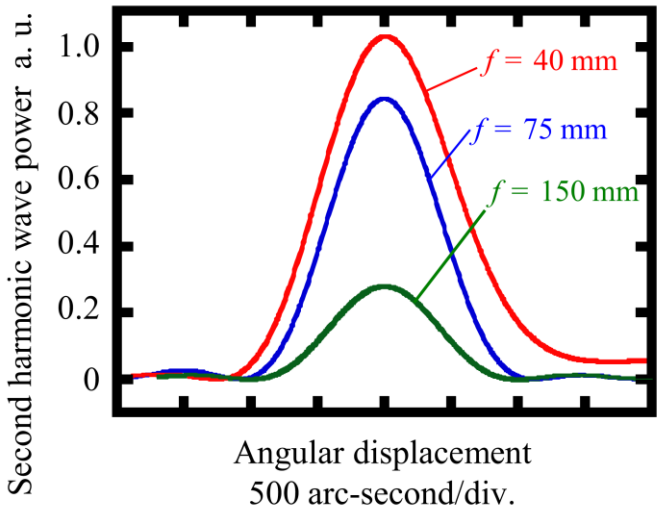

Figure 3.5 The calculated response curves of second harmonic wave power with respect to angular displacement for several focal length of focusing lenses.

3.4 Experiments design and procedures

The experiments were carried out to demonstrate the feasibility of the proposed angle measurement method based on SHG by using the developed prototype optical setup, a schematic of which is shown in Figure 3.3. A commercial mode-locked Fs laser (C-fiber, Menlo Systems) having a central wavelength of 1560 nm, was employed as the light source for the setup. The Fs laser emitted from a single-mode optical fiber was collimated by the collimating beam with diameter d of 3.6 mm. It must be noted that the collimated Fs laser with must have sufficient intensity and poser density to generate SHG. In the case of using a low output power Fs laser, it is effective to intensifying the laser beam by focusing the laser beam in a nonlinear crystal to generate the second harmonic wave although the applications of such an angle sensor with a focused laser beam are limited. The technique of focused laser beam for SHG shown in Figure 2.4 of Chapter 2, in which the laser spot diameter can be estimated by Equation (2.24) in the previous chapter. To ensure the outcome of the laser focusing

method in generating the second harmonic wave, the spectrum of both the generated second harmonic wave and the unconverted fundamental wave is observed experimentally as schematically shown in Figure 3.6.

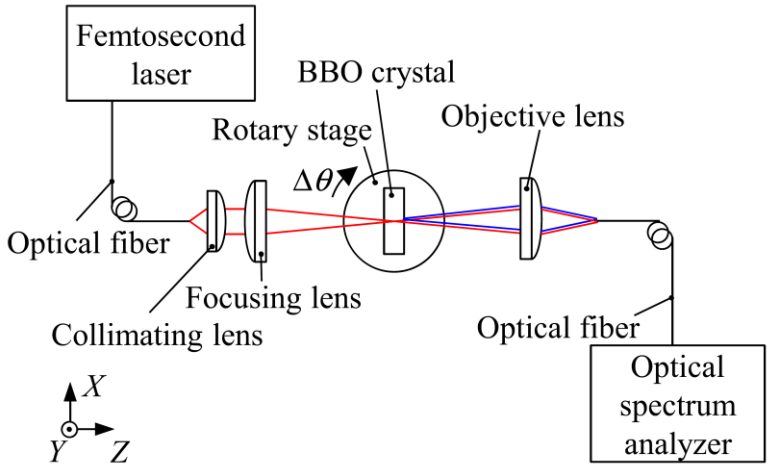

Figure 3.6 Schematic of the experimental setup for observing spectra of fundamental and second harmonic waves [6].

As can be seen in the figure, the collimated laser beam whose polarization direction is parallel to the *Y*-axis was focused into a nonlinear crystal mounted on a rotary stage by an achromatic focusing lens with a focal length of 40 mm. A type I BBO crystal, in which the angle between its optic axis and the crystal surface was designed to be its matching angle, was employed as the nonlinear crystal. By using an objective lens, both the generated second harmonic wave and the unconverted fundamental wave were coupled into a multimode fiber and observed by an optical spectrum analyzer (OSA). The BBO crystal mounted on the rotary stage representing the measurement target was rotated at 48 arc-second intervals corresponding to 500 pulse intervals of the stepping motor controller to observe the total power of the SHG spectrum with respect to the change in angular position and to investigate the angle-dependence of the spectrum of the second harmonic wave.

According to Equation 2.14 in Chapter 2, a higher power p_ω or p_1 of the fundamental wave contributes to an increase in $p_{2\omega}$ or p_2. Therefore, an optical setup adjustment is needed to optimize the focusing of the fundamental light beam in the

BBO crystal. Since the beam spot diameter is one of important parameter in producing higher power density, the focal length *f* of the focusing lens can be changed according to Equations 2.24 and 2.26 in Chapter 2. The influence of focused laser beam diameter was therefore evaluated in experiments by using several focusing lenses having different focal lengths (40 mm, 75 mm, and 150 mm). The specification of the lens with the focal length of 40 mm.

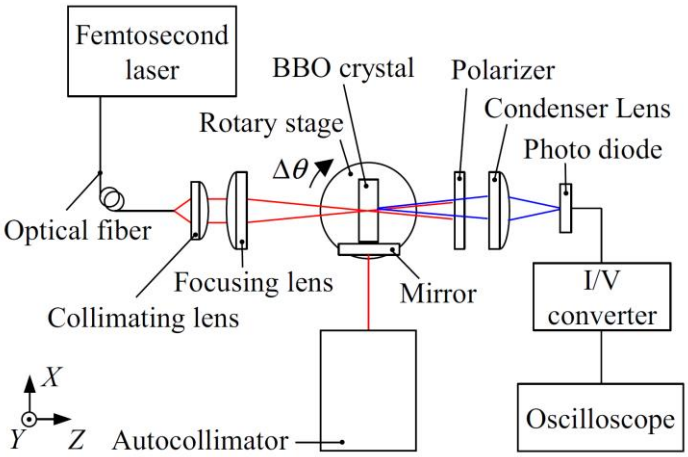

(a)

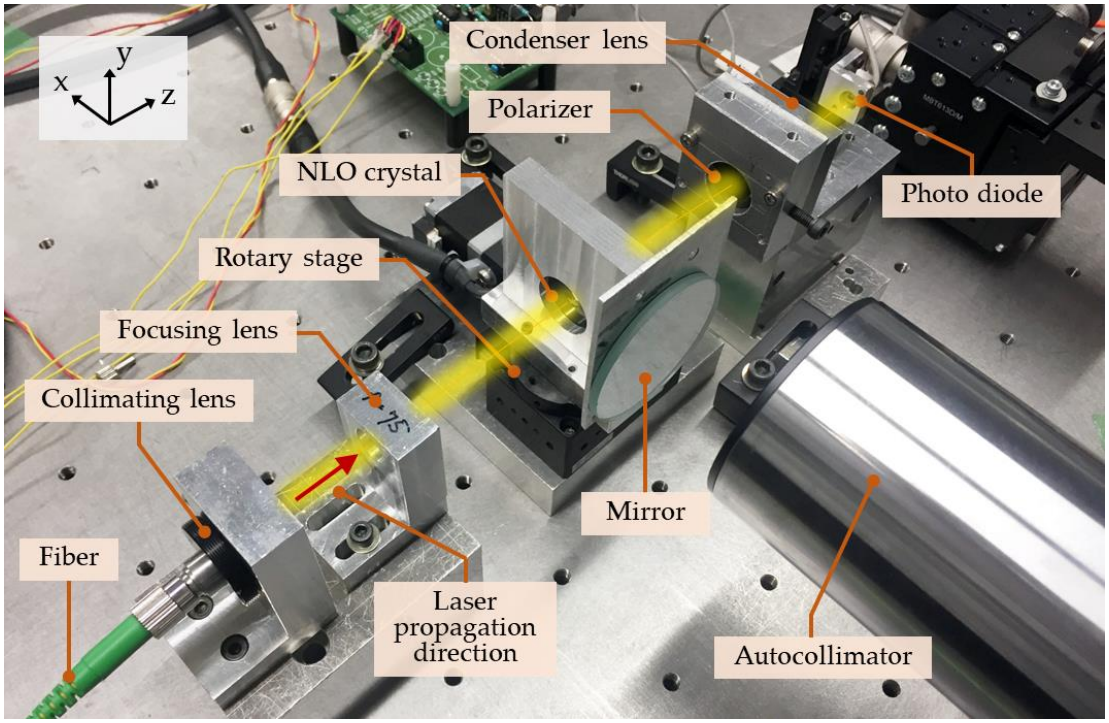

(b)

Figure 3.7 Experimental setup of the intensity-dependent angle sensor (**a**) A schematic of proposed angle sensor [6]; (**b**) A photograph of the experimental setup.

Figure 3.7a shows the schematic of the optical setup for the proposed angle measurement method based on SHG, and Figure 3.7b shows the photograph of the experimental setup. It can be seen in the figure, the BBO crystal mounted on a precision rotary table was placed at the focal plane of the focusing lens. To reduce the influence of chromatic aberration, achromatic doublet lenses were employed as the focusing lens. A polarizer was placed just behind the BBO crystal in such a way that the transmission axis of the polarizer was set to be parallel to *X*-axis so that the second harmonic light wave could transmit the polarizer, while the unconverted fundamental light wave could be absorbed. The transmitted second harmonic light wave was detected by a photodiode with a cutoff frequency of 30 MHz. The photocurrent signal from the photodiode was converted into the corresponding voltage signal by a trans-impedance amplifier, and was captured by an oscilloscope. The angular displacement was given to the BBO crystal by the rotary table. A flat mirror was also mounted on the rotary table so that the angular displacement given to the BBO crystal could be verified by a commercial autocollimator employed as a reference. All experiment equipment specifications in this research are shown in Table 3.2 to Table 3.18.

Table 3.2 The specification of the femtosecond pulse laser source

Components	**Value**
Manufacturer	Menlo Systems GmbH
Model number	C Fiber (C Side)
Wavelength	1560 nm +/- 20 nm
Average Output Power	>15 mW
Pulse Width	<150 fs
Repetition Rate	100 MHz
Repetition Rate Instability	±1 MHz

Table 3.3 Specification of the rubidium frequency standard

Components	Value
Manufacturer	Stanford Research Systems, Inc.
Model number	FS725
Output frequencies	10 MHz
Amplitude	0.5 rms, ±10%
Accuracy	$\pm 5\times10^{-11}$
Short time stability (Allan variance)	$<2\times10^{-11}$ (1 s) $<1\times10^{-11}$ (10 s) $<2\times10^{-12}$ (100 s)

Table 3.4 Specification of the frequency synchronizer.

Components	Value
Model number	RRE-SYNCRO
RMS Timing Jitter	<200 fs (0.1 Hz – 500 kHz) or same as reference Whichever applies first

Table 3.5 The specification of the collimating lens.

Components	Value
Manufacturer	Thorlabs Japan Inc.
Model number	F280FC-1550
Alignment wavelength	1550 nm
Focal length	18.75 mm
Collimating diameter	3.6 mm
Theoretical divergence	0.032°
AR Coating	1050–1620 nm

Table 3.6 Specification of the single-mode fiber.

Components	Value
Manufacturer	OPTOKON Co., Ltd.
Model number	NPC-28S2D-J-001
Type	FC Patchcord (FC/APC)
Fiber cable model	G652D (Single mode fiber)
Mode field diameter	10.4±0.5 mm at 1550 nm

Table 3.7 The specification of the linear polarizer.

Components	Value
Manufacturer	Thorlabs Japan Inc.
Model number	LPNIR050-C
Extinction Ratio	>1000:1 at 1050–1700 nm
Diameter	12.5 mm

Table 3.8 The specification of BBO crystal.

Components	Value
Manufacturer	CASTECH Inc.
Name	BBO (β-BaB_2O_4)
Diameter	6.00 mm × 6.00 mm
Thickness	2(±0.1) mm
Angle Tolerance	θ=19.8°±0.25°
	ϕ=0°±0.25°
Flatness	≤ λ/8 at 633 nm
Coating	S1: P-1560 nm
	S2: P-780 nm

Table 3.9 The specification of the focusing lens (*f*=40 mm).

Components	**Value**
Manufacturer	Edmund Optics Japan Co.
Model number	#45-796
Type	Achromatic Lens
Focal length	40.0 mm at 880.0 nm
Diameter	12.0 mm
Coating	NIR II R_{avg}≤0.7% at 750–1550 nm

Table 3.10 The specification of the focusing lens (*f*=75 mm).

Components	**Value**
Manufacturer	Edmund Optics Japan Co.
Model number	#45-799
Type	Achromatic Lens
Focal length	75.0 mm at 880.0 nm
Diameter	12.0 mm
Coating	NIR II R_{avg}≤0.7% at 750–1550 nm

Table 3.11 The specification of the focusing lens (*f*=150 mm).

Components	**Value**
Manufacturer	Edmund Optics Japan Co.
Model number	#47-380
Type	Achromatic Lens
Focal length	150.0 mm at 880.0 nm
Diameter	25.0 mm
Coating	NIR II R_{avg}≤0.7% at 750–1550 nm

Table 3.12 The specification of the Photodiode.

Components	Value
Manufacturer	Hamamatsu photonics
Model number	S4204
Name	Si PIN photo diode
Size	4.1 mm×5 mm
Area of light receiving section	1 mm×2 mm
Wavelength range	320–1100 nm
Peak sensitivity wavelength	960 nm

Table 3.13 The specification of the Rotary stage.

Components	Value
Manufacturer	SURUGA SEIKI Co., Ltd.
Model number	KRB04017C
Travel Range	±8.5°
Resolution (pulse)	0.0067°(Full)
Repeatability positioning accuracy	±0.003°

Table 3.14 The specification of the commercial autocollimator

Components	Value
Manufacturer	MÖLLER-WEDEL OPTICAL GmbH
Name	ELCOMAT 3000
Model number	229919
Max measurement range	2000 arc-second × 2000 arc-second
Number of measuring axes	2
Resolution	0.005 arc-second
Accuracy	±0.1 arc-second over any 20 arc-second range ±0.25 arc-second over total range

Table 3.15 The specification of the stepping motor controller.

Components	Value
Manufacturer	SURUGA SEIKI Co., Ltd.
Model number	DS102MS
Driver type (division number)	Micro step (1-1/250)

Table 3.16 The specification of the digital oscilloscope.

Components	Value
Manufacturer	NIPPON AVIONICS Co., Ltd.
Model number	RA2300
Name	Omniace III
Resolution of A/D conversion	16 bits

Table 3.17 The specification of the fiber alignment stage.

Components	Value
Manufacturer	Thorlabs Japan Inc.
Model number	MBT613D/M

Table 3.18 The specification of the objective lens.

Components	Value
Manufacturer	Edmund Optics Japan Co.
Model number	#67-659
Type	Double-Convex Lens
Focal length	30.0 mm at 587.6 nm
Diameter	30.0 mm
Coating	NIR II $R_{avg} \leq 0.7\%$ at 750–1550 nm

3.5 Results and discussion

3.5.1 Evaluation of angle detection characteristics

Figures 3.8a and 3.8b show the observed spectra of the fundamental wave and the second harmonic wave, respectively. In each figure, the integrated laser power over the observed spectrum was also plotted. As can been seen in the figure, second harmonic waves were successfully generated. In Fig. 3.8b, a strong dependence of the power of the generated second harmonic wave on the angular displacement of the BBO crystal was observed, indicating the possibility of angle measurement based on SHG with a focused beam for a femtosecond laser source with a small power. The maximum conversion efficiency of the fundamental wave to the second harmonic wave was evaluated to be approximately 4%. The angle in which the intensity of the second harmonic wave reaches the maximum was considered to be that the incidence angle of the fundamental wave into the BBO crystal was matching angle. It should be noted that the observed second harmonic spectra were Gaussian-like ones, while the spectrum of the fundamental wave was flat; the root cause of this difference is mainly due to the chromatic aberration of the focused fundamental light wave, the details of which are explained in the following of this paper.

Experiments were carried out to evaluate the sensitivity of the developed optical arrangement. Figure 3.9 shows the photodiode response signal due to the angular displacement exerted on the BBO crystal obtained from the different focal lengths of the lens. As predicted in the theoretical calculation results in Figure 3.5, the power of the second harmonic wave was found to be higher with the decrease of focal length *f*. The observed powers of the second harmonic waves showed similar angular dependence compared with the simulation results. Meanwhile, the measurable angle range, in which the variation of the output signal from the PD can be observed, were found to be wider by several times compared with the range predicted in the simulation results. The sensitivity was evaluated as the steepest region of these curves as it is illustrated in Figure 3.10a, meanwhile the noise level was evaluated by checking the output stability in a certain period of time as it is illustrated in Figure 3.10b. To do

so, the rotary stage was fixed in the angle position in which the response voltage is approximately half of maximum response voltage of the SHG. The data was taken for 500 ms with interval of 1 ms. As the result, Figure 3.11 shows a typical noise component in the output signal from the PD in the case of using the lens with focal length of 75 mm. Furthermore, the measurement resolution of the developed angle measurement method was evaluated as the ratio of the noise component (2σ) to the sensitivity.

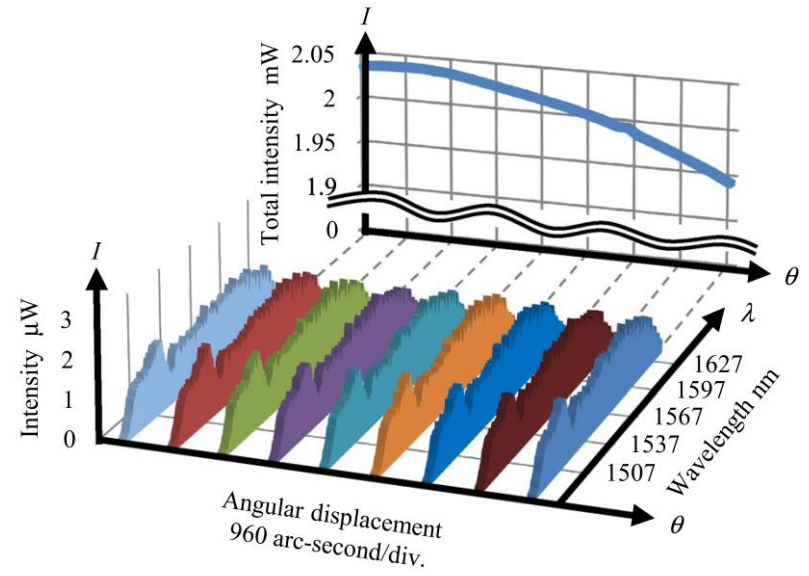

(a)

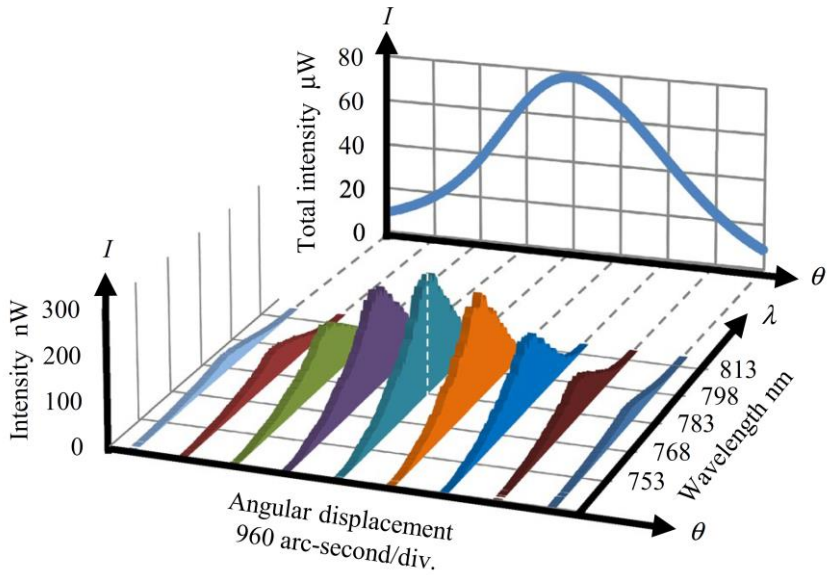

(b)

Figure 3.8 (**a**) Observed spectra and total power of the fundamental wave over the angular displacement of BBO crystal; (**b**) Observed spectra and total power of the second harmonic wave over the angular displacement of BBO crystal

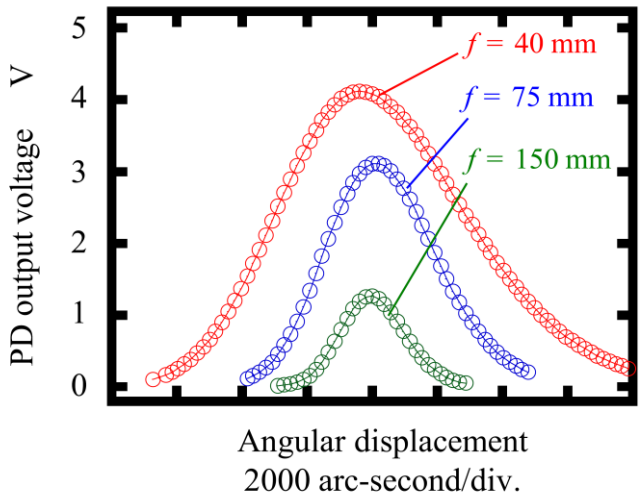

Figure 3.9 Experimental result of the SHG with angular displacement for several focal lengths of lenses

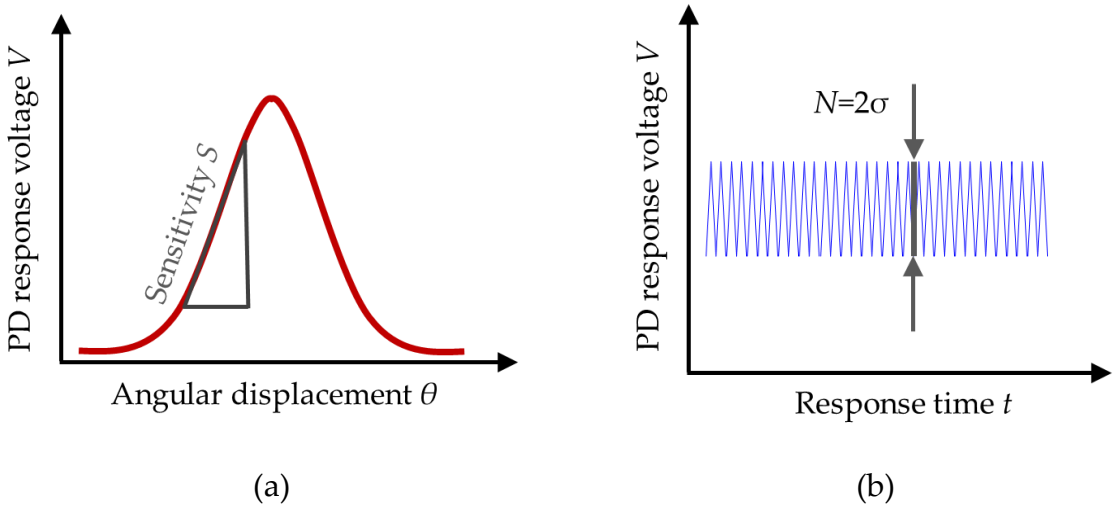

Figure 3.10 (a) The illustration of the measurement sensitivity determination; (b) The illustration of noise level observation.

The experiment results that show the characteristics of the proposed angle sensor for the use of different focal length of the lens are summarized in Table 3.19. From the results, it is known that the highest sensitivity is achieved with the use of lens with the focal length of 75 mm and a resolution of approximately 0.4 arc-second was estimated to be achieved by the developed setup.

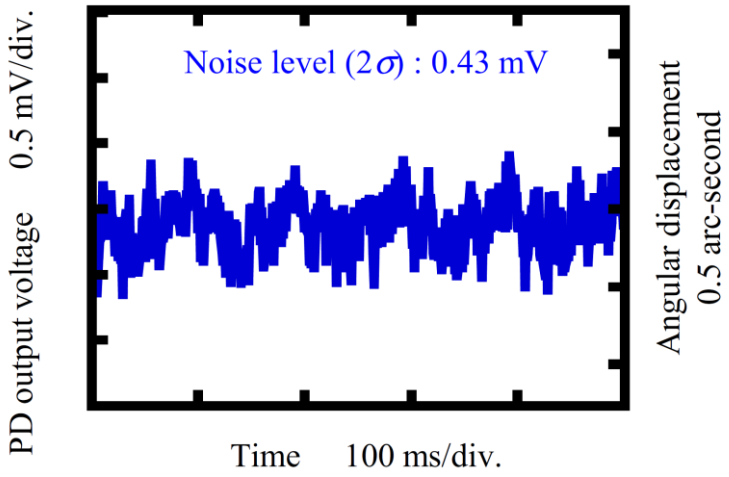

Figure 3.11 PD output stability for detection of SHG with focal length of 75 mm and cut-off frequency of 30 Mhz.

Table 3.19 Characteristics of the proposed angle sensor performance

Focal length mm	**Sensitivity mV/ arc-second**	**Noise level mV**	**Resolution arc-second**
40	0.97	0.44	0.45
75	1.18	0.43	0.36
150	0.79	0.37	0.47

Experiments were further extended to verify the resolution of the developed angle sensor with intensity-dependent measurement. The BBO crystal was rotated by the rotary table in a step of 0.4 arc-second, while the output signal from the PD was monitored. Figure 3.12 shows the variation of PD output observed during the experiment in which the output signal from the laser autocollimator is also plotted. As can be seen in the figure, it was verified that the developed angle measurement system could distinguish the given angular displacement. Meanwhile, as shown in Figures 3.5 and 3.8, the sensitivity of the developed angle measurement system observed in the experiments was lower than that predicted in theoretical calculation results. The chromatic aberration of the lens is considered one of the causes of differences in experimental and calculation results.

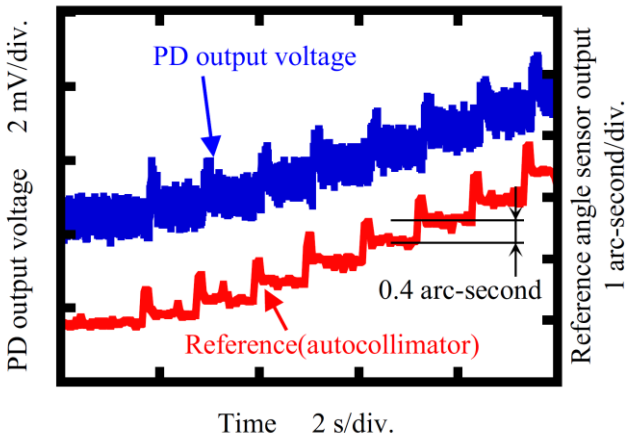

Figure 3.12 The measurement results using the proposed angle sensor (*f*=75 mm) with respect to the angular displacement in which the reference sensor output is also displayed.

3.5.2 Investigation of the chromatic aberration influence

As described in previous section, one of the causes of the difference in second harmonic characteristics between theory and experiment is considered to be the effect of aberrations in the optical system. To investigate the influence of the chromatic aberration, ray tracing is carried out for the developed optical setup. Ray tracing is the act of manually tracing a ray of light through a system by calculating the angle of refraction or reflection at each surface. This is the primary method to determine the performance of the optical system.

The optical model used for the ray tracing in this study is shown in Figure 3.13. In the model, an achromatic doublet lens composed of a N-LAK22 substrate and a N-SF6 substrate is employed as the focusing lens, where the data of ref [8] are used for Sellmeier equations of these glasses, and the refractive index of the substrates are shown in Equations (3.1) and (3.2). An achromatic lens used in the configuration is a lens that combines a spherical lens made of two different lens substrates to correct chromatic aberrations.

$$\text{N-LAK22: } n_1(\lambda)=\left(1+\frac{1.14229781\lambda^2}{\lambda^2-0.00585778594}+\frac{0.535138441\lambda^2}{\lambda^2-0.0198546147}+\frac{1.04088385\lambda^2}{\lambda^2-100.834017}\right)^{1/2} \quad (3.1)$$

$$\text{N-SF6: } n_2(\lambda)=\left(1+\frac{1.77931763\lambda^2}{\lambda^2-0.0133714182}+\frac{0.338149866\lambda^2}{\lambda^2-0.0617533621}+\frac{2.08734474\lambda^2}{\lambda^2-174.01759}\right)^{1/2} \tag{3.2}$$

The lens parameter to be used in the ray tracing method is summed up in Table 3.20. The curvature radius of each surface is denoted by R_1 for the surface 1, R_2 for the surface 2, and R_3 for the surface 3. Meanwhile, the center thicknesses are denoted by t_1 and t_2. The origin of the ray tracing is set at the center of the surface 1. A ray whose incidence axis is x_0 from Z-axis is refracted at surfaces 1, 2, and 3 in the figure, and then is refracted at surface 4 of the nonlinear crystal. The result of the ray tracing for the cases with a lens focal length of 40 mm is shown in Figure 3.14a for the case of the change in the crystal's angular position $\Delta\theta$ equal to 0°. In the figure, the results with wavelengths of 1500, 1560, and 1620 nm are plotted. Ray tracing is also carried out for the case with $\Delta\theta$ equal to 1°. The result is shown in Figure 3.14b. To clarify the influences of refraction at surface 4, ray tracing is also carried out for the case without BBO crystal. The result is shown in Figure 3.14c. Furthermore, to evaluate the influences of chromatic aberration of the focusing lens, a parameter ΔZ, which is the Z-directional distance between the focal positions of the rays with wavelengths of 1500 and 1620 nm, is introduced.

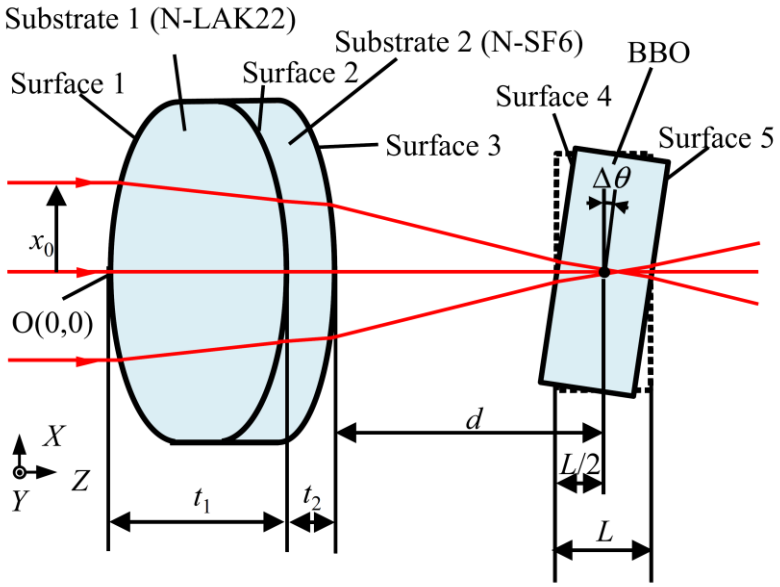

Figure 3.13 The system for calculation of ray tracing.

Table 3.20 The lens parameters in ray tracing method

Focal length	R_1	R_2	R_3	t_1	t_2	t_3
mm	**mm**	**mm**	**mm**	**mm**	**mm**	**mm**
40	22.81	42.11	84.66	4.5	2.5	36.4
75	21.91	42.30	84.66	3.0	2.5	72.4
150	250.49	565.11	1071.9	6.0	4.0	145.4

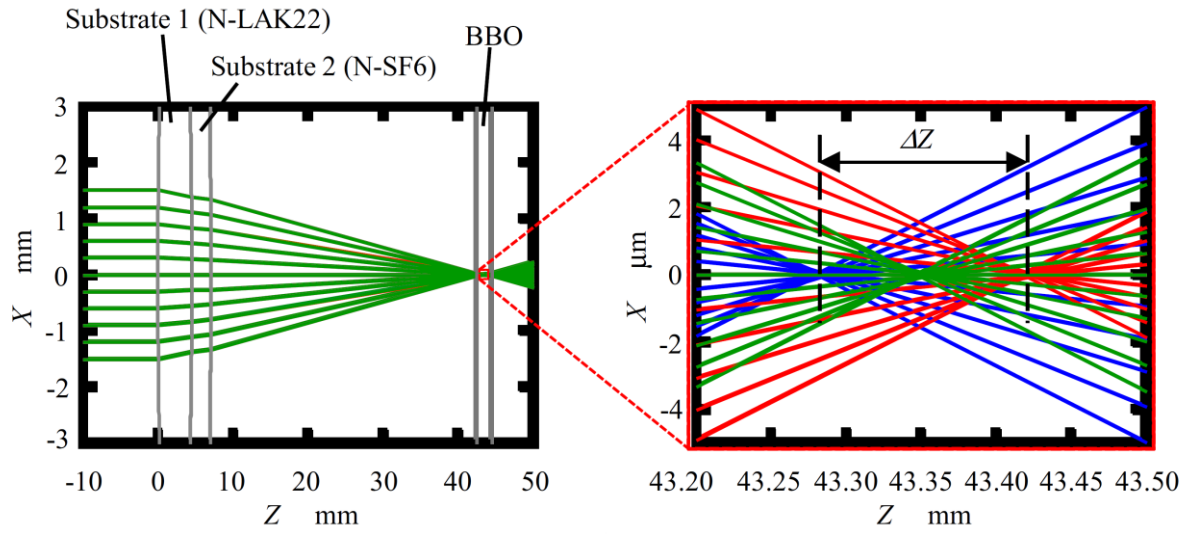

(a)

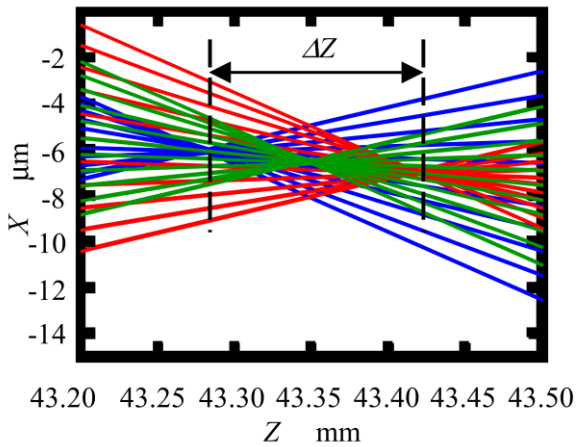

(b)

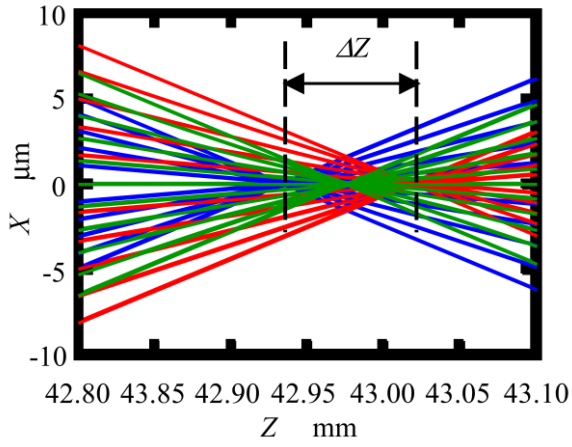

(c)

Figure 3.14 Results of ray tracing for the focal length of 40 mm of focusing lens; 1500 nm (blue lines), 1560 nm (green lines), and 1620 nm (red lines); (**a)** the case for $\Delta\theta = 0°$; (**b)** The case for $\Delta\theta = 1°$; (**c**) the case without the BBO crystal

Table 3.21 summarizes the ΔZ for the cases of focal lengths equals to 40, 75, and 150 mm. The difference between the sensitivities observed in the experiments and those predicted in theoretical calculation results can be explained by the influences of the chromatic aberration summarized in the table. In the experiments, second harmonic wave was effectively generated around the beam waist position of the light with a wavelength of 1560 nm (Z1560 nm), since the spectrum of second harmonic wave had its central peak around 780 nm. This was because the irradiance of the laser around Z1560 nm was larger than those in other areas due to the chromatic aberration, and the resultant SHG occurred effectively around Z1560 nm; in other words, the chromatic aberration made the effective crystal length L_{eff} shorter.

Table 3.21 The specifications of the lenses and the position of the BBO crystal

Focal length mm	**ΔZ without BBO crystal mm**	**Angle deg.**	**ΔZ with BBO crystal mm**
40	0.09	0	0.14
		1	0.14
75	0.16	0	0.26
		1	0.26
150	0.32	0	0.52
		1	0.52

The full width at half maximum of PD output voltage dependence on angular displacement in Figure 3.9 is summarized in Table 3.22. The FWHM for shorter focal length is found to be wider than that for longer focal length of the lens. The ratio of ΔZ to b is also summarized in the table. The ratio of ΔZ to b for shorter focal length is also found to be larger than that for longer focal length. Therefore, the effective crystal length L_{eff} is shorter for shorter focal length due to the stronger influence of the chromatic aberration. Thus, the resolution using the focal length of 75 mm is higher than that using the focal length of 40 mm. For shorter L_{eff}, the FWHM of the sinc quadratic function becomes wider. The FWHMs of sinc quadratic function calculated for various length of crystal L are plotted in Figure 3.15. The experimental results are

found to take closer value for the length of crystal of 0.25, 0.5, and 0.8 mm for the focal length of 40, 75, and 150 mm, respectively. These L_{eff} are several times longer than ΔZ; this result indicates that SHG is localized around Z1560 nm within L_{eff}. Therefore, the SHG spectra in Figure 3.8a are not similar to the fundamental wave spectra. Surface 4 of the BBO crystal makes the chromatic aberration ΔZ is 1.6 times longer than those without the BBO crystal as shown in Table 3.21.

Table 3.22 FWHM of second harmonic power dependence on angular displacement and $\Delta Z/b$

Focal length mm	**FWHM arc-second**	$\Delta Z/b$
40	6500	0.29
75	3900	0.15
150	2300	0.075

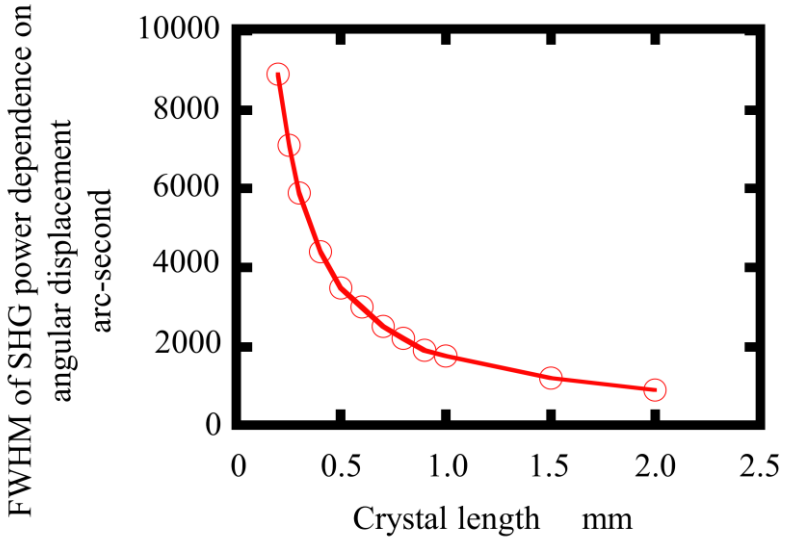

Figure 3.15 FWHM of SHG power dependence on angular displacement for various crystal length

3.6 Summary

A new optical angle measurement method has been proposed depends on the intensity of SHG. The proposed method is making use of the unique characteristic of high peak power and high-intensity electric field of the femtosecond laser pulses,

which can generate second harmonic waves based on the nonlinear optical phenomenon. Results of the theoretical analysis have clarified that BBO crystal is suitable for the proposed angle measurement method when a mode-locked femtosecond laser source having the spectrum ranging from 1500 to 1620 nm is employed. It has been demonstrated by theoretical analysis and experiment that a focused femtosecond laser beam is effective to realize SHG-based angle measurement for a femtosecond laser source with a small power where the intensity of a collimated beam from such a femtosecond laser source is too small to make SHG. Experimental results with the developed measurement system have demonstrated feasibility of the proposed angular measurement. Meanwhile, the sensitivity observed in the experiments has been found to be lower than that predicted in the theoretical calculation. To clarify the reason for the discrepancy between the results of theoretical calculation and those of the experiments, investigations have been carried out based on ray tracing. It has been clarified that the chromatic aberration has been one of the main roots causes of these problems, taking the results of ray tracing and observed second harmonic spectra into consideration. It has also been clarified that the shorter focal length of the focusing lens has made the influence of chromatic aberration stronger, and has made the effective crystal length L_{eff} shorter, resulting in the degradation of the sensitivity.

It should be noted that, as the first step of research, this study has been focused on the proposal of the angle measurement principle and on the verification of the feasibility of the proposed principle under the condition of a focused beam from a low power femtosecond laser source. Detailed investigation on the basic characteristics of the proposed method, design optimization of the optical setup for the achievement of higher resolution, as well as the measurement uncertainty analysis, will be carried out in future work. It should also be noted that the applications of angle measurement using a focused laser beam are limited and a high-power femtosecond laser source with a high-intensity collimated laser beam will also be employed in future work.

3.7 References

1. Yariv, A.; Yeh, P. *Photonics: optical electronics in modern communications*. Oxford University Press, Oxford, 2006.
2. Hecht, E. Optics. Pearson Education, London, 2006.
3. Franken, P.A.; Hill, A.E.; Peters, C.W.; Weinreich, G. Generation of optical harmonics. *Phys Rev Lett* **1961**, *7*, 118–119.
4. Koechner, W. *Solid-state laser engineering*. Springer, Berlin, 2006.
5. Dmitriev, V.G.; Gurzadyan, G.G.; Nikogosyan, D.N. *Handbook of nonlinear optical crystals*. Springer, Berlin, 1999.
6. Matsukuma, H.; Madokoro, S.; Astuti, W.D.; Shimizu, Y.; Gao, W. A new optical angle measurement method based on second harmonic generation with a mode-locked femtosecond laser. *Nanomanufacturing and Metrology* **2019**, *2*, 187–198.
7. https ://www.schot t.com/d/advan ced_optic s/f0321 76e-eab5-4116-bd38-09a9e f39e6 bb/1.4/schot t-optic al-glass -colle ction -datas heets-oct-2016-jap.pdf

Chapter 4
High-precision wavelength-dependent SHG angle detection

4.1 Introduction

This chapter proposes the feasibility study of high-precision SHG angle detection in the optical frequency domain. Unlike the intensity-dependent angle measurement in the previous section, the frequency-domain angle measurement is defined as the angle displacement detection indicated by the change in the character of each given frequency band over a range of frequencies. This method is proposed to overcome the drawbacks of the intensity-dependent SHG-based angle sensor in which the performance of the previous method is very dependent on the stability of the SHG intensity. The NLO crystal is not allowed to shift from the focal point during the measurement to avoid increasing measurement uncertainty. Moreover, chromatic aberration is present in the previous method that causes the localization of SHG.

It is known that frequency is inversely proportional to wavelength. Thus, the frequency-domain angle sensor can be shown in terms of wavelength band change

over the given wavelength range due to the angle change. Since the angle detection is based on SHG counts on the wavelength and its phase-matching condition, as previously mentioned in Chapter 2, the monochromatic laser consisting of narrow radiation width is unsuitable for this proposed angle sensor. Instead, the mode-locked Fs laser is proposed to be applied in the configuration setup. The mode-locked laser is characterized by two features, broadband in wavelength and high intensity, which is well-suited for the SHG angle sensor in the wavelength-dependent. Therefore, the mode-locked laser emitting femtosecond pulses are frequently used for measurements with high precision that provide absolute quantifying due to its information regarding the wavelength [1-5].

The SHG spectrum characteristic of the proposed method is firstly calculated by the plan-wave approximation equation to predict the measurement trend. The measurement trend designed in the theoretical calculation is realized experimentally by focusing the mode-locked Fs laser on a rotary stage mounted-NLO crystal that represents the measurement target. In this study, the configuration setup is changed from refractive optics to reflective optics parabolic mirror to avoid the chromatic aberration issue, which was a drawback of the focusing lens in the previous chapter. An NLO crystal with a large angle matching dispersion is required to accommodate the matching angle of the Fs wavelength range from 1480 nm to 1640 nm. Recalled the NLO matching angle characteristic in Chapter 2, the MgO: LiNbO3 crystal has a suitable range of matching angles of the given wavelength range. Further calculations related to the measurement trend by taking into account refraction at the interface between the NLO crystal and the air are also presented in this chapter.

4.2 The principle of wavelength-dependent angle sensor with focused beam

Angle detection in the wavelength domain needs laser input with a wide range of wavelengths, and the Fs laser is suitable for the requirement. As mentioned in Chapter 2, the angle detection based on SHG is related to the phase-matching condition that

occurs at a matching angle for its respective given wavelength. In using an Fs laser that consists of a wide range of wavelengths, when a specific wavelength component is at a matching angle, other wavelength components experience phase mismatching. The phase-matching of other wavelength components can thus be satisfied when the NLO crystal experiences angular displacement about its *Y*-axis. Figure 4.1 shows a schematic of the angle measurement based on the proposed method. By utilizing the SHG spectrum characteristic, angle measurement can be carried out by monitoring the evolution of the second harmonic spectrum over the angle change of the crystal. Unlike the angle sensor that depends on intensity where the dynamics of SHG are observed by using an oscilloscope-connected photodiode where the change in the output voltage of the photodiode indicates the angular displacement of the measurement target, the wavelength-dependent angle sensor uses a multimode fiber-connected to an optical spectrum analyzer (OSA) to display the spectrum within the desired range of wavelength.

Two methods are applied in terms of SHG peak determination, the centroid method and the spectral peak determination based on the highest intensity. The difference between peak determination methods will be discussed in the next section of this chapter. The spectral peak evolution based on both peak determination methods constructs the measurement trend. Thus, the sensitivity can be estimated. To realize the SHG-based angle measurement with wavelength-dependent, the characteristic of the NLO crystal that is acceptable for the angle setup is the crystal with a wide-angle of dispersion. According to the theoretical analysis in Chapter 2, MgO:$LiNbO_3$ crystal has a suitable phase-matching characteristic for this proposed angle sensor.

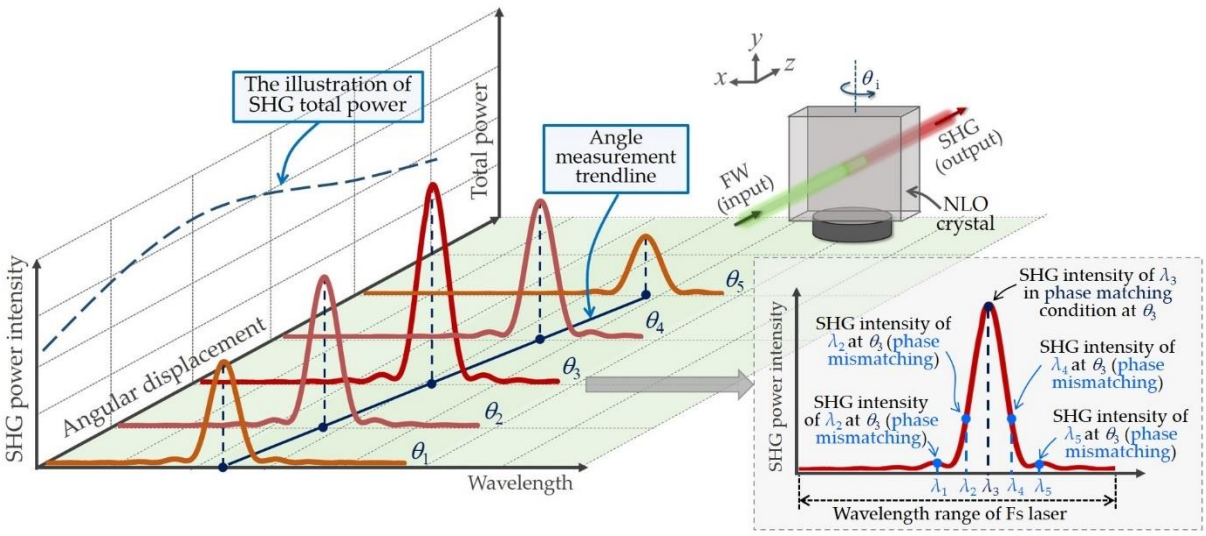

Figure 4.1 Schematic of the propose angle sensor principle based on SHG utilizing Fs laser.

4.3 Calculation design

Theoretical calculations are carried out to predict the measurement trend of the proposed angle sensor. As explained in Chapter 2, the SHG calculation must consider several parameters including the beam type to generate the second harmonic wave. In the use of the CW collimation beam, for example, calculations using the wave-plane approximation can be performed to describe the behavior of generating the second harmonic wave. The same thing can be done in the use of a collimated FS laser where each fundamental power associated with each wavelength contributes to the generation of SHG at its respective SHG wavelength [6]. Meanwhile, in the use of a focused beam, the wave-plane approximation calculation can also be exploited to predict the trend of the second harmonic wave as long as the Rayleigh length area is long enough compared to the length of the crystal NLO. If the Rayleigh length is much shorter than the crystal length, then the calculation using the plane wave approximation needs to be reviewed [7]. However, the plane wave approximation calculation is performed in this study as a preliminary analysis.

Through the plane wave approximation, let the fundamental power p_ω and SHG power $p_{2\omega}$ in Equation (2.14) be rewritten as p_i and p_{ij}', respectively, where the i-th index denotes the wavelength and the j-th index denotes angular position. As it is related to Equation (2.16) as well, the new equation can be written as follow [7-10]

$$p_{ij}' = \frac{2\pi^2 {d_{eff}}^2 L^2}{n_o(\lambda_i)^2 n_e(\theta, \lambda_i')\varepsilon_0 c {\lambda_i}^2 A} p_i^2 \ \mathrm{sinc}^2\left(|\Delta k(\theta)| L/2\right) \quad ; \begin{matrix} i = 1, 2, ..., m \\ j = 1, 2, ..., n \end{matrix} . \qquad (4.1)$$

Here, ε_0 is vacuum permittivity, c is the speed of light in a vacuum, L is the length of the crystal, and A is the cross-sectional area. These quantities are considered to be constant and be ignored to simplify the calculation since they remain the same despite the changes of other physical quantities. Meanwhile d_{eff} is the effective nonlinear coefficient that depends on the crystallographic point group and the propagation direction. Since MgO: $LiNbO_3$ is employed in this study, the d_{eff} is determine by Equation (2.20) in Chapter 2. The azimuthal position between the X-axis and the projection of the wave vector in the surface of the crystal ϕ in the equation is related to crystal orientation. It does not influence phase matching for the case of a uniaxial crystal-like MgO: $LiNbO_3$ [11]. Therefore, it is assumed in this calculation that ϕ is equal to 0, thus Equation (2.20) can be rewritten as follows

$$d_{eff} = d_{22} \cos^2 \theta , \qquad (4.2)$$

where d_{22} is the nonlinear coefficient to 2.1 pm/V for MgO: $LiNbO_3$ crystal, θ is the angle between the optical axis and the propagation direction (wave vector) which can be determined over the angle change of the crystal that rotates about its Y-axis. This angle is strictly determined by the phase matching condition. According to Equation (4.1), d_{eff} is contributing to the magnification of the SHG power only. It means that the characteristic of the angle measurement is not affectionated by the d_{eff} and can be neglected in the calculation. It should be noted that restricting factors such as heat effect, walk-off effect, and dispersive spreading are not taken into consideration in the calculation [7]. The FW power intensity p_i can be determined in the experiments where every mode in the fundamental wave has its deterministic power intensity. Furthermore, it should be noted that p_{ij}' is proportional to the quadratic of FW power (p_i^2) and the quadratic of sinc function. This sinc function describes the behavior of the laser propagation inside the crystal. By taking the birefringent effect and phase

mismatching Δk into consideration, it can be expressed as follows:

$$\operatorname{sinc}^2\left(|\Delta k(\theta)|L/2\right)=\frac{\sin^2\left(|\Delta k(\theta)|L/2\right)}{\left(|\Delta k(\theta)|L/2\right)^2}. \tag{4.3}$$

Where the Δk can be determined using Equation (2.21) correlates with Equation (2.18) in Chapter 2. Let the fundamental wavelength λ_{ω} and SHG wavelength $\lambda_{2\omega}$ be rewritten as λ and λ', respectively, so that the equations can be written as

$$\Delta k(\theta)=\frac{4\pi}{\lambda}\left[\, n_{\mathrm{o}}(\lambda)-n_{\mathrm{e}}\left(\theta,\lambda'\right)\right]. \tag{4.4}$$

$$n_{\mathrm{e}}\left(\theta,\lambda'\right)=\left\{\left[\frac{\cos\theta}{n_{\mathrm{o}}\left(\lambda'\right)}\right]^2+\left[\frac{\sin\theta}{N_{\mathrm{e}}\left(\lambda'\right)}\right]^2\right\}^{-1/2}. \tag{4.5}$$

The matching angle of MgO: $LiNbO_3$ that has been shown by Figure 2.2 in Chapter 2, is satisfied when $\Delta k\ (\theta_{\mathrm{pm}}) = 0$ and $n_{\mathrm{o}}(\lambda) = n_{\mathrm{e}}\ (\theta_{\mathrm{pm}},\lambda')$. After all the calculations are fulfilled, the matrix p_2 can be built as follows:

$$p_2=\begin{pmatrix} p_{11}' & p_{12}' & \cdots & p_{1\mathrm{n}}' \\ p_{21}' & p_{22}' & \cdots & p_{2\mathrm{n}}' \\ \vdots & \vdots & \ddots & \vdots \\ p_{\mathrm{m}1}' & p_{\mathrm{m}2}' & \cdots & p_{\mathrm{mn}}' \end{pmatrix}. \tag{4.6}$$

The matrix rows represent the calculated second-harmonic power intensity related to angular displacement. Meanwhile, the matrix column represents the second harmonic power intensity associated with the wide range of Fs laser wavelength. The calculated angle measurement trend can be decided by the peak of the calculated spectrum of the second harmonic wave concerning the angular displacement. Finally, the sensitivity can be determined by the slope of the calculated peaks trend line of the second harmonic wave.

4.4 Experiment design and procedures

In this section, the experimental setup and procedures are explained in detail. It is known that SHG can only be generated by sufficient FW power. However, the direct use of the Fs laser output is insufficient to generate a proper harmonic wave that OSA can observe. As the practical solution, beam intensifying is needed to gain higher power density, that is, by reducing the beamwidth. The beam intensifying procedure has already been proposed in Chapter 3 by employing the lens. However, chromatic aberration is becoming an issue that cannot be avoided with the use of the lens. Therefore, the new beam intensifying setup is introduced by changing the refractive properties of the lens to the reflective properties of the parabolic mirror.

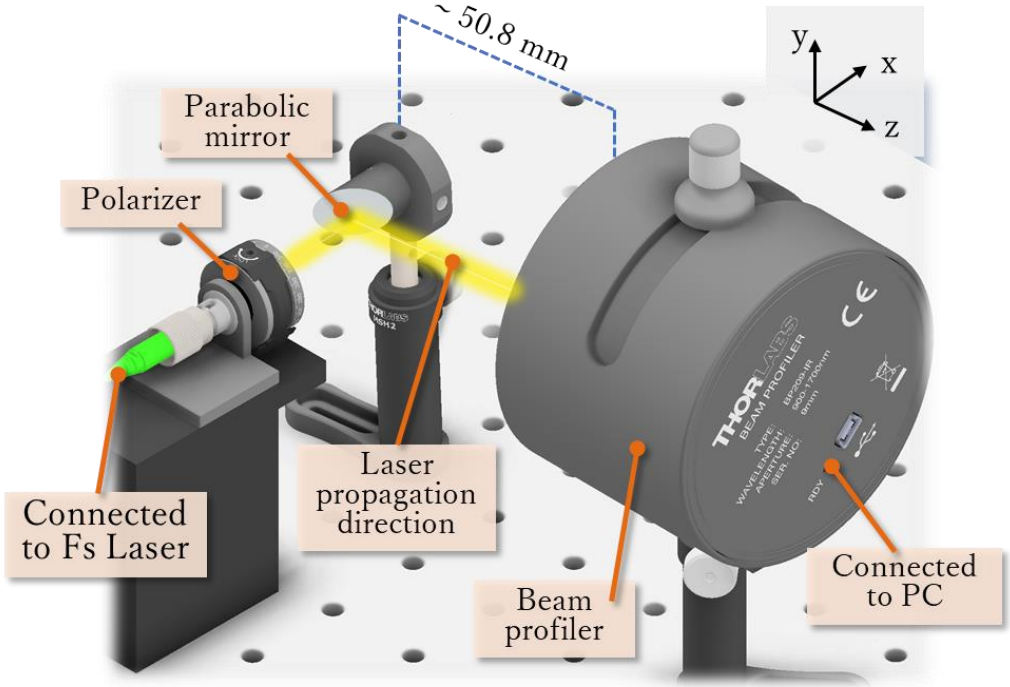

Figure 4.2 Schematic of experimental setup of focused beam observation.

The experiment of the proposed angle detection in the optical wavelength domain is firstly started by the alignment procedure with a commercial mode-locked femtosecond laser employed as the FW laser source. The laser is synchronized by an Rb frequency standard and a frequency synchronizer. The beam emitted from the fiber-connected Fs laser propagated through the optical devices, i.e., a collimating lens

to avoid the beam spreading as the laser propagates, a polarizer to polarize the laser beam, and an off-axis parabolic mirror to focus the beam. Afterwards, to confirm the beamwidth reduction due to the beam focusing procedure, the beam in the focal point of the off-axis parabolic mirror is observed by using the beam profiles-connected to PC as the experimental setup is schematically shown in Figure 4.2.

The alignment for the angle measurement is the next step to be done. Once the focused beam has been confirmed, a rotary stage-mounted MgO:$LiNbO_3$ crystal representing the measurement target is placed in the focal point of the parabolic mirror. Afterwards, the beam consists of FW and generated SHW eventually reaches an objective lens and multimode fiber connected to an optical spectrum analyzer in which both spectra are recorded. The stepping motor controller drives the rotary stage to ensure the angular shift of the target is restrained. The alignment stage is equipped with an objective lens that can be moved independently in the XYZ axis to guide the beam to the multimode fiber. The schematic setup and the photograph of the experimental setup in this study can be seen in Figure 4.3(a) and Figure 4.3(b), respectively. The specification of the off-axis parabolic mirror, multimode fiber, the optical spectrum analyzer, MgO:$LiNbO_3$ crystal, fiber alignment stage, and beam profiler can be seen in Table 4.1 to Table 4.5.

Table 4.1 The specification of the beam profiler.

Components	**Value**
Manufacturer	Thorlabs Japan Inc.
Model number	BP209-IR
Wavelength range	900–1700 nm
Measurable beam diameter	2.5 μm-9 mm
Dynamic range	78 dB

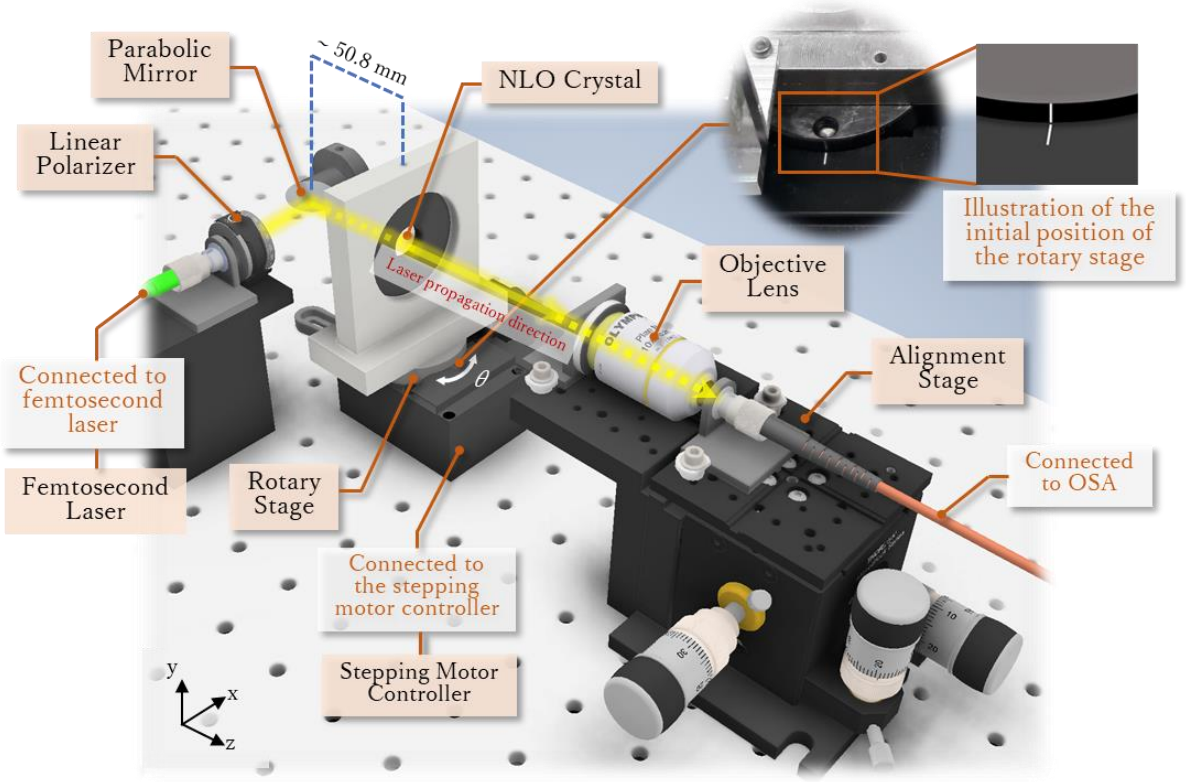

(a)

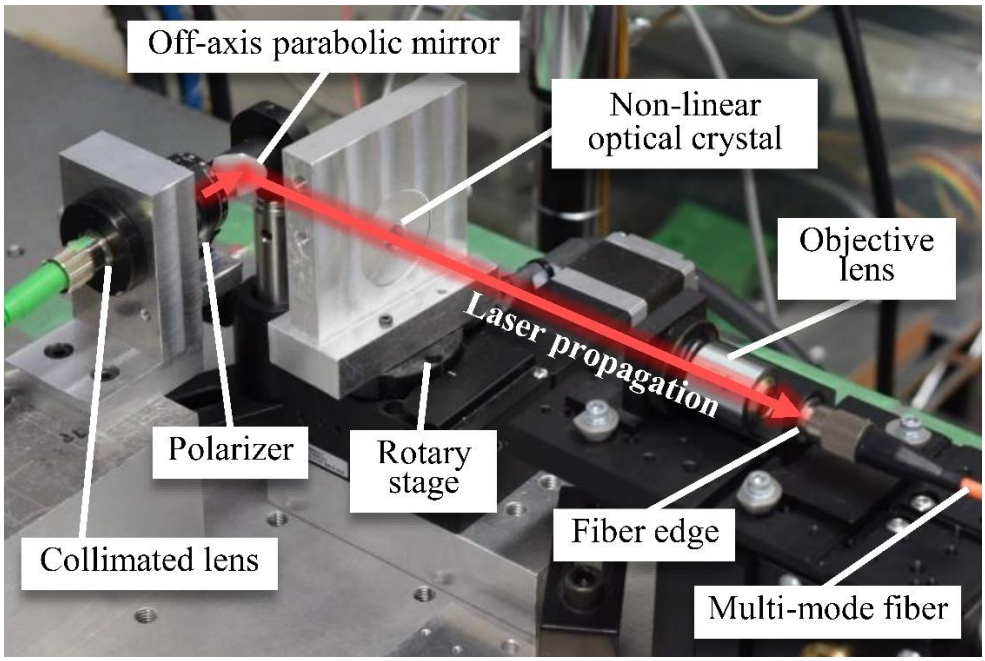

(b)

Figure 4.3 Experimental setup of wavelength-dependent angle sensor with focused beam femtosecond laser (a) A schematic of proposed angle sensor; (b) A photograph of the experimental setup [12].

Table 4.2 Specification of the optical spectrum analyzer.

Components	Value
Manufacturer	Yokogawa Electric Co.
Model number	AQ6370C-20
Wavelength range	600–1700 nm
Wavelength accuracy	±0.01 nm (Range: 1520–1580 nm)
Wavelength resolution	0.02 nm
Wavelength repeatability	±0.005 nm
Intensity sensitivity	−90 dBm [i.e. 1 pW] (1300–1620 nm)
Intensity accuracy	±0.4 dB (when input intensity is –20 dBm)
Intensity dispersion	±0.1 dB

Table 4.3 Specification of the off-axis parabolic mirror.

Components	Value
Manufacturer	Thorlabs Japan Inc.
Model number	MPD029-G01
Reflected Focal Length	>1000:1 at 1050-1700 nm
Off-Axis Angle	90°

Table 4.4 Specification of MgO:$LiNbO_3$ crystal

Components	Value
Manufacturer	CASTECH Inc.
Name	5%MgO:LN
Diameter	5(±0.1) mm × 5(±0.1) mm
Thickness	2(±0.1) mm
Angle Tolerance	θ=47°±0.5° ϕ=30°±0.5°
Flatness	≤λ/6 at 633 nm
Coating	S1, S2 : AR (1500–1600 nm/750–800 nm)

Table 4.5 Specification of the multi-mode fiber.

Components	Value
Manufacturer	Thorlabs Japan Inc.
Model number	M42L02
Type	FC/PC to FC/PC
Wavelength range	400–2400 nm
Core diameter	50 mm ± 2%

The pulse-to-angle conversion was evaluated using an autocollimator as the experimental setup is shown schematically in Figure 4.4. The angular shift of the rotary stage due to pulses given at certain intervals is observed by the autocollimator as an external angle sensor in the clockwise and counterclockwise rotation directions. The clockwise rotational movement corresponds to the forward measurement result. While the counterclockwise movement is indicated by the inverse measurement results. In the first step, the angular movement is carried out on the angle range of the autocollimator because the autocollimator has a limited angle range which is lower than the proposed angle sensor range.

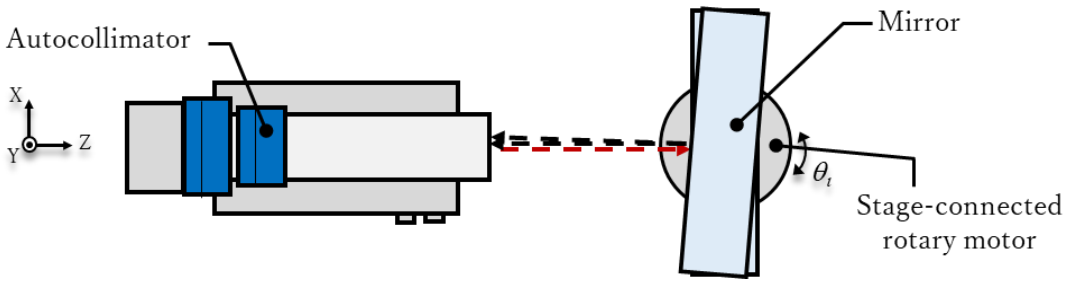

Figure 4.4 The schematic of experimental setup to confirm the angle shift of the rotary stage due to the given interval pulse.

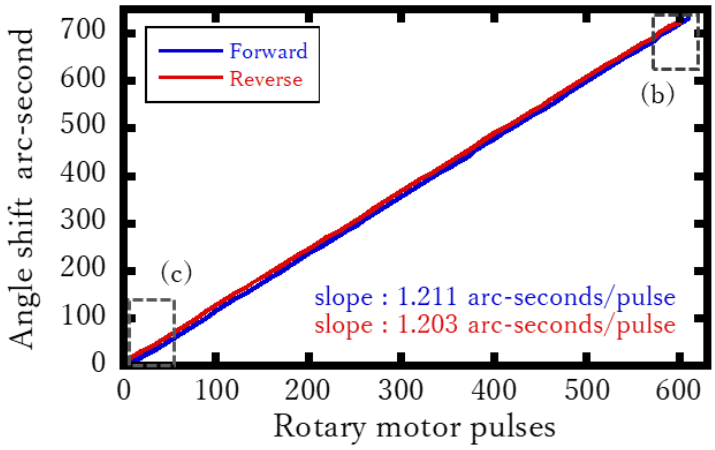

(a)

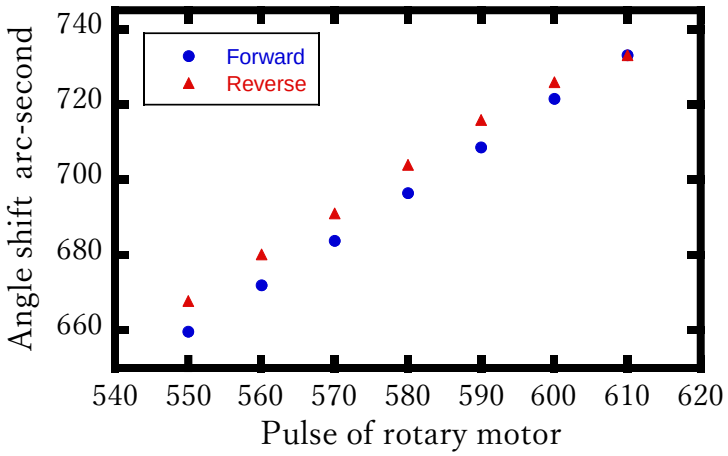

(b)

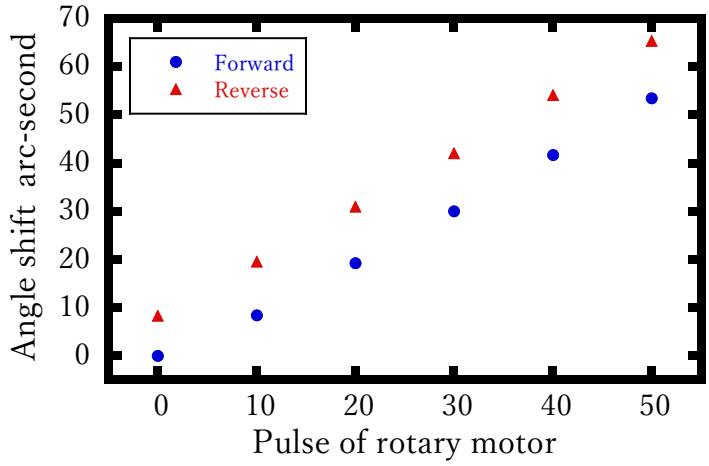

(c)

Figure 4.5 (a) Angle shift observation over the interval of 10 pulses; (b) Augmented area of angle shift observation near the maximum pulses given to the rotary stage; (c) Augmented area near the initial position or rotary stage.

Figure 4.5 exhibits the experimental results. The comparison between the forward and reverse measurements can be seen in Figure 4.5a by the blue and red lines, respectively. Even though they have a similar tendency, if the edge of the measurement is enlarged, it is seen that the two lines do not coincide. There is a discrepancy between the two lines, as shown in Figures 4.5b and 4.5c. It indicates that the rotary stage is not returning to the initial position even after the same pulse is applied. As a consequence, the different conversion values are obtained, where the forward movement has a conversion value of 1.211 arc-second/pulse and the reverse movement has a conversion value of 1.203 arc-second/pulse. In this study, the forward or the clockwise movement will be applied in the rotary stage during the experiment.

The stability of the given pulse can be seen in Figure 4.6. As can be seen in the figure, even though the constant pulse is given to the rotary stage, the angular movement is not constant. However, both directions of movement of the rotary stage have stability with the same tendency every ten times of data.

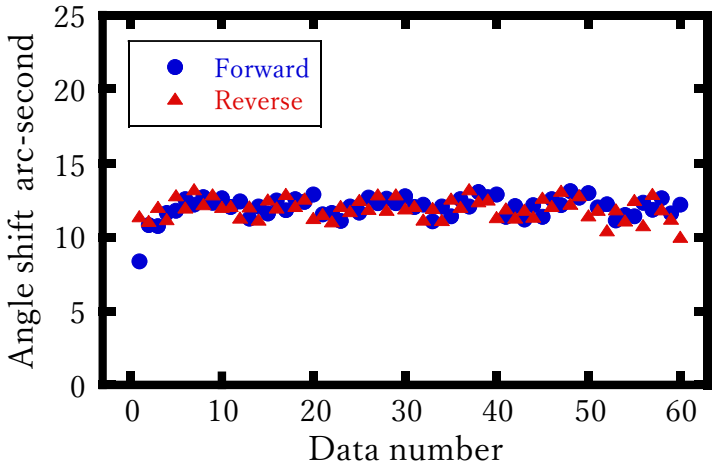

Figure 4.6 The pulse interval stability

4.5 Result and discussion

4.5.1 Beam spot evaluation

Figure 4.6 exhibits the beam spot evaluation that shows the Gaussian-like distribution of the intensity. The beam width can be defined as the $1/e^2$ value of those

Gaussian-like intensities. By using Equation (2.24) in Chapter 2, the beamwidth of the laser in the focal spot can be estimated. As the focus distance of the parabolic mirror is 50.8 mm, the diameter of the diameter collimated beam is 3.6 mm, and the central wavelength of 1560 nm, the diameter of the focussed beam is expected to be 28 μm. However, the experimental observation using the beam profiler shows a slightly wider beamwidth where the beamwidth in *X*-position is 37.2 μm and *Y*-position is 42.5 μm, as can be seen in Figure 4.7, indicating that the laser beam is not perfectly round. The measurement result was larger than the calculation in both axes. One of the reasons can be due to imperfect alignment. There is a possibility that aberration such as comma aberration has been generated, which is inferred from the two factors; alignment of the *X*-position is more difficult than that of the *Y*-position, and the diameter of the *Y*-position is larger than that of the *X*-position.

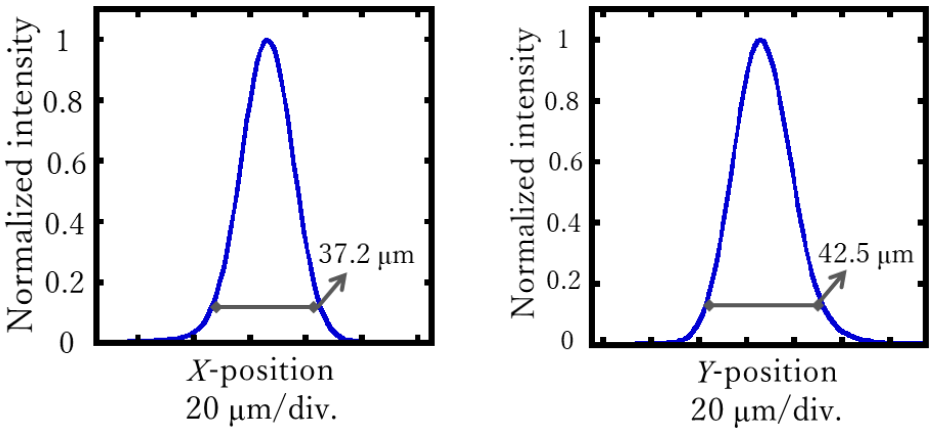

(a) (b)

Figure 4.7 Result of beam spot observation; (a) Cross-sectional profiles of *X*-axis; (b) Cross-sectional profiles of *Y*-axis.

4.5.2 Calculation result of SHG-based angle measurement

The characteristics of $n_e(\theta,\lambda`)$ and the characteristics of the sinc quadratic function significantly influence the SHG characteristic according to Equation (4.1). These parameters dynamically change over a variety of wavelengths and angles. Figures 4.8a and 4.8b present the dynamics of the sinc quadratic function of MgO:$LiNbO_3$ crystal according to Equation 4.3 in the 3D plot and 2D plot, respectively. It can be seen that

the spectral width of the sinc quadratic function spectrum is getting narrower as a larger angular shift is applied to the crystal. Meanwhile, Figure 4.9 shows the calculation result according to Equation 4.5, which reveals the dynamics of the $n_e(\theta, \lambda`)$.

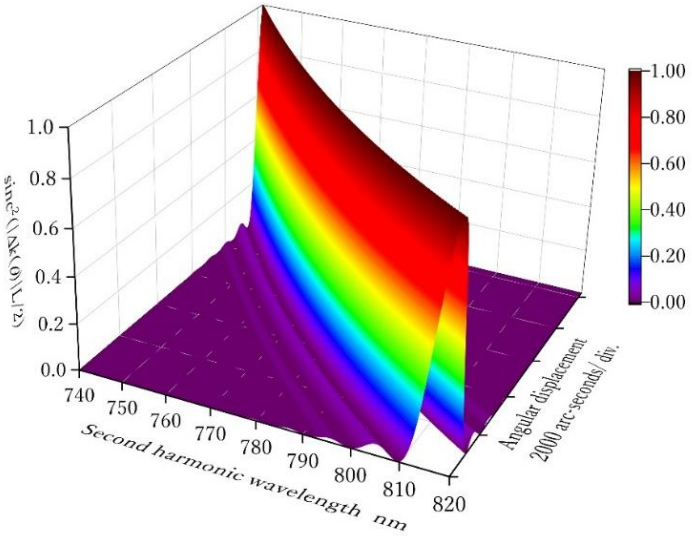

(a)

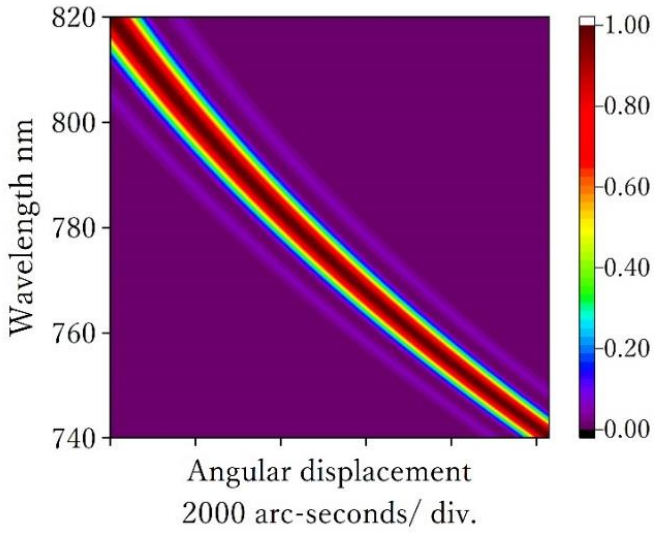

(b)

Figure 4.8 The dynamics of sinc quadratic function over the change of angle for given fundamental wavelength ranges from 1480 nm to 1640 nm; (a) The 3D plot; (b) The 2D plot.

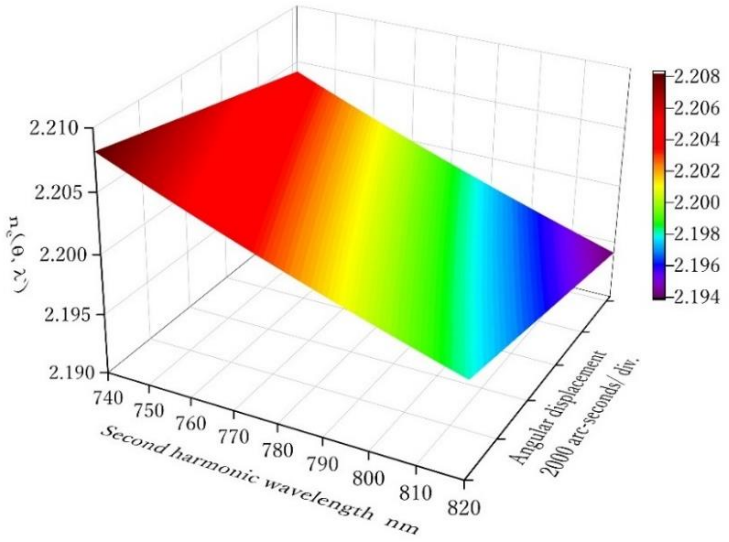

Figure 4.9 The characteristics of $n_e(\theta, \lambda`)$ with respect to the SHG wavelength and angular displacement around the phase-matching angle of MgO:$LiNbO_3$ crystal

The FW power intensity for the calculation is extracted by the observed FW spectrum of Fs laser as shown in Figure 4.10, where each mode of wavelength has a respective power intensity. The spectrum is not smooth because it consists of peaks and valleys in which three high peaks are spotted, where the significant drop in intensity has occurred at wavelengths of 1522.8 nm and 1535.6 nm. The OSA sensitivity is set to the "NORMAL" setting during data recording with 500 sampling data within the wavelength range from 1480 nm to 1640 nm.

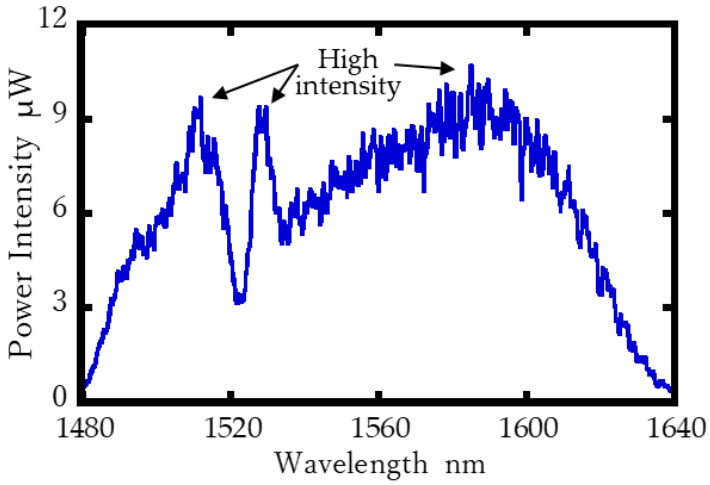

Figure 4.10 The fundamental wave spectrum characteristic of the Fs laser

The calculation result to predict the SHG spectrum characteristic using Equation (4.1) with the matrix model of Equation (4.6) is shown in Figure 4.11 as 2D and 3D

plotted graph. The contour characteristic of the calculation in Figure 4.11a shows the emergence of localized SHG intensity in three areas. It can state that the localized SHG intensity is caused by the characteristic of the FW spectrum in Figure 4.10, where it also has three significant intensity areas. As shown in Figure 4.11b, a drop in SHG power also appears, resulting in the appearance of separate peaks (split peaks) at a certain angular position of the crystal.

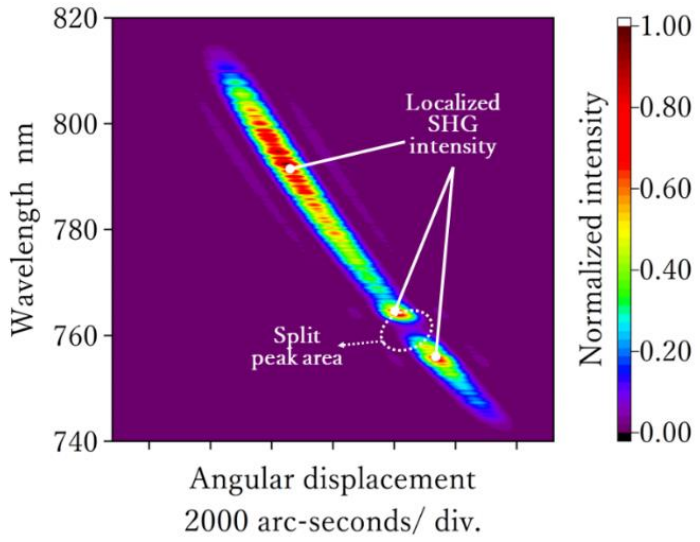

(a)

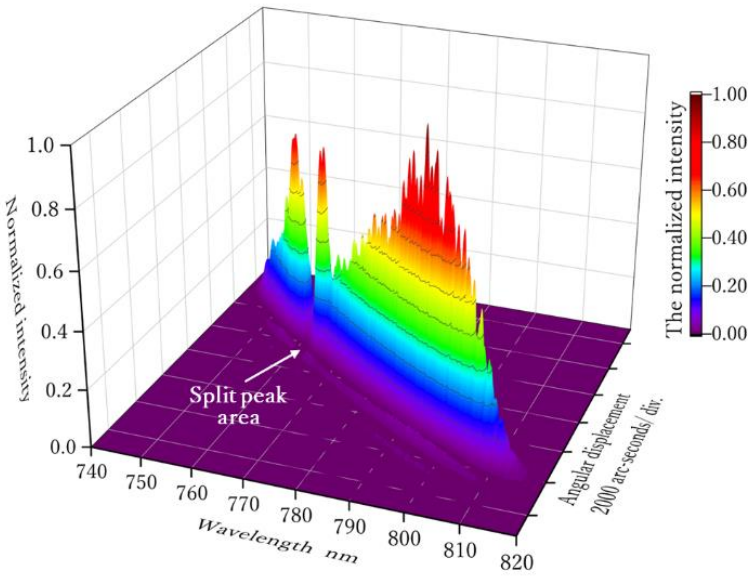

(b)

Figure 4.11 The SHG spectra characteristic based on the calculation result; (a) The 2D plot; (b) The 3D plot.

The measurement trend based on the calculation result in Figure 4.10 is evaluated by observing the peak shift of the SHG spectra with respect to the angular position of the crystal around its phase-matching angle. Two methods are introduced in order to determine the peak position. The first method is the centroid method, where the peak of spectra is indicated by the central value of the spectra that is evaluated using the following formula [13].

$$\lambda_C = \frac{\sum_i \lambda_i I(\lambda_i)}{\sum_i I(\lambda_i)} \tag{4.7}$$

where λ_i is the i-th sampling wavelength and $I(\lambda_i)$ is the optical intensity at λ_i. To minimalize the noise influence, the cutoff power intensity is given and set to half of the maximum intensity so that the following condition can be realized

$$I(\lambda_i) = \begin{cases} 0 & \text{if } I(\lambda_i) < 0.5 \max\{I(\lambda_i)\} \\ I(\lambda_i) & \text{if } I(\lambda_i) \geq 0.5 \max\{I(\lambda_i)\} \end{cases} \tag{4.8}$$

The second method is the highest intensity method that directly determines the spectral peak, where the highest intensity of the SHG spectrum for the respective angular position indicates the peak of the spectra. Unlike the centroid method, no cut-off power is applied to the calculation procedure.

Figure 4.12 displays the measurement trendline of the calculated SHG spectra based on the centroid and the highest intensity methods. In general, no significant difference inside the measurement sensitivity area or the area in which the trendline is linear. However, this method gives significantly different results in the split peak area, as shown in the figure, wherein the centroid method allows continuous measurement trends in the split peak area. In contract, the highest intensity method shows the real spectral peaks without additional data processing. It reveals that the sensitivity of the theoretical calculation is 0.00724 nm/arc-second using the centroid method and 0.00713 nm/arc-second using the highest intensity method.

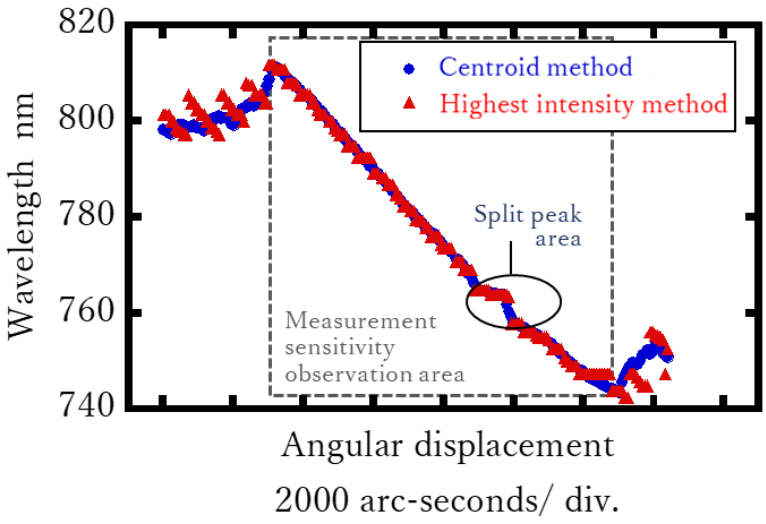

Figure 4.12 The measurement trendlines based on the centroid method (blue dots) and the highest intensity method (red triangles)

4.5.3 Experimental result and evaluation on the angle measurement

Experiments were carried out to confirm the feasibility of the proposed angle sensor. The use of a parabolic mirror in the proposed angle sensor has been shown to reduce the chromatic aberration that occurs when the beam is focused using a lens, as described in Chapter 3. In Chapter 3, the BBO crystal was employed as a nonlinear optical crystal because the angular dispersion of BBO to the phase mismatch is rather small. As the preliminary observation result to confirm the advantage of the parabolic mirror in beam focusing, Figure 4.13 shows a comparison of the SHG spectra obtained with a parabolic mirror and a lens, as depicted in Figures 4.13a and 4.13b, respectively. As can be seen in Figures 4.13a and 4.13b, the spectral trends of the two results are quite different. In the case where a parabolic mirror focused the laser, the second harmonic wave spectrum has a shape that reflects the shape of the FW spectrum in Figure 4.10. The spectrum is broader than the spectrum obtained when the lens was used to focus the light. On the other hand, the second harmonic wave spectrum with the lens focusing has a Gaussian-like shape. This is because when the light is focused by a parabolic mirror, the localization of the second harmonic wave due to chromatic aberration shown in Chapter 3 does not occur. As discussed in Chapter 3, the conversion efficiency from the FW to second harmonic wave at the wavelength apart

from the central wavelength decreases due to less intensity at the focusing point of the wavelength due to chromatic aberration. Therefore, by using a parabolic mirror, it is expected that a wide measurable range can be achieved by eliminating the effect of chromatic aberration.

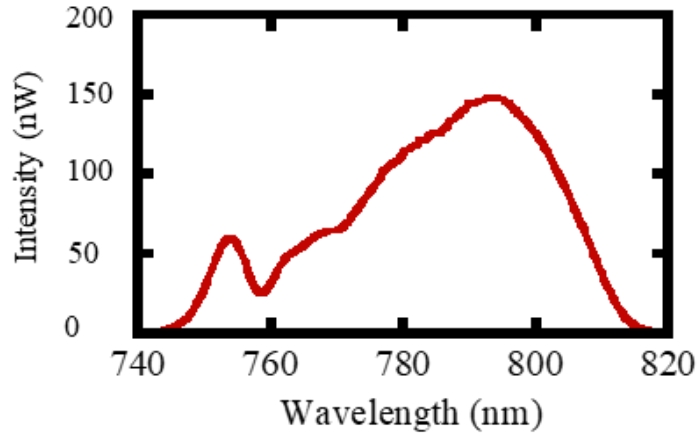

(a)

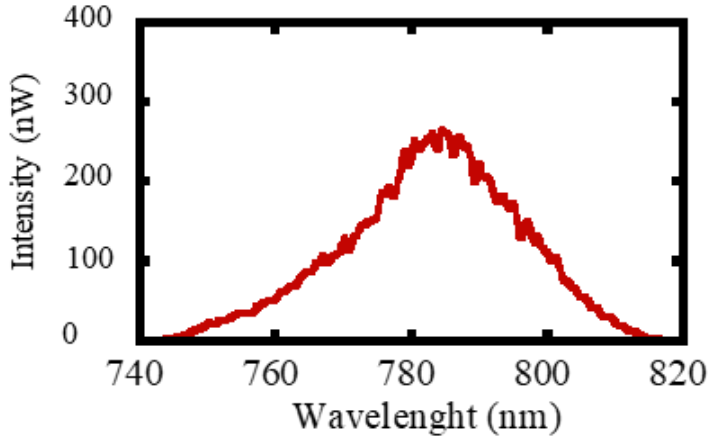

(b)

Figure 4.13 (a) Observed second harmonic wave spectrum using parabolic mirror, (b) Observed second harmonic spectrum using lens.

A feasibility study of the proposed angular measurement method based on second harmonic generation in the optical wavelength-dependent was carried out. The MgO:$LiNbO_3$ crystal was employed as a nonlinear optical crystal in the experiment. Data were taken with pulse intervals of 150 for 120 data on the angular position of the crystal. Figure 4.14 shows the experiment result as the 2D and 3D graphs of SHG spectra observation over the change in angular position. The localized SHG intensities

are spotted as it has predicted by the theoretical calculation in the previous section as well as the split peak that also appears in a similar position as the calculation result. The spectral evolution near the split pea area is shown in Figure 4.15. Two peaks appear within a certain range of angular positions of the crystal.

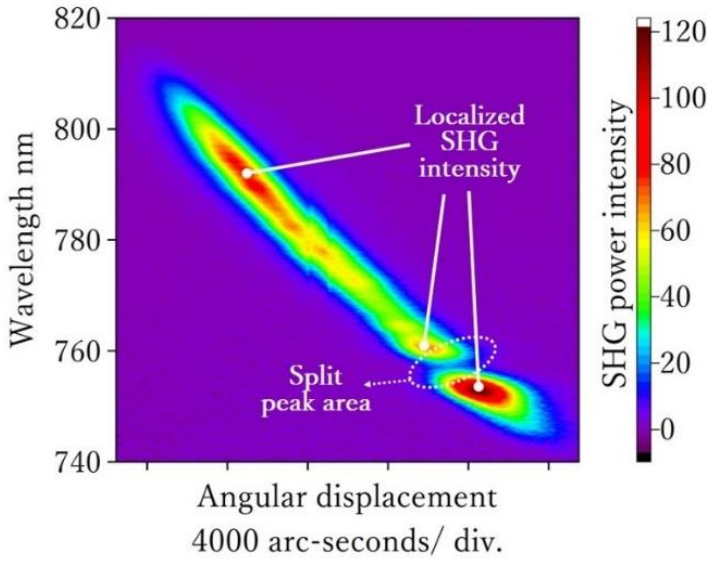

(a)

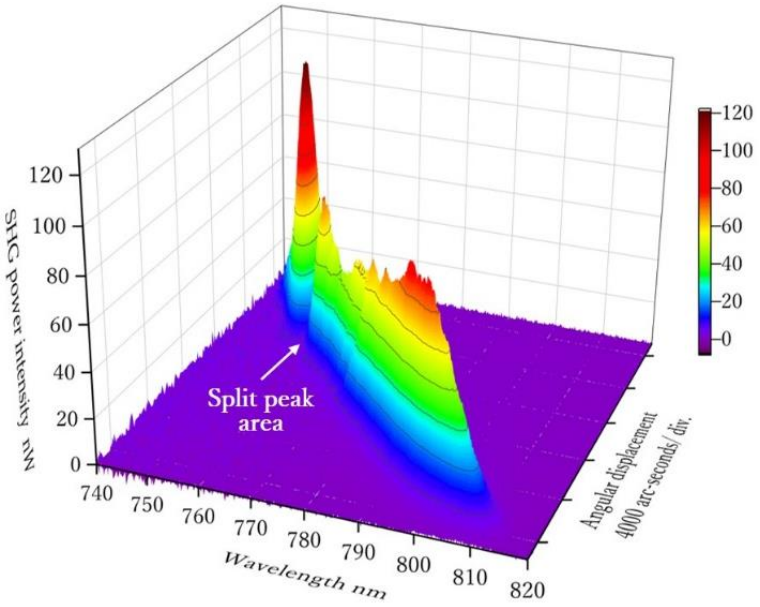

(b)

Figure 4.14 The observed SHG spectra characteristic over the change in angular position of MgO:$LiNbO_3$ crystal; (a) The 2D plot; (b) The 3D plot.

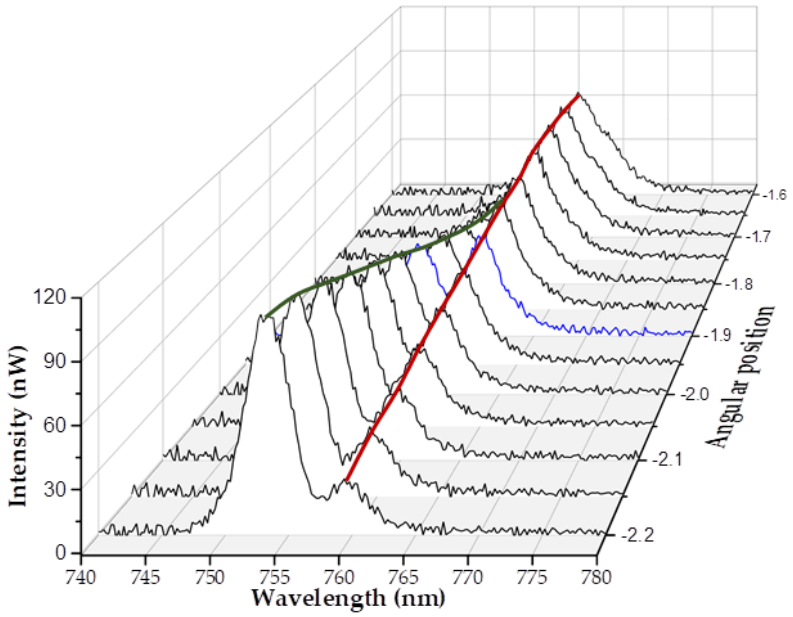

Figure 4.15 The spectral evolution in the split peak area

The measurement trend is indicated by the spectral peak of the observed SHG in Figure 4.14. As explained in the previous section, the spectral peak can be determined by the centroid method (Ic method) and the highest intensity method (Ipeak method). Compared to the centroid method, the highest intensity method is easier to realize experimentally since the spectrum's peak can be observed using the OSA directly. On the other hand, the centroid method reduces noise influence. To confirm it, the spectral peak determination without cut-off of the intensity (Ic non-threshold) is also performed in the centroid method.

Firstly, the measurement trend line by the Ic non-threshold is evaluated as shown in Figure 4.16. The whole analysis in Figure 4.16a shows the nonlinear spectral peak on the edge of the measurement trendline; therefore, to determine the measurement sensitivity, the trendline is cut in the range of the linear part only, as shown in Figure 4.16b. The measurement sensitivity according to Figure 4.16b is 0.00299 nm/arc-second. On the other hand, Figure 4.17 shows the angle measurement trendline by the centroid method with the cut-off power intensity. The noise effect, especially at the edge of the measurement trendline in which the SHG conversion is relatively low, can be reduced. As a result, the measurable angle can be expanded. This analysis achieves the

measurement sensitivity of 0.00311 nm/arc-second. Lastly, Figure 4.18 exhibits the angle measurement trendline by the highest intensity method. The measurement trendline is not as smooth as the result analyzed by the centroid method, but it has a similar measurement tendency. Unlike the analysis result using other methods, the result by this method shows two different sensitivity areas as the consequence of the split peak emergence. Those are 0.00347 nm/arc-second in the most extended angle range and 0.00092 nm/arc-second in the least angle range.

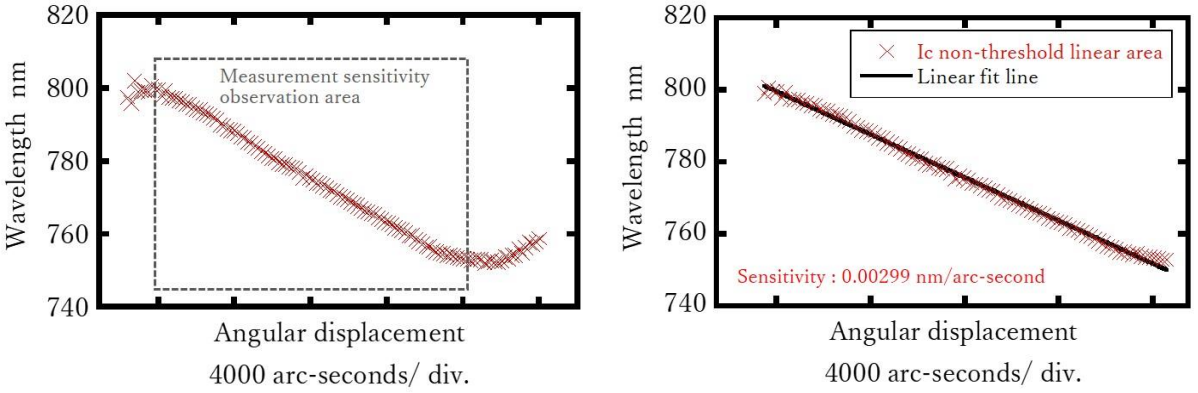

Figure 4.16 Angle measurement trendline using centroid method without cut-off power intensity; (a) the entire spectral peak analysis; (b) the spectral peak in the linear area.

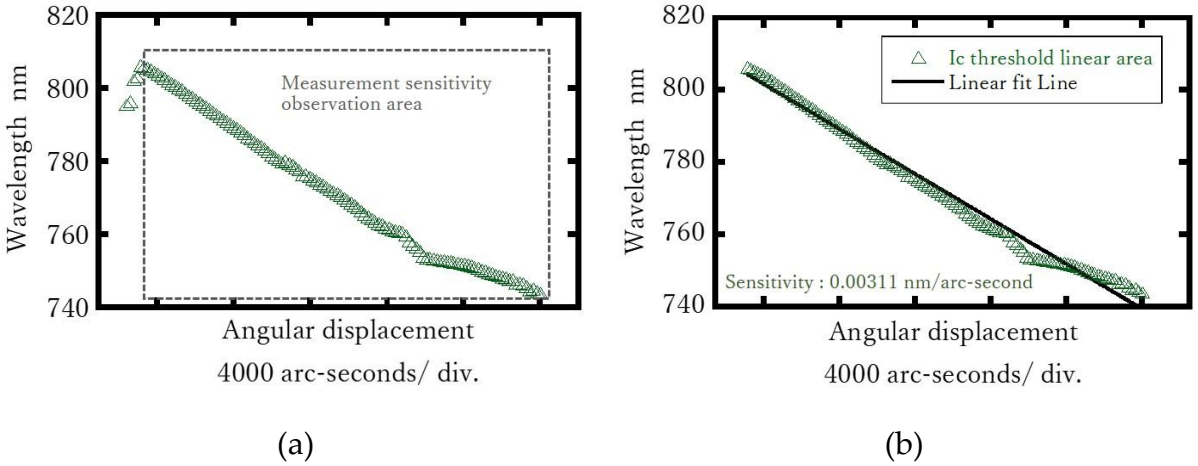

Figure 4.17 Angle measurement trendline using centroid method with cut-off power intensity; (a) the entire spectral peak analysis; (b) the spectral peak in the linear area.

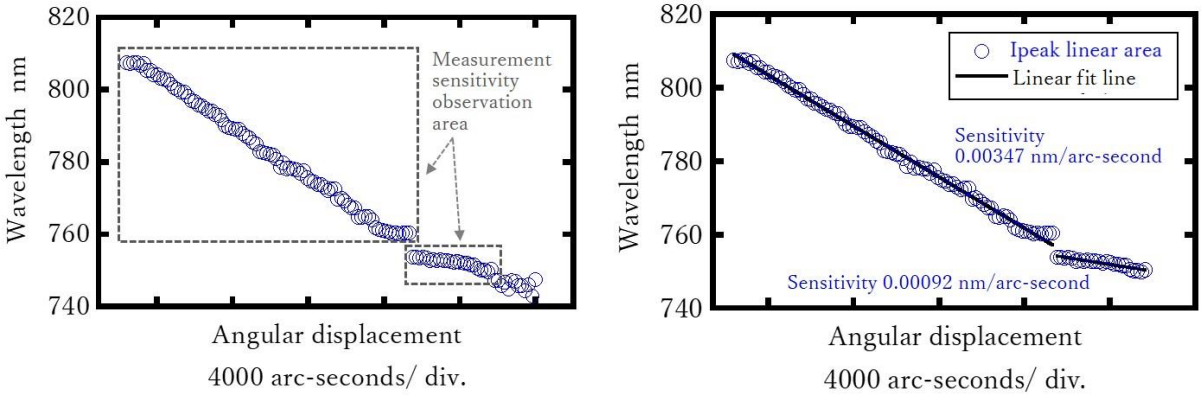

(a) (b)

Figure 4.18 Angle measurement trendline using the highest intensity method; (a) the entire spectral peak analysis; (b) the spectral peak in the linear area.

Figure 4.19 compares the trend line angle measurements using all analytical methods. Each method works differently in the split peak area where continuous points are obtained using the centroid method; meanwhile, the discrepancy appears in using the highest intensity method. Figure 4.20 provides a better understanding of how different analytical methods give different results in determining spectrum peaks, especially in the double peak area. It is known that the resolution of the OSA is 0.02 nm; therefore, the angular resolution of the experiment result is equal to measurement sensitivity divided by the wavelength resolution of the OSA. The experiment result of the proposed angle sensor analyzed by some spectral peak methods is summed up in Table 4.6. The measurement sensitivity is less than the calculated measurement sensitivity in the previous section. However, the measurable angle is wider compared to the calculation result. The difference between the calculation and experiment result will be discussed in the next section.

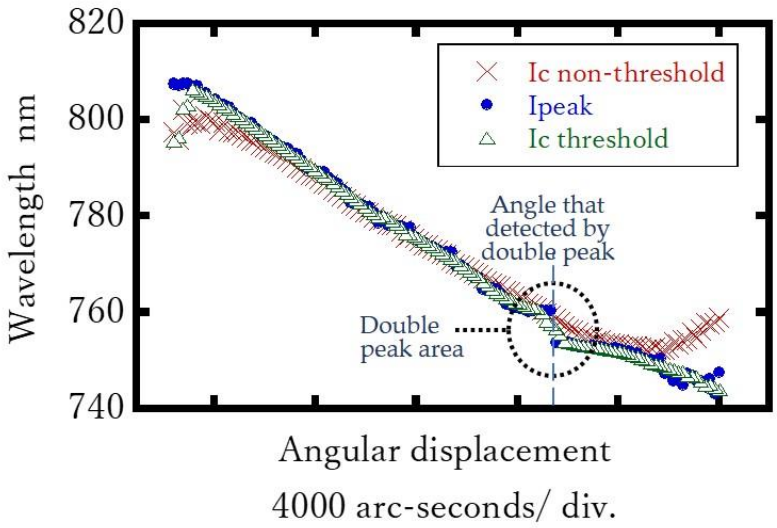

Figure 4.19 The comparison angle measurement trendline using several peak analysis methods

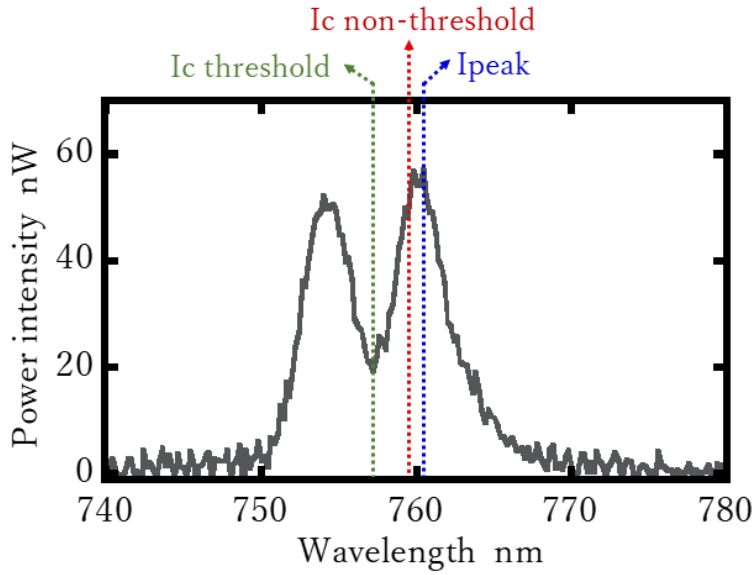

Figure 4.20 The spectral peak determination using different method in the split peak area.

Table 4.6 Angle measurement result in several methods

Method	Wavelength range nm	Angle range arc-second	Sensitivity nm/arc-second	Resolution arc-second
Ic non-threshold	752.88 – 800.76	17100	0.00299	6.69
Ic threshold	744.02 – 806.32	20880	0.00311	6.43
Ipeak	760.40 – 807.40	14940	0.00347	5.67
	750.40 – 753.80	4140	0.00092	21.74

Further analysis using the centroid method, the measurement resolution that was

previously limited by the wavelength resolution of the optical spectrum analyzer is possible to be overcome by this method. The measurement resolution can be expressed by the following equation

$$\Delta\theta = \frac{N}{S}. \tag{4.9}$$

Where $\Delta\theta$ denotes the angular resolution, N denotes the noise level, and S is the sensitivity coefficient. In this study, N is twice as large as the standard deviation of the centroid wavelength at a specific angular position, and S is the angle detection sensitivity obtained in the experiment. In order to obtain the resolution of the proposed method using the centroid method, the noise level from experiments was evaluated by taking ten spectral measurement data with a fixed rotary stage as a result shown in Figure 4.21. In addition, the dynamic range of the measurement method was also evaluated as a ratio of measurable range to resolution.

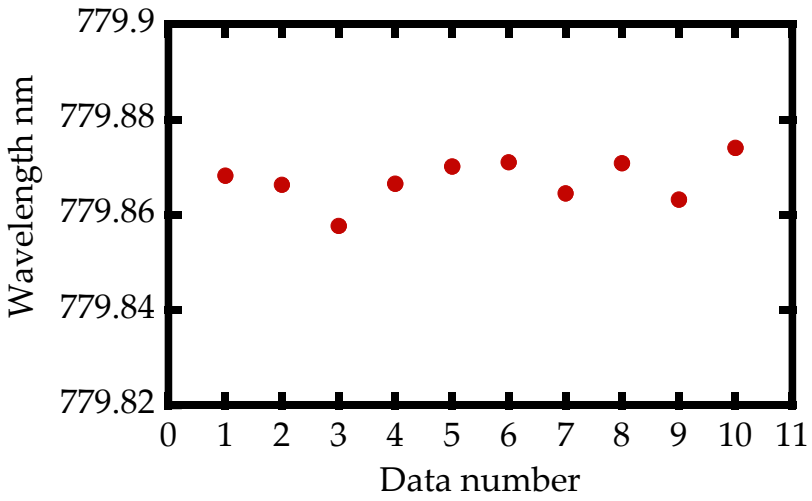

Figure 4.21 Experimental result of noise level using the standard deviation of the center-of-gravity wavelength calculation for each data point

Table 4.7 The experimental results of the proposed angle measurement system.

Standard deviation 2*S* nm	**Sensitivity nm/arc-second**	**Resolution arc-second**	**Angle range arc-second**	**Dynamic range**
0.00943	0.00311	3.03	20880	6891

4.5.4 Angle measurement evaluation with the influence of different index of refraction

The diffraction of a laser beam is one of the optical properties that cannot be eliminated in verifying the proposed method due to crystal usage. In general, the incident laser beam that passes through the boundary of two media with different refractive indices will propagate following Snell's law, as schematically shown in Figure 4.22 and expressed as follows [14].

$$\sin\theta_i = n_c \sin\theta_r \tag{4.10}$$

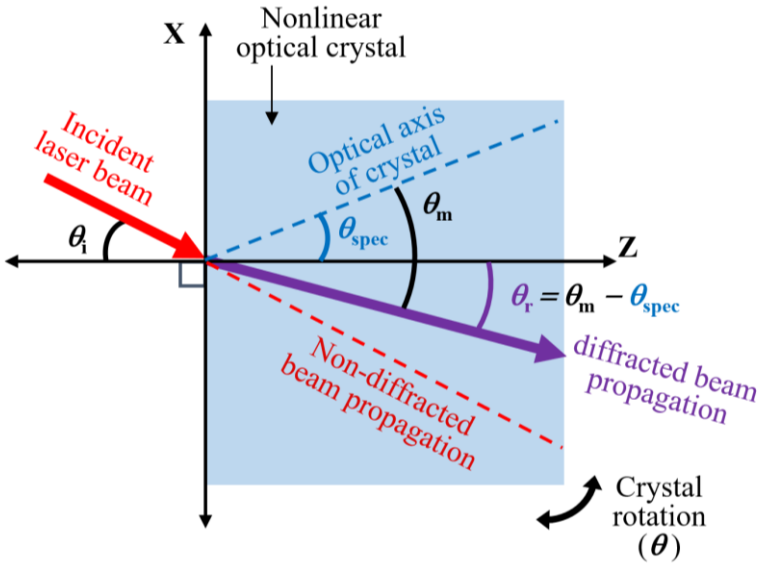

Figure 4.22 Schematic of refraction effect due to crystal diffraction; the change in direction of an incident laser beam through a nonlinear optical crystal

The figure above considers a case where the crystal is assumed to be a rectangular parallelepiped and a certain wavelength satisfies the phase-matching angle (θ_m). The angle between the normal axis and optic axis crystal is marked as θ_{spec}, the incident angle is θ_i, the refraction angle is θ_r, the refractive index of the crystal is n_c, and the refractive index of air is assumed as 1. The relations of those parameters are described by the following equations.

$$\theta_r = \theta_m - \theta_{spec} \tag{4.11}$$

$$\theta_i = \sin^{-1}\left\{\sin\left(n_c\left(\theta_m - \theta_{spec}\right)\right)\right\} \tag{4.12}$$

It is noticed that crystal diffraction will affect the SHG calculation because the incident angle to the optic axis of the nonlinear crystal to achieve the phase matching condition must be greater than the assumed incident angle. Moreover, the sinc function will also change.

Let the measurement trend lines analyzed by the centroid method, shown in Figure 4, be modified following Snell's equation. The modified calculation that considers the refraction is found to concur with the experimental result, as shown in Figure 4.23. Here, the result is displayed as the spectral peak shift with respect to the phase-matching angle of MgO:LiNbO3 crystal. The results are plotted so that the angular displacement of the experiment and modified calculation are consistent at the wavelength of 780 nm.

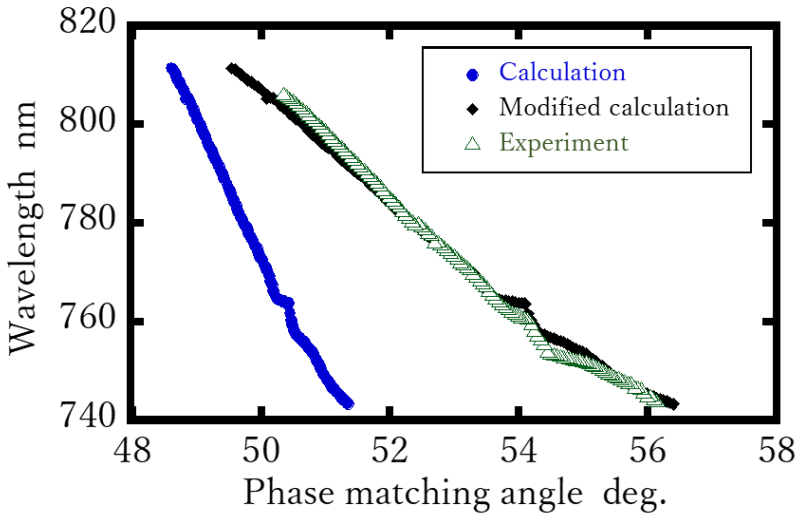

Figure 4.23 Comparison between angle measurement result from experiment and modified calculation with the influence of refraction.

The proposed SHG angle detection in the wavelength domain has a high reproducibility because the measurement is based on the observed wavelength that is

not affected by the intensity fluctuation of the FW. An even higher resolution and dynamic range can be obtained by increasing the signal-to-noise ratio with higher incident FW power. A supercontinuum source, for example, is another option to get a wider measurable range. However, the use of higher incident FW power must pay attention to the side effects that can affect the performance of the angle sensor, for example, the heat effect, which is very commonly found in the use of high-intensity laser sources.

4.6 Summary

A new optical angle measurement method has been proposed by using the unique characteristic of high peak power and wide spectral range of the femtosecond laser pulses, which can generate second harmonic waves in a wide spectral range. The angle detection method is presented in the wavelength domain to realize the absolute angle measurement. The theoretical analysis results have clarified that the widest measurable range can be achieved in the case that MgO:$LiNbO_3$ crystal is employed for the proposed angle measurement method. In the experiment, the validity of using a parabolic mirror has been demonstrated, where the chromatic aberration of the focusing beam has occurred in the localization of SHG in previous research can be solved by using an off-axis parabolic mirror for beam focusing. The experimental results with the developed measurement system have demonstrated the feasibility of the proposed angular measurement. Moreover, it has been clarified that the refraction of the interface between the air and nonlinear optical crystal should be considered. As a result, the measurable range of 20000 arc-second and measurement resolution of 3.03 arc-second has been achieved.

4.7 References

1. Shimizu Y.; Matsukuma H.; Gao W. Optical angle sensor technology based on the optical frequency comb laser. *Applied Sciences*. **2020**, 10, 4047, 1-22.

2. Chen YL.; Shimizu Y.; Tamada J.; Kudo Y.; Madokoro S.; Nakamura K.; Gao W.; Optical frequency domain angle measurement in a femtosecond laser autocollimator. *Optics Express.* **2017**, 25(14), 16725-16738.

3. Chen YL.; Shimizu Y.; Tamada J.; Nakamura K.; Matsukuma H.; Chen X.; Gao W.; Laser autocollimation based on an optical frequency comb for absolute angular position measurement. *Precision Engineering*. **2018**, 54, 284-293.

4. Shimizu Y.; Kanda Y.; Ma X.; Ikeda K.; Matsukuma H.; Nagaike Y.; Hojo M.; Tomita K.; Gao W.; Measurement of the apex angle of a small prism by an oblique-incidence mode-locked femtosecond laser autocollimator. *Precision Engineering*. **2021**, 67, 339-349.

5. Liang, X.; Wu, T.; Yang, L.; Wang, Y.; Liu, Y.; Zhu, J. Absolute angular measurement with optical frequency comb using a dispersive interferometry. Opt. Express **2020**, 28, 36095–36108.

6. Hong, L.H.; Chen, B.Q.; Hu, C.Y.; Li, Z.Y. Spatial-temporal evolution of ultrashort laser pulse second harmonic generation in β-barium borate (β-BBO) crystal. *J. Appl. Phys.* **2021**, *129*, 233102.

7. Dmitriev V.G.; Gurzadyan G.G.; Nikogosyan D.N. *Handbook of nonlinear optical crystals*, 3rd ed. Springer; Berlin 1999**.**

8. Sutherland, R.L. *Handbook of nonlinear optics*, 2nd ed. Marcel Dekker; New York, 2003.

9. Mills, D.L. *Nonlinear optics basic concepts*. Springer-Verlag; Berlin, Heidelberg, 1991.

10. Boyd, R.W. Nonlinear Optics, 3rd ed. Elsevier: Amsterdam, The Netherlands, 2008.

11. Manzoni, C.; Cerullo, G. Design criteria for ultrafast optical parametric amplifiers. *J. Opt.* **2016**, *18*, 103501.

12. Astuti, W.D.; Matsukuma, H.; Nakao, M.; Li, K.; Shimizu, Y.; Gao, W. An optical frequency domain angle measurement method based on second harmonic generation. *Sensors* **2020**, *21*, 670.

13. Sato, R.; Chen, C.; Matsukuma, H.; Shimizu, Y.; Gao,W. A new signal processing method for a differential chromatic confocal probe with a mode-locked femtosecond laser. *Meas. Sci. Technol.* **2020**, 31, 094004.

14. Peatross, J.; Ware, M. *Physics of Light and Optics*. optics.byu.edu 2015.

Chapter 5
Optimization of wavelength-dependent SHG angle sensor

5.1 Introduction

Various studies are still being carried out to improve the performance of angle sensors even though many types of angle sensors have been established and commercialized with various measurement methods and models for specific measurement purposes [1-4]. Research on conventional angle sensors such as inductive angle positioning sensors [5,6], autocollimators [7,8], and rotary encoders [9,10], is no exception. The angle-sensing technology is still a challenge to meet the need for current trends in technology that lead to the manufacturing of high complexity products yet shrinking in dimensions. It requires a suitable angle sensor that is not limited by the type of material being measured, has minimal potential damage to the material during the measurement process, and is expected to have minimal maintenance costs [11,12]. An inductive angle positioning sensor, for example, has limitations for detecting the metal target only. Meanwhile, the autocollimator is

time-consuming in operation as it is hardly positioned and requires regular maintenance, and the rotational magnetic encoder commonly contains fine parts that are sensitive to contamination. These reasons encourage more intensive research on new angle measurement methods, especially non-contact angle sensors, as the solution to bridge these problems.

A second harmonic wave angle sensor, a non-contact optical-based angle sensor, offers a well-suited measurement configuration system to satisfy the aforementioned requirements [13,14]. The second harmonic generation (SHG) is a phenomenon in which the optical wave source passes through a nonlinear optical material and generates a frequency-doubled harmonic wave where the power of the second harmonic wave is highly dependent on the wavelength and the incident angle of the source toward the nonlinear material [15]. SHG has attracted attention because of its advantages that can be found in many fields of study, especially in the biological and medical sciences for bioimaging spectroscopy [16–18], nonlinear microendoscope [19,20], and surface chemistry sensing [21,22]. However, the application of SHG in angle displacement measurement is relatively new, and related research is still limited.

In the previous chapters, a new angle measurement based on the SHG by focusing a Femtosecond laser (Fs) laser beam with lenses [13] and a parabolic mirror [14] into a nonlinear optical (NLO) crystal serving as a measurement target has been proposed with intensity-dependent and wavelength-dependent measurement. The focused beam method is one practical way to obtain highly intense fundamental waves of Fs laser for generating harmonic waves. A good performance has been achieved when the NLO crystal is placed at the focal point or within the Rayleigh length region of the parabolic mirror, where the beam can be treated to have a plan wave nature. This measurement method holds promise in the angle shift detection of fixed-positioned measurement targets but could encounter problems when the target has misalignment along the laser propagation direction. To accommodate possible changes in position on the axis, a new SHG angle sensor configuration is needed.

This chapter proposes an optimization of the angle sensor using the SHG generated by a collimated Fs laser beam instead of a focused Fs laser beam. A collimated beam is expected to have no significant change in physical properties during propagation. The Fs laser beam is highly collimated, but a more intense laser beam is required to generate the second harmonic wave. Therefore, a Keplerian lens configuration is needed to intensify the laser beam while keeping the beam collimated. Theoretical calculations are carried out to predict the sensor's performance, and the feasibility of the angle sensor is confirmed experimentally. In the experiment, the beams are aligned so that they propagated through the NLO crystal to produce SHG, where the NLO crystal is mounted on a rotary stage representing the target to be measured. Since the SHG in the crystal is strongly related to the angle and the wavelength, the small angular change of the crystal can be directly detected by the SHG spectrum change in a given wavelength range. The peak of the SHG spectral evolution as the angular position of the crystal changes is then evaluated to determine the sensitivity of the angle sensor. Finally, to confirm the feasibility of the measurement method where the target does not have to be placed in one position, experiments are carried out at several positions of the NLO crystal along the beam propagation direction.

5.2 The principle of wavelength-dependent angle sensor with collimated beam

The principle of wavelength-dependent angle sensor with collimated beam has no different from the measurement principle in the previous chapter. The optimization angle sensor is based on SHG, which occurs when an NLO crystal is irradiated with a laser beam of a certain frequency w producing radiation at twice the initial frequency of $2w$ [15,23]. Since the light frequency is inversely proportional to the light wavelength, the FW having a wavelength λ generates a second harmonic wave having a wavelength $\lambda' = \lambda/2$. SHG can be employed in angle measurement due to the birefringence in the uniaxial NLO crystal that divides the laser beam into two different

rays, the ordinary ray (referred to as the o-ray in the following) and the extraordinary ray (referred to as the e-ray in the following). Both the rays experience their respective refractive indices inside the crystal. In a certain condition where the optical path lengths of these beams are identical inside the crystal, phase-matching occurs, and the light intensity of the second harmonic wave is maximized. Note that for any given λ, the phase-matching condition could arise in its corresponding matching angle $\theta_{m,}$ which can be estimated by following Equation 2.19 in Chapter 2. [14, 24].

Regarding the usage of the NLO crystal in the proposed angle sensor, the NLO crystal is required to have a large angular dispersion for the wavelength range of an Fs laser to be employed in the angle sensor. In this study, an Fs laser whose optical spectrum ranges from 1480 nm to 1640 nm is used. MgO: $LiNbO_3$ is thus one of the suited crystals that fulfill the requirement because the phase-matching angle of the crystal within the given wavelengths range shows the large angular dispersion as explained in Chapter 2 [13,14]. Since Fs laser has a wide range of wavelength, when a certain wavelength is at a matching angle in which high SHG intensity is achieved due to high efficiency, other wavelengths in the same angle undergo phase mismatch with lower intensity. The phase matching and phase mismatch features of the SHG will appear simultaneously in an optical spectrum analyzer (OSA) in the form of a spectrum [25]. The phase-matching of other wavelengths can thus be satisfied when the MgO: $LiNbO_3$ crystal experiences angular displacement about its Y-axis. By utilizing this characteristic, angle measurement can be carried out by monitoring the peak wavelength of the second harmonic wave.

The performance and measurement trend of the optimization can be estimated using a similar calculation design in Chapter 3. However, the higher output power of Fs with different characteristics of the fundamental wave is used in this study and will be discussed in the next section.

5.3 Experiment design and procedures

In this section, the detailed experiment procedures and results will be discussed.

Due to the configuration of the angle sensor that is employing the collimated beam as the laser source, the experimental procedure is divided into two main procedures. First, light intensification was carried out, followed by the beam output observation at several observation distances to confirm the collimation of the beam. The fact that the collimated beam is cannot be realized experimentally, makes the collimation of the beam is in the approximation scheme when the divergence angle must be as small as possible. The second experiment was the angular shift detection with the vary of crystal positions to confirm the feasibility of the measurement method to overcome the target misalignment problem along the Z-axis.

5.3.1 Beam intensifying setup

Aside from the NLO crystal preference mentioned in Chapter 2, high intensity of the fundamental wave is required to generate a second harmonic wave with microwatts to milliwatts power. In the previous work, the Fs laser with relatively low power is used. Therefore, the focused beam method is applied to gain a higher power density to generate SHW. This beam intensifying model is less effective since the combination of the parabolic mirror and nonlinear crystal has the limitation in crystal size and depth of focus, and restricts the working distance since the crystal must have been placed in the focal point. Therefore, a collimated fundamental wave whose light intensity is intensified by reducing the beam diameter is employed to address the issues. The higher power femtosecond laser (C-Fiber High Power, Menlo System) is employed in this optimization angle sensor where the specification of this Fs laser is tabulated in Table. 5.1. Even so, the power density of the new Fs laser is still not sufficient to generate the second harmonic wave and the reduction of the beam is conducted. Figure 5.1 shows an example of the optical setup based on the Keplerian configuration that reduces the beam width. The following relationship can be found between the initial beam diameter d_1 and the expected beam d_2:

$$d_2 = \frac{d_1 f_2}{f_1} \quad . \tag{5.1}$$

Where the focal length of the first lens and the second lens are denoted by f_1 and f_2, respectively with the provision of $f_1 > f_2$. In this study, the lenses with the focal length of 150 mm and 75 mm are set as the 1st plano-convex lens and the 2nd plano-convex lens in the experimental configuration.

Table 5.1 Specification of the femtosecond pulse laser source with higher output power

Components	Information
Manufacturer	Menlo Systems GmbH
Model number	C Fiber High Power
Wavelength	1560 nm ± 20 nm
Average Power	>500 mW
Pulse Width	<90 fs
Repetition Rate	100 MHz
Repetition Rate Instability	<1 ppm over 20h at constant temperature

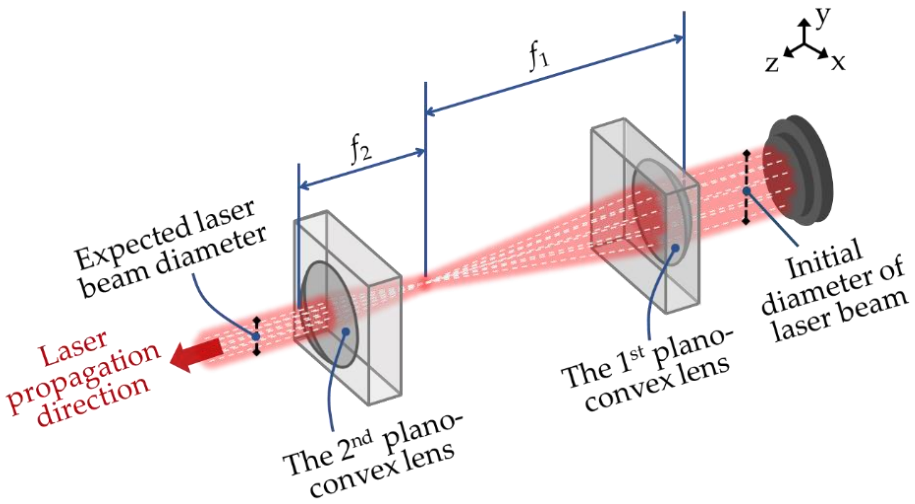

Figure 5.1 A schematic of the setup reducing the collimated beam width with a pair of plano-convex lenses [26].

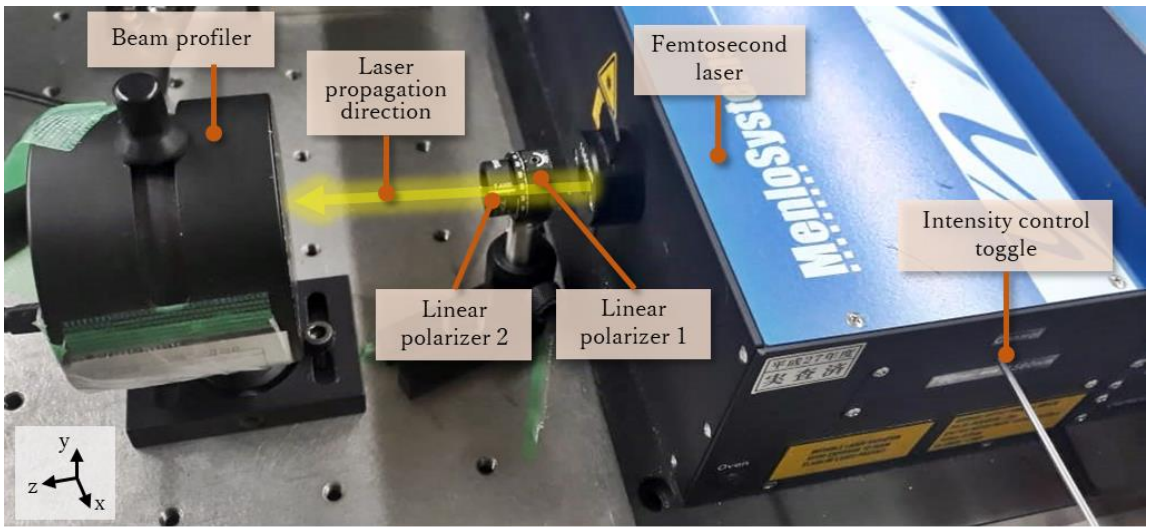

Figure 5.2 Experimental setup of initial beam output observation.

Figure 5.2 shows the schematic experimental setup to observe the initial output of the Fs laser. Two polarizers are set in place to prevent the beam profiler from being damaged by the high-power density of the Fs laser. In the experiment, the transmission axes of the polarizers were set nearly perpendicular so that the beam intensity was low enough.

The collimation of the beam is still necessary to be checked after the beam reduction. As a direct technique to verify it, the beam profiler is employed to observe the beamwidth at various observation distances as well as to confirm the collimation of the beam. Figure 5.3a exhibits the schematic of experimental setup and Figure 5.3b displays a photograph of the experimental setup. An evaluation of the beamwidth against the propagation distance is carried out to determine whether a collimated beam is formed. Since the ideal collimated beam cannot be realized experimentally, in this experiment, the beam is considered to be collimated if the divergence angle is in close proximity to zero degrees. The divergence angle is determined by the arctan value of the linear fit slope of the beamwidth observation trend and for the case when the slope is very less, the divergence angle is equivalent to the slope itself.

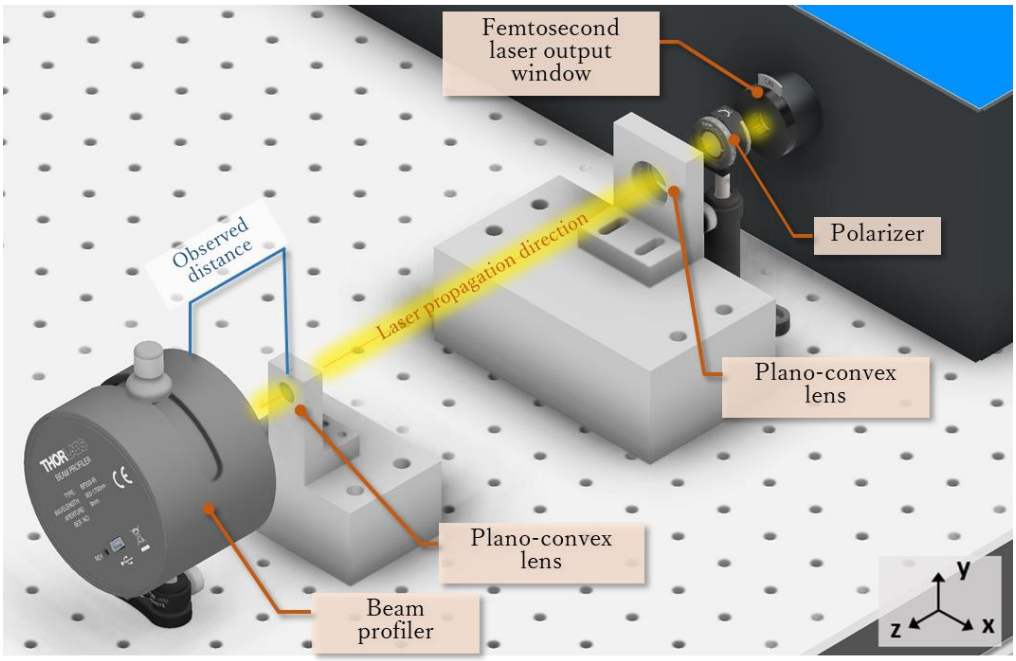

(a)

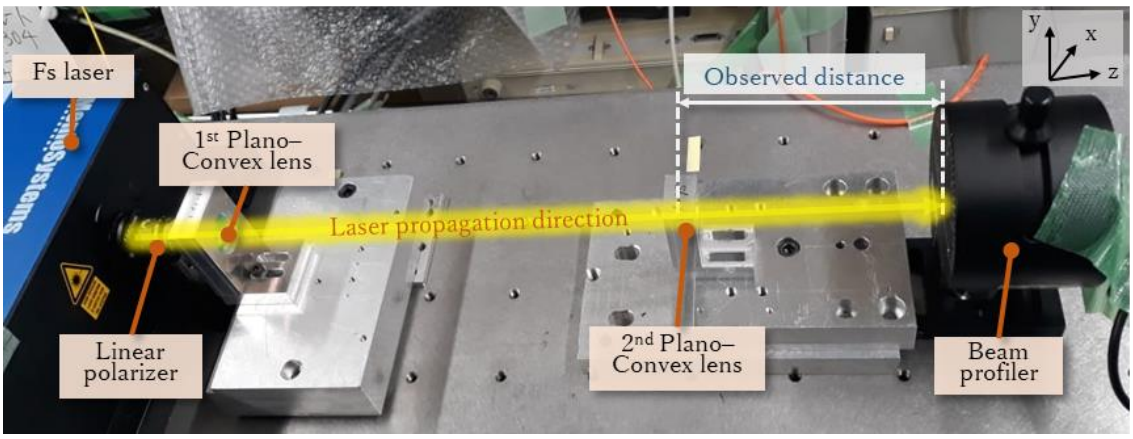

(b)

Figure 5.3 Experimental setup of beam observation; (**a**) A schematic of the beam collimation observation; (**b**) A photograph of the experimental setup.

5.3.2 Experimental setup of angle measurement

Similar to the experiment in the previous chapter, the angle change in this experiment is done by rotating the crystal mounted in the rotary stage that represents the angle shift of the measurement target. The rotary stage is shifted by the given pulse. In the previous chapter, the pulse-angle shift conversion is calculated by calculating the pulse with the average value of the rotary stage angle-shift that is separately observed by the autocollimator. Since the rotary stage movement is not stable and does

not give the absolute angular displacement of the rotary stage due to the interval pulse given, the new configuration is proposed.

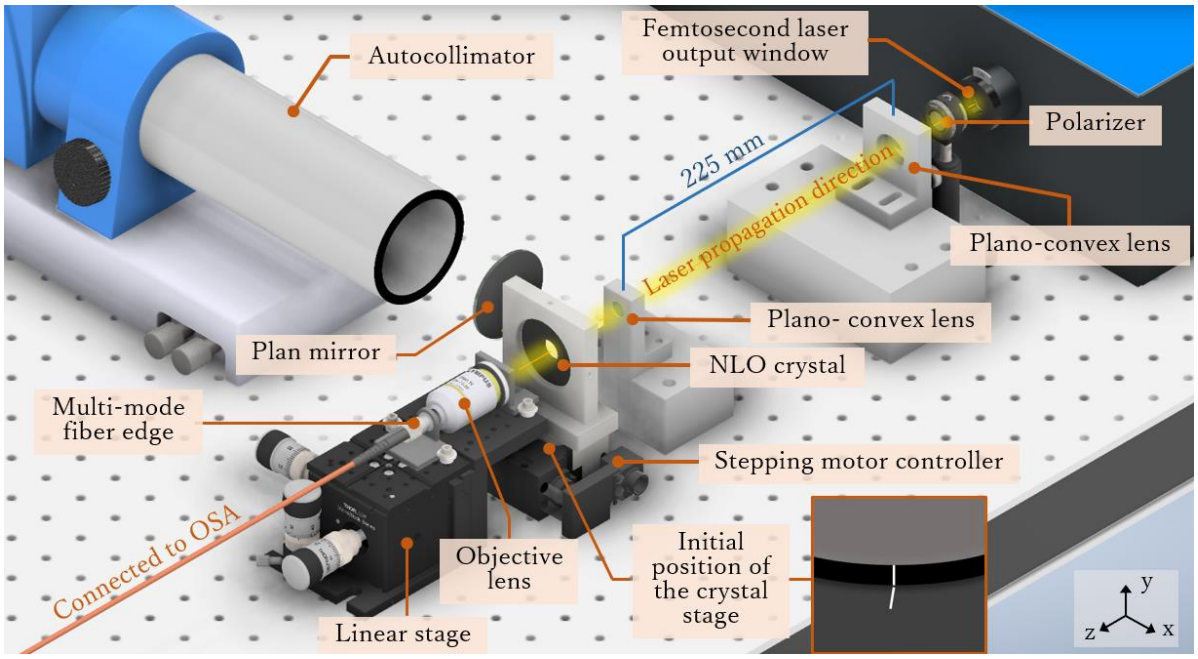

(a)

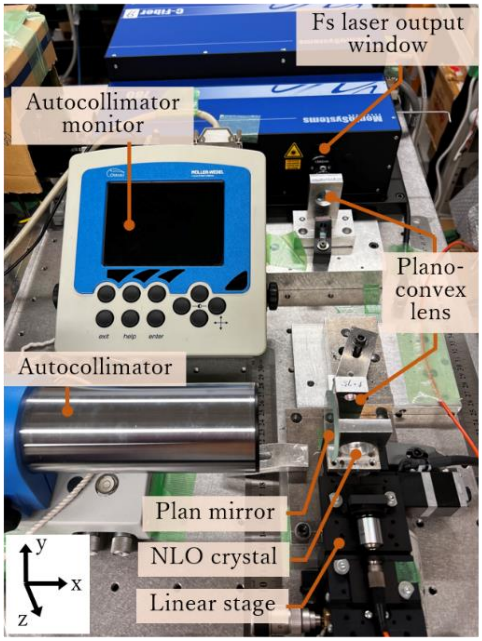

(b)

Figure 5.4 Experimental setup of wavelength-dependent angle sensor with collimated beam femtosecond laser; (a) A schematic of proposed angle sensor; (b) A photograph of the experimental setup [26].

Figure 5.4a shows the experimental setup of the angle sensor with collimated beam with the a autocollimator installed to check the angular displacement as another

method to confirm the absolute angular movement of the rotary stage due to the given pulse, and Figure 5.4b shows the photograph of the experimental setup. As can be seen in the figure, the initial position of the rotary set is set such that the two indicator lines on the rotary plate and the surface of the stepping motor controller meet. At this point, the incident laser is assumed to be perpendicular to the crystal surface. The detection of the angular displacement was carried out by observing the evolution of the SHG spectrum with respect to the changes in the angular position of the crystal. The detection continued by varying the z-position of the crystal. The autocollimator ensured the angular position of the crystal throughout the entire experiment. The sensitivity of the angle sensor was determined by concerning the slope of the measurement trend based on the SHG peaks changing versus respective angle shifts.

5.4 Calculation result

Using the fundamental wave characteristics of the Fs laser, the theoretical calculation was performed to estimate the SHG characteristic of the angle sensor as well as to predict the measurement trend of the proposed angle sensor. Figure 5.5 shows the FW spectrum of the Fs laser with a higher power in which the fundamental power for calculation is extracted. The OSA sensitivity is set to the "MID" setting during data recording with 500 sampling data within the wavelength range from 1480 nm to 1640 nm.

The calculation result based on the birefringence equation is displayed in the 2D plot and a 3D plot in Figure 5.6a and Figure 5.6b, respectively. The localized intensities are found in the figure due to the characteristic of FW where the FW spectrum consists of peaks and sudden drops of power in several wavelengths. From the result, the spectral peaks were determined by using the highest intensity method over the change in angular position of the MgO: $LiNbO_3$ crystal.

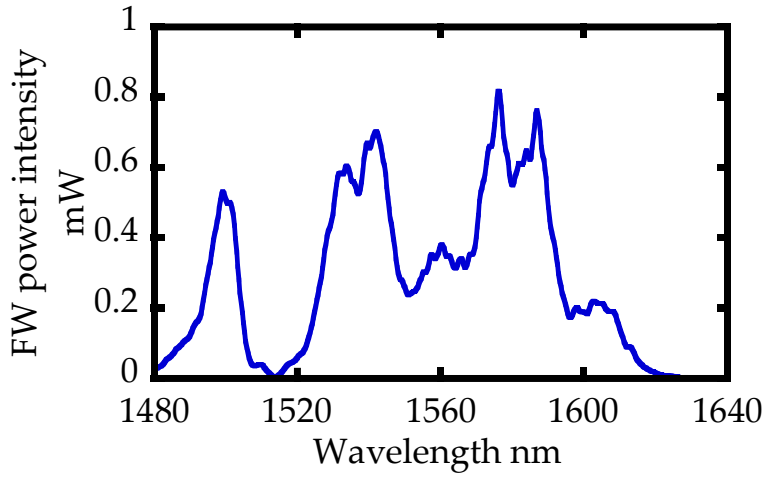

Figure 5.5 Fundamental wave spectrum of Fs laser with higher power

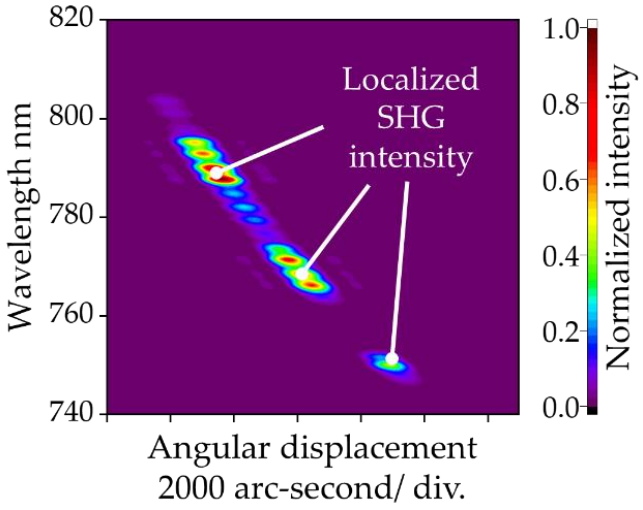

(a)

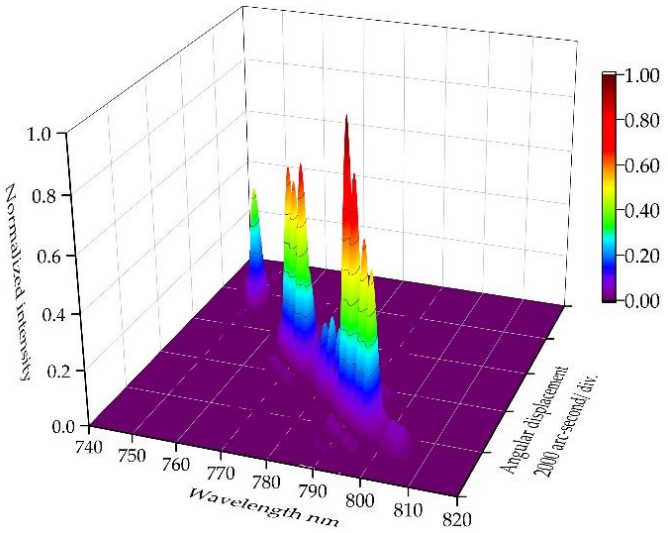

(b)

Figure 5.6 The SHG spectra characteristic based on the birefringence calculation result; (a) The 2D plot; (b) The 3D plot.

The angular displacement calculated based on the change in the spectral peak is presented in Figure 5.7a; this result estimates the measurement trend. As can be seen in Figure 5.7b, a sensitivity of 0.00725 arc-second/nm was observed in the most extended measurement range within the angle range of approximately 6000 arc-second, while sensitivity of 0.00226 arc-second/nm was observed in the least measurement range within the angle range of approximately 2000 arc-second, as shown in Figure 5.7c. Although the calculated yield trendline was not as smooth as the calculated MgO: $LiNbO_3$ phase-matching angle trend line shown in Figure 2.7b of Chapter 2, but still showed a nearly similar angle-wavelength dependence tendency.

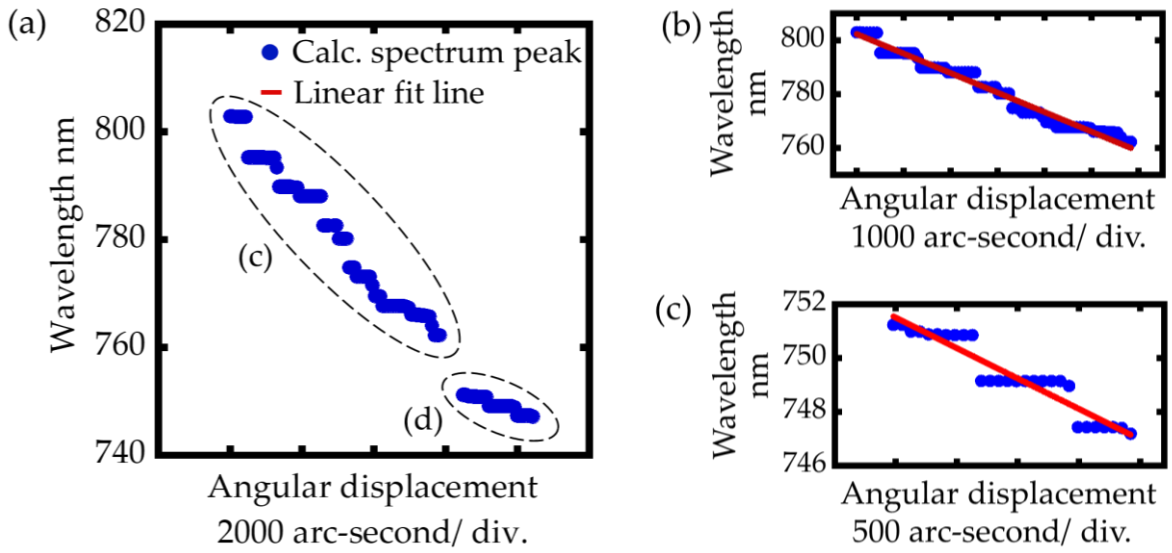

Figure 5.7 The measurement trendline based on the peak of the calculated SHG; (**a**) The undivided measurement trend line; (**b**) The trendline of the most extended angle range area; (**c**) The trendline of the least angle range area.

A close observation of the results shows the presence of the split peaks that causes the localized SHG intensities and discrepancy of the measurement trend line. For instance, Figure 5.8 shows one of the split peaks that appeared at the matching angle of 50.18º. The split peak caused two peaks of the SHG spectrum to detect a specific angle position simultaneously.

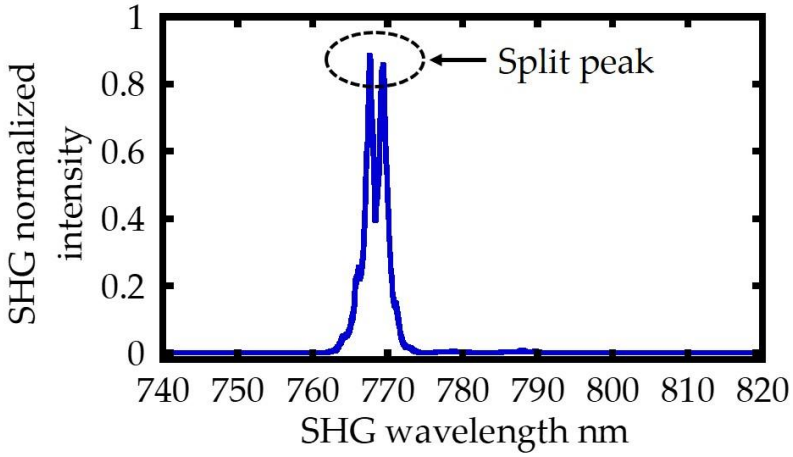

Figure 5.8 Calculated SHG spectrum in the split peak region

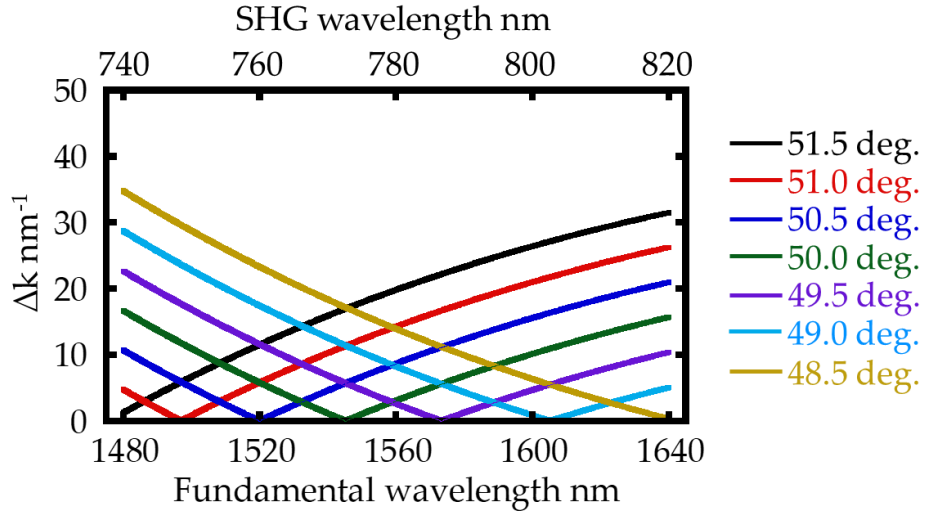

(a)

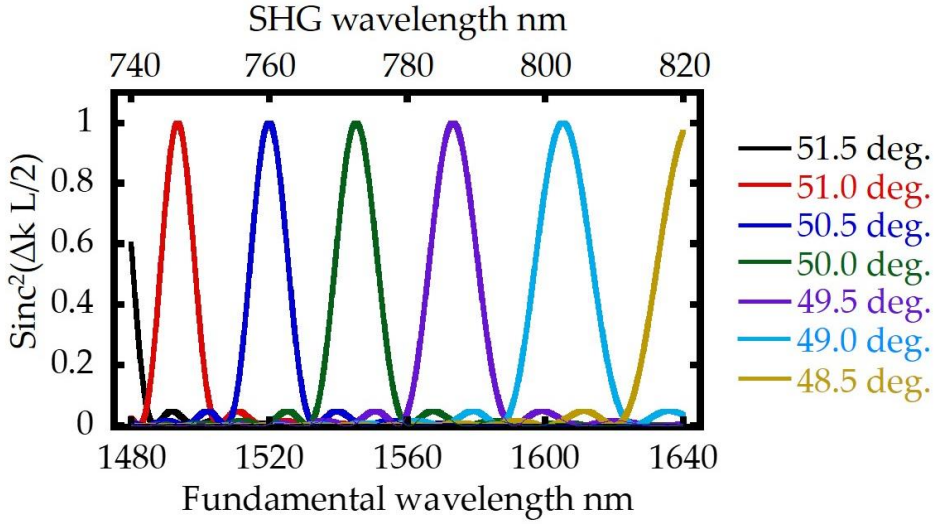

(b)

Figure 5.9 (**a**) The dynamics of phase mismatching for a certain angle; (**b**) The sinc quadratic function characteristic due to the dynamics of phase mismatch for a certain angle

Further analysis of the calculations was carried out to explore the measurement dynamics. Figure 5.9a shows the dynamics of phase mismatch for certain angle and Figure 5.9b shows the dynamics of sinc quadratic function. As shown in Figure 5.9a, a certain angular phase mismatch for a given wavelength established a pattern that affected the sinc quadratic function in Figure 5.9b. The peaks of sinc quadratic function gradually narrowed with the increase of angle. Since the sinc quadratic function was applied to the FW spectrum in Figure 5.5 consisting of peaks and valleys, the second harmonic wave spectrum was dynamically changed, and the split peaks were unavoidable.

5.4 Experimental result

5.4.1 Beamwidth evaluation for beam collimation verification

One of the first steps to producing a collimated laser beam is the observation of the Fs laser output profile. Figure 5.10a shows the profile of the collimated beam light distribution at its initial condition, which was observed at the cross-sectional Z-axis. Figure 5.10b shows the X-direction and Y-direction of the cross-sectional profile. The beam is defined as the $1/e^2$ value of those gaussian-like intensities. The beam width was evaluated as 2117 μm and 2195 μm along with the X and Y directions, respectively. The direct use of the Fs laser with this output is not sufficient to generate the SHW, thus beam reduction is required.

The reduction of the beam width was successfully carried out using the setup shown in Figure 5.3. The results presented in Figure 5.11 shows the change in the beamwidth as the increase in observation distance. As shown in the figure, the X-direction diameter showed more consistent results than the Y-direction diameter upon the variation of observation distance. Since the dispersion angle was small at the observation distance from 10 mm to 140 mm, the produced laser was treated as a collimated laser beam. The evaluation of this collimated beam is tabulated in Table 5.2. It is found that the beamwidth from the experiment is smaller than the value estimated by Equation 5.1, 1058.5 μm in the X-direction and 1097.5 μm in the Y-direction. This

discrepancy was due to the initial profile of the Fs laser beam; as the profiler was positioned farther than the 1st plano-convex lens, the beam at this position could experience dispersion resulting in the detection of the profile with a larger diameter.

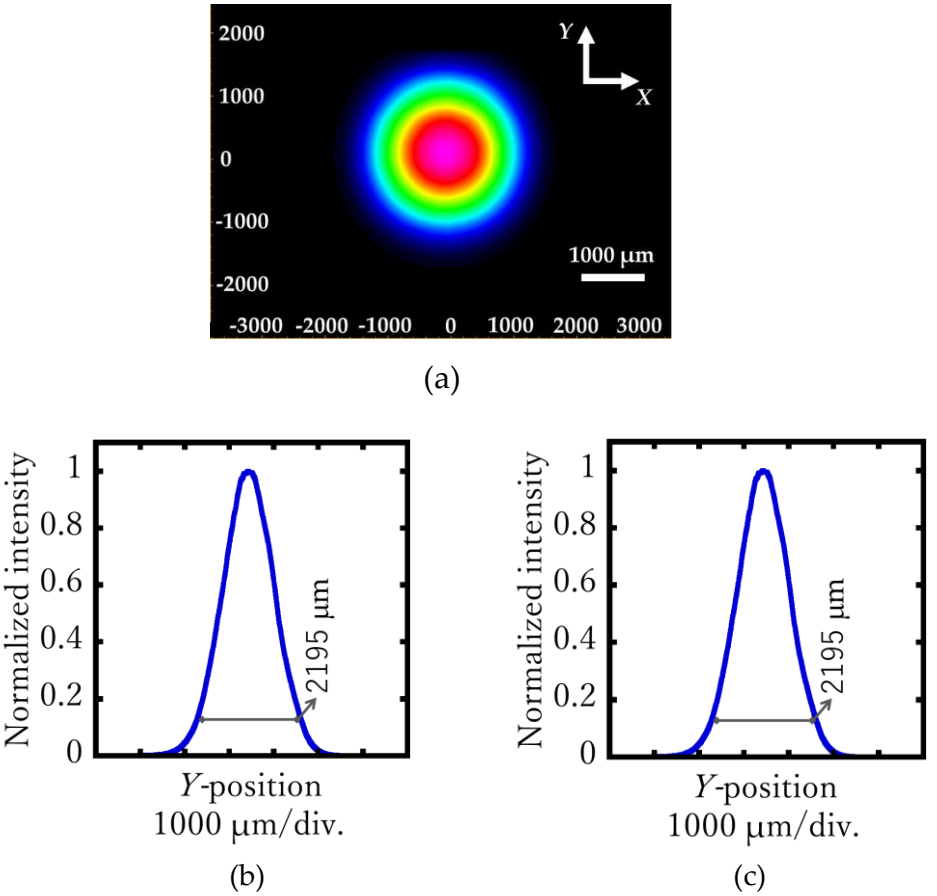

Figure 5.10 The initial beam profile of Fs laser; (**a**) Light intensity distribution; (**b**) Cross-sectional profiles of X-axis; (**c**) Cross-sectional profiles of Y-axis.

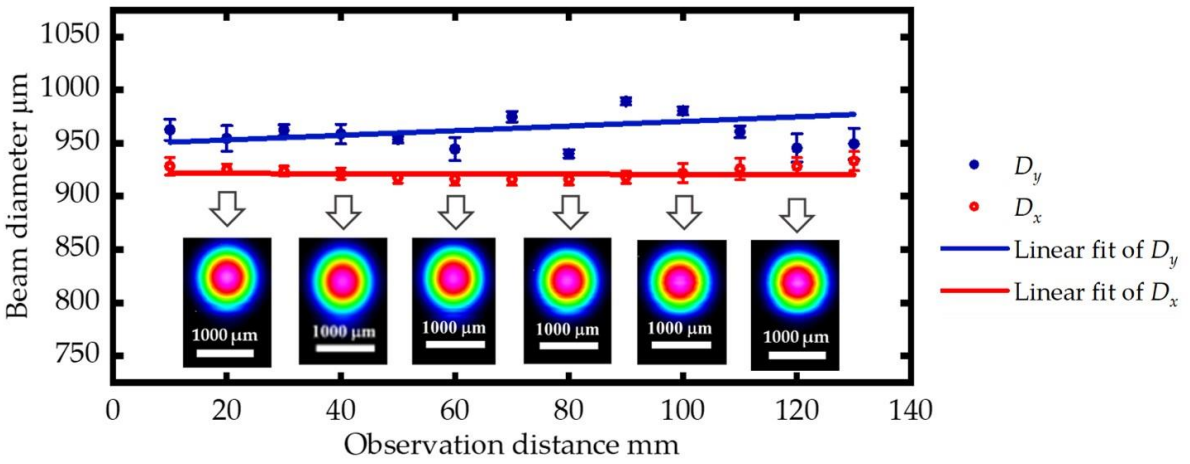

Figure 5.11 The change in beam width as the observation distance increase.

Table 5.2 The diameter of generated collimated laser beam.

Profile direction	Diameter	Angle of dispersion
X	(921.83±3.00) μm	2.53 arc-second
Y	(948.70±13.47) μm	44.79 arc-second

Since the proposed angle is wavelength-dependent and based on spectral behavior identification, the observation of the Fs laser output as the FW is needed. Figure 5.12 shows the spectral characteristics of the initial Fs laser output and the Fs laser output after the reduction of the beam diameter. The initial Fs laser output had a power density of 0.35 W/cm^2. In contrast, a smaller beam width produced a high-power intensity with a power density of 19.17 W/cm^2. Spectrum peaks are identified at several wavelengths with the highest intensity in the wavelength of 1576 nm. Meanwhile, the drop of power is identified with the lowest intensity in the wavelength of 1508 nm.

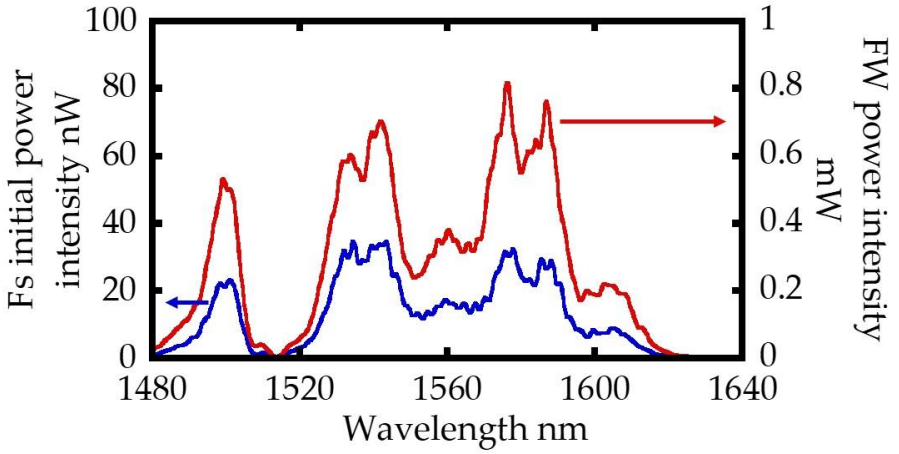

Figure 5.12 The comparison spectrum of initial Fs laser output and the Fs laser output after reduction of the beamwidth.

5.4.2 Variation of crystal position for feasibility test angle sensor

In order to confirm the feasibility of the angle sensor optimization, the measurement characteristics of the angle sensor are identified in several crystal positions. The performance was validated by observing the characteristic of the detected FW and second harmonic wave associated with angular change and the

variation of the crystal position, 30 mm, 50 mm, and 70 mm. The total power characteristic of FW and SHG will be presented in this section as well.

The observed FW spectrum and SHG spectra in the crystal position of 30 mm from the 2nd plano-convex lens are presented as a contour graph in Figures 5.13a and 5.13b, respectively. The SHG spectrum was taken with an interval of 100 pulses for 155 data. The localized intensity is found in the SHG contour graph in which the highest intensity is observed at the wavelength of 786.24 nm. The angle position in this area is assumed as the phase matching angle of the fundamental wavelength of 15572.48 nm. The localized intensities are also spotted in the other region with lower intensity as can be seen in the augmented contour graph of Figure 5.13b.

The total power of the FW and SHG spectrum for the crystal position of 30 mm over the angular displacement is presented in Figures 5.14a and 5.14b, respectively. The FW total power decreases as the crystal rotates, in which the incident angle of the laser toward the surface of the crystal increases. Meanwhile, the SHG total power contour graph shows that the highest total power is generated at an angle position where the highest SHG intensity is achieved at a wavelength of 786.24 nm.

Figures 5.15a and 5.15b show the observed FW and SHG spectra in the crystal position of 50 mm. The SHG spectrum was taken with an interval of 100 pulses for 170 data. The localized intensities are found too in the SHG contour graph in which the highest intensity is observed in the wavelength of 785.28 nm, and the augmented figure shows another region of localized intensities with lower intensity.

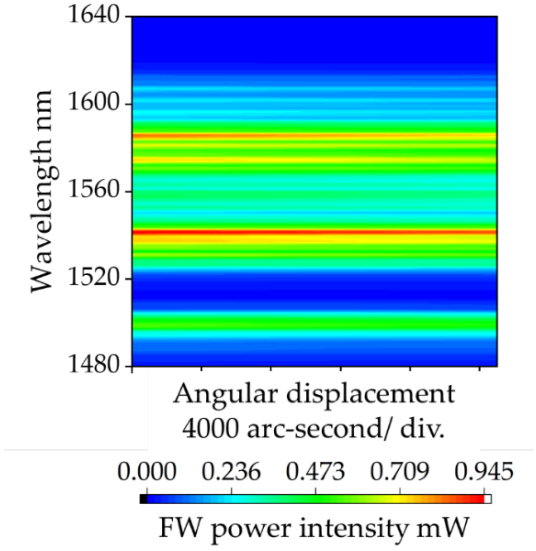

(a)

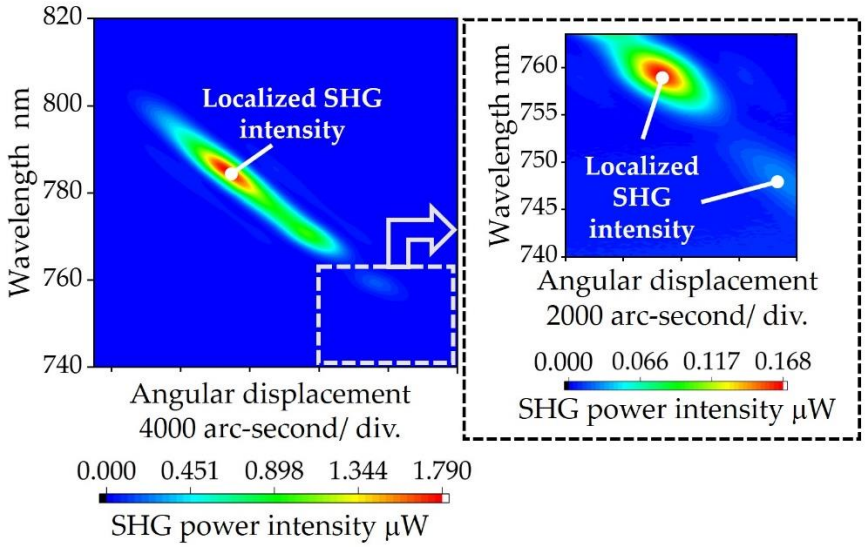

(b)

Figure 5.13 The observed spectrum contour graphs of 30 mm; (**a**) FW; (**b**) SHG.

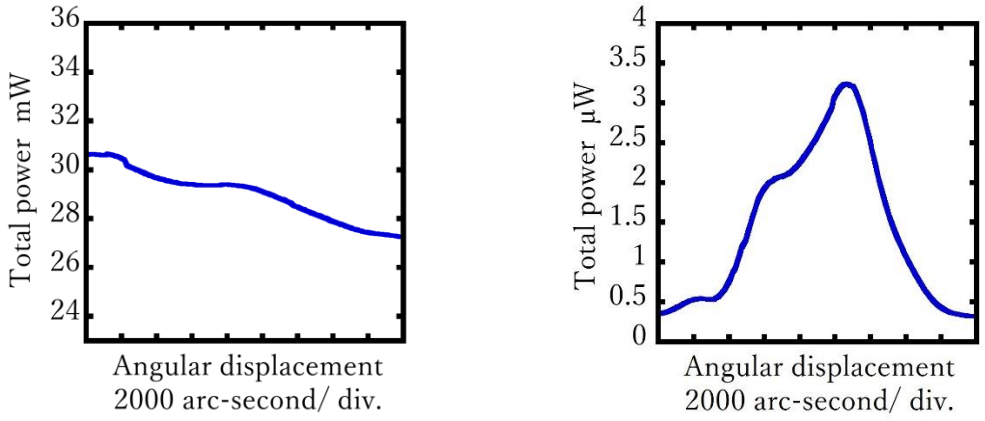

(a) (b)

Figure 5.14 The observed total power of 30 mm associated with the angular shift; (**a**) FW; (**b**) SHG.

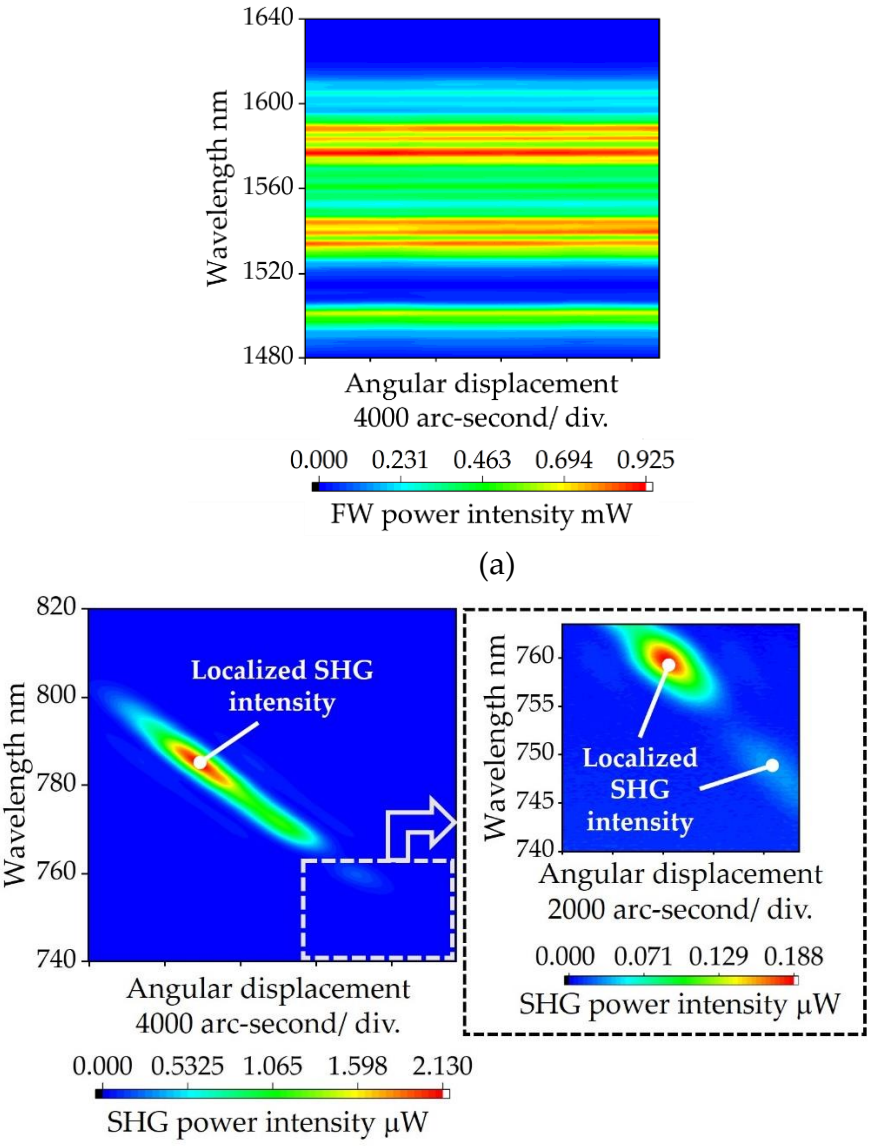

Figure 5.15 The observed spectrum contour graphs of 50 mm; (**a**) FW; (**b**) SHG.

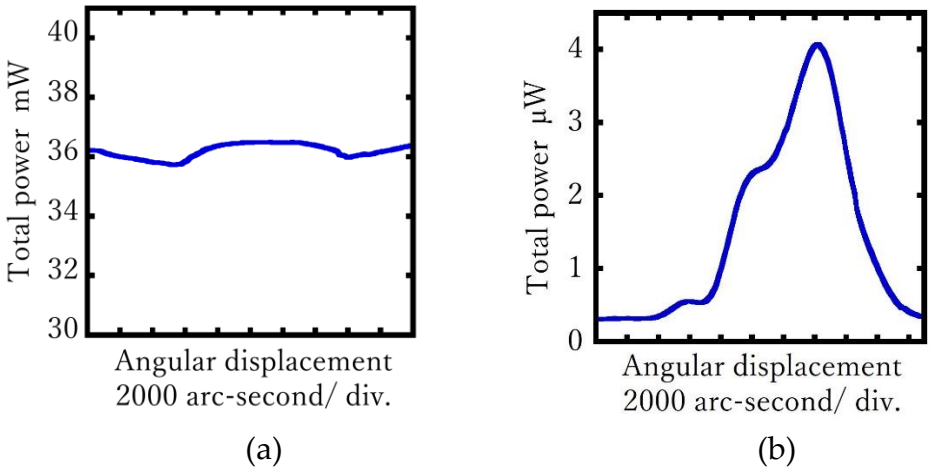

Figure 5.16 The observed total power of 50 mm associated with the angular shift; (**a**) FW; (**b**) SHG.

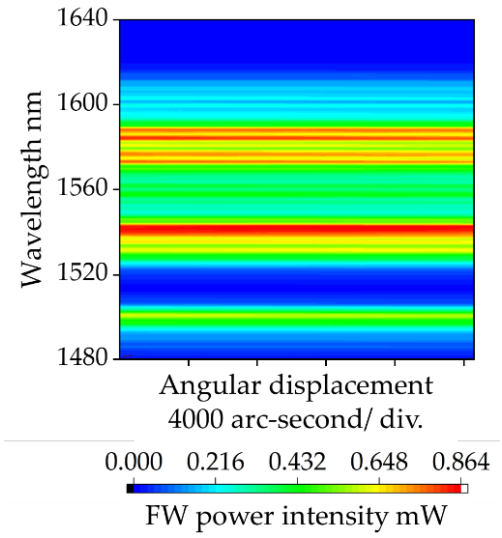

(a)

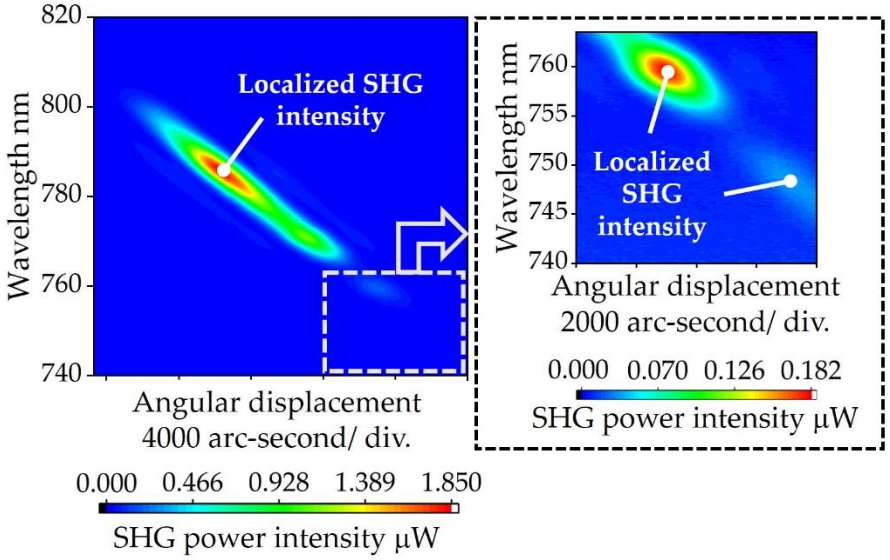

(b)

Figure 5.17 The observed spectrum contour graphs of 70 mm; (a) FW; (b) SHG.

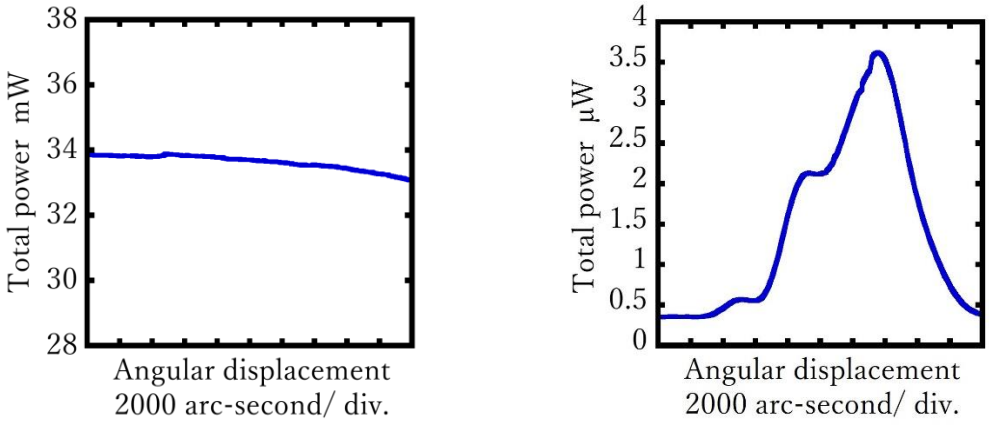

(a) (b)

Figure 5.18 The observed total power of 70 mm associated with the angular shift; (**a**) FW; (**b**) SHG.

The total power spectra of FW and SHG for the crystal position of 50 mm with respect to angular displacement are presented in Figures 5.16a and 5.16b, respectively. The total power characteristic of FW is different from the experimental result at the crystal position of 30 mm. It should be noted that the laser spectrum was observed using a multimode fiber connected to OSA. The multimode fiber is very sensitive to disturbances such as vibration or accidental contact with surrounding objects. The FW power intensity results in Figure 5.16a is believed to have such a trendline due to the external disturbance during the data recording. On the other hand, the SHG total power in Figure 5.16b has a similar trend with the result at the crystal position of 30 mm, even though it was observed in a wider angular position.

The last crystal position is 70 mm, in which the observation result of the FW and SHG spectrum is shown in Figures 5.17a and 5.17b, respectively. The spectra were taken with the interval of 100 pulses for 170 data. The highest intensity is observed in the wavelength of 785.28 nm, identic with the experiment result of 50 mm. The total power of FW and SHG spectrum for this crystal position are presented in Figures 5.14a and 5.14b, respectively and show a similar tendency to other crystal positions.

Those results are not identical, as indicated by the different ranges of power intensity. However, the characteristics of all observed FW show a similar tendency. On the other hand, Figures 5.13b, 5.15b, and 5.17b show the observed second harmonic wave that revealed a different contour profile compared to the calculation result in Figure 5.6a. It is noticed that there is an inconsistency of FW intensity and second harmonic wave when the crystal position is changed. Such inconsistencies were frequently encountered in the use of lasers, especially when re-alignment of the experimental setup was carried out. A different start point and endpoint of the angle measurement were observed in the figures because the initial position of the crystal was manually adjusted as previously mentioned in the experimental procedures section. However, it did not affect the sensor performance, as is proven by the measurement trendline that will be explained later. The localized SHG intensity appeared in all variations of crystal position. The augmented contour graphs give a

better view of the lower wavelength range area where the localized intensities are also spotted. Compared to one another, those results have a resemblance in characteristics and tendencies. It indicates that variations in crystal position along the laser beam propagation direction had no significant impact on the FW and SHG spectra.

The measurement trendline of all crystal positions will be discussed. The behavior of the spectral peaks towards the angular movement of the crystal shows the trend line of the angle sensor measurement. The spectral peak is determined by the highest spectral intensity for each angular position. Only the linear region is considered to calculate the measurement sensitivity. Unlike Chapter 4, the centroid method is not applied to determine the spectral peak in this study due to the presence of the split peaks in more than one area. The split peak condition leads to the change in the trend line around the split peak area, which causes the change in measurement sensitivity as well. As a consequence, the angular resolution considers the resolution of OSA only.

Figure 5.19 shows the measurement trend of the angle sensor, determined by estimating the SHG peak with respect to the angle transition at the 30 mm crystal position. As can be seen in Figure 5.19a, the characteristic spectral peaks of the angle sensor show three measurement trends with different sensitivities. The three different linear areas can be seen separately in Figures 5.19b, 5.19c, and 5.19d, where the measurement sensitivity of 0.00294 nm/arc-second and angle range of 13328.38 arc-second are achieved in the most extended measurement result.

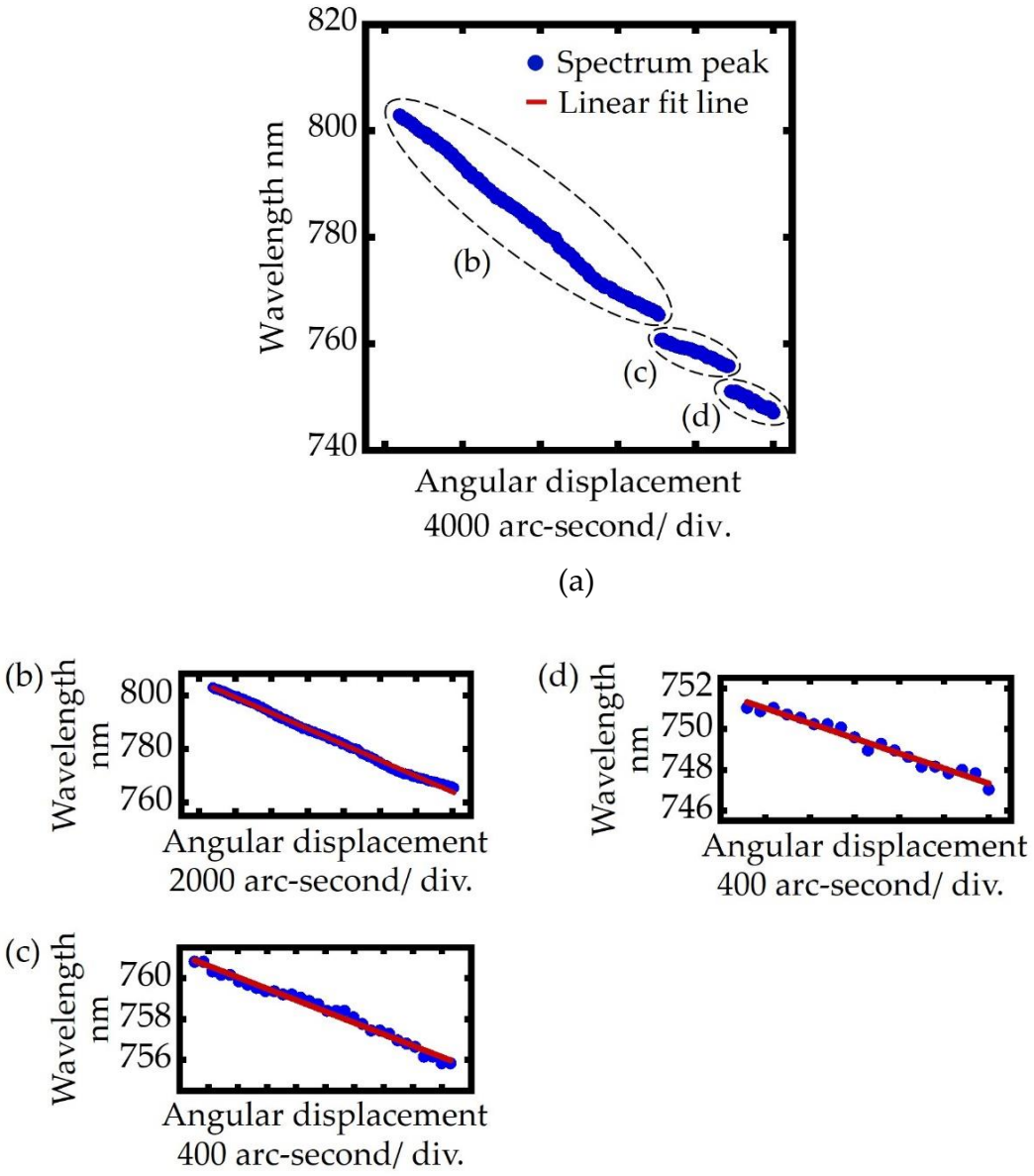

Figure 5.19 Angle measurement trend based on the peaks of SHG at the crystal position 30 mm; (**a**) the entire measurement trend line; (**b**) the most extended measurement area; (**c**) the middle range measurement area; (**d**) the least measurement area.

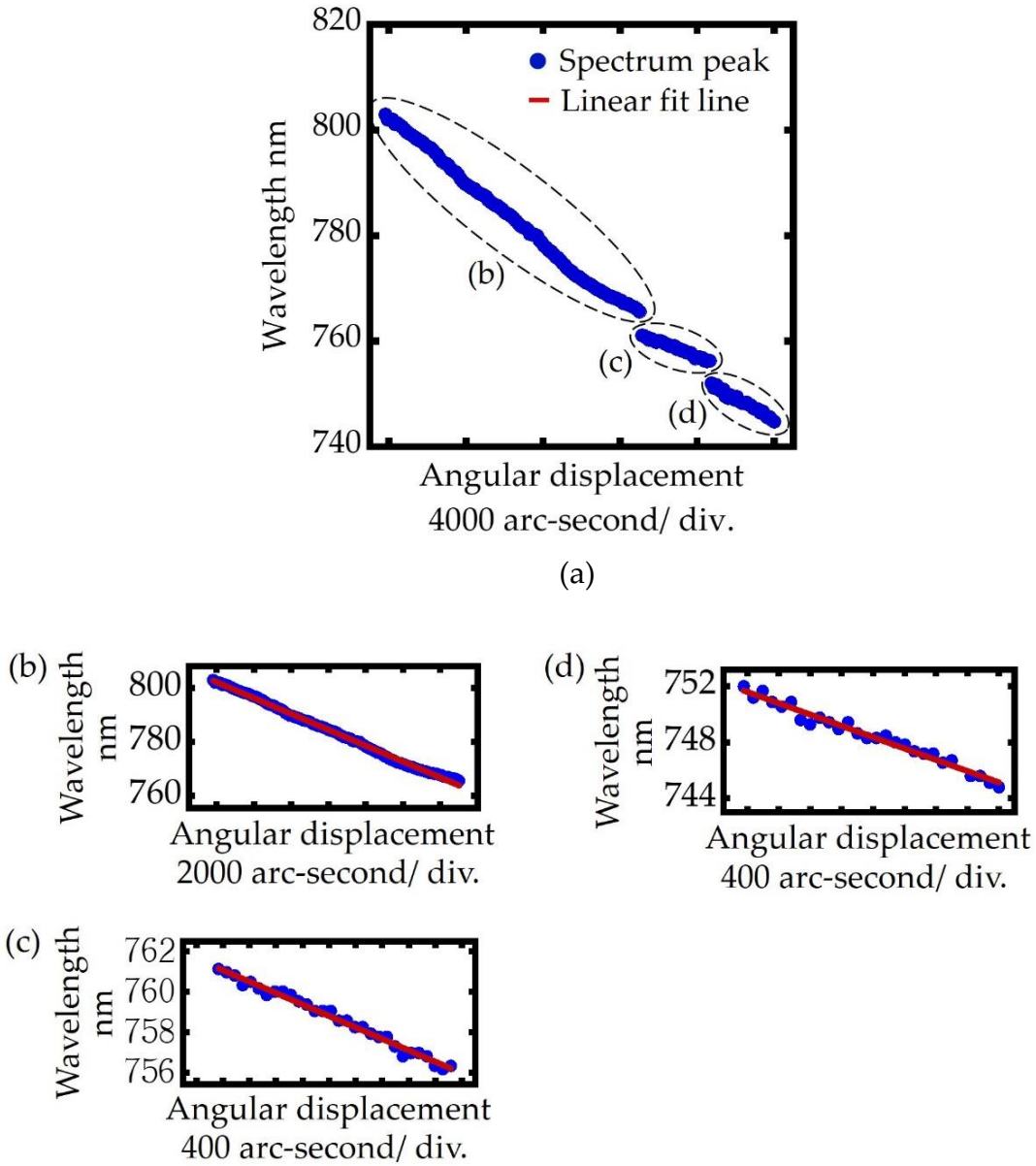

Figure 5.20 Angle measurement trend based on the peaks of SHG at the crystal position 50 mm; (**a**) the entire measurement trend line; (**b**) the most extended measurement area; (**c**) the middle range measurement area; (**d**) the least measurement area.

Figure 5.20 shows the measurement trend of the angle sensor at the crystal position of 50 mm, meanwhile Figure 5.21 shows the measurement trend at the crystal position of 70 mm. Three different sensitivities are detected as well in both crystal position with the identical measurement sensitivity in the most extended measurement area for both crystal position, that is 0.00294 nm/arc-second.

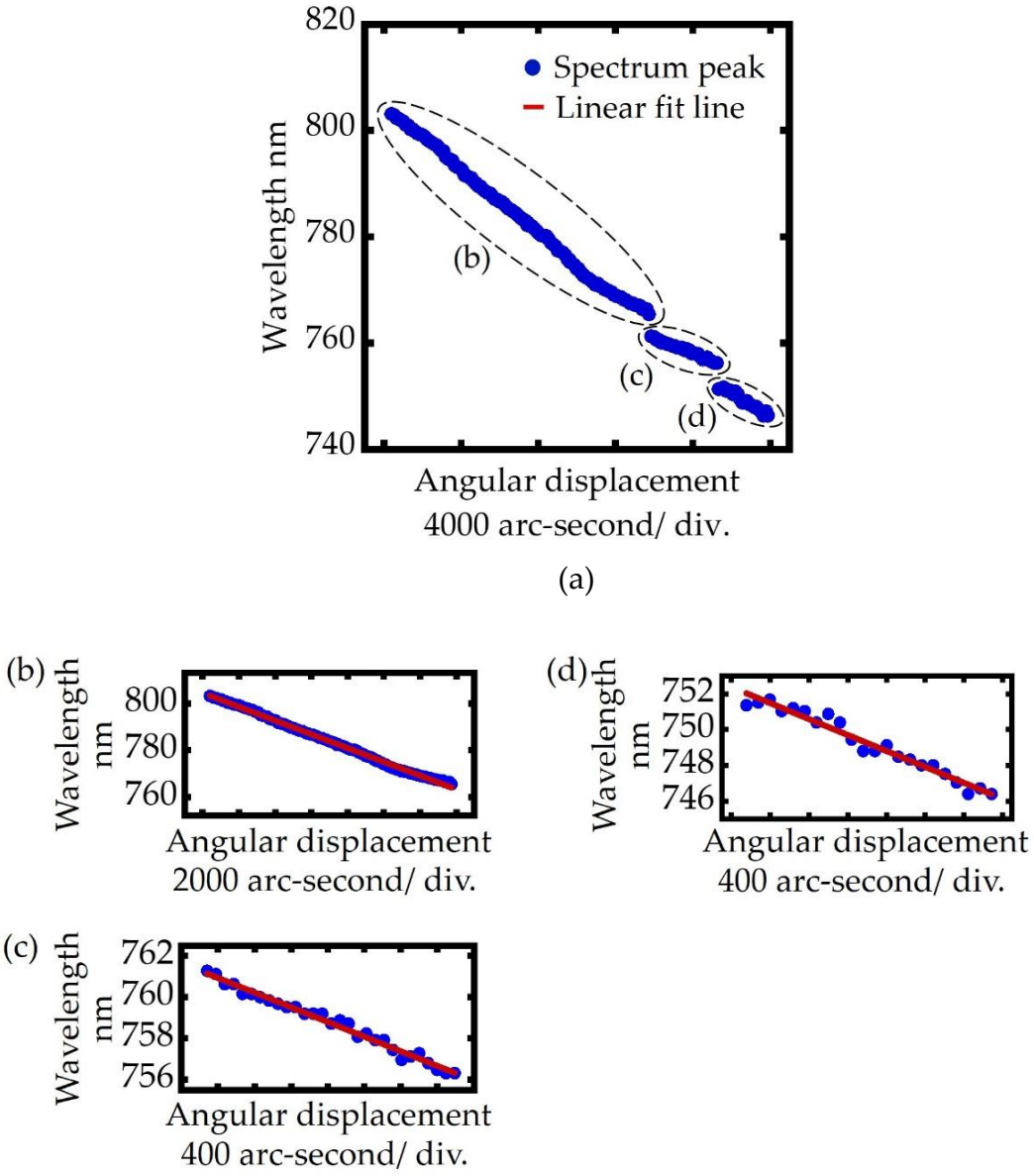

Figure 5.21 Angle measurement trend based on the peaks of SHG at the crystal position 70 mm; (**a**) the entire measurement trend line; (**b**) the most extended measurement area; (**c**) the middle range measurement area; (**d**) the least measurement area.

By considering the SHG peak only, the problem of intensity inconsistency at the crystal position variations mentioned earlier can be solved. The thorough measurement trend results from the experiment revealed different measurement trends compared to calculation results in Figure 5.7. The calculation could not confirm the measurement trend in the least intensity of localized SHG due to the very low efficiency in this range, therefore there is only two measurement sensitivity confirmed in the theoretical calculation.

The measurement trends in this study are tabulated in Table 5.3. The most extended measurement range of all crystal position changes showed identical sensitivity and resolution. In this area, the measurement target represented by the crystal position could be placed at any position along the collimated beam propagation direction. Meanwhile, the intensity was not steady throughout the experiment in areas with a lesser measurement range, resulting in inconsistent measurement sensitivity. The angle measurement range of 18998.31 arc-second, 19948.44 arc-second, and 19256.59 arc-second was achieved at the crystal position of 30 mm, 50 mm, and 70 mm, respectively. It is also noticed in Table 5.3 that the experiment results afforded lower measurement sensitivity but had wider angle range than that predicted in the calculation results. Ignoring the optical factor in the calculations was the main cause of the discrepancy. For example, it is assumed that the laser propagated through the air before entering the crystal, where the refractive index of the crystal is greater than that of air. The direction of Fs laser propagation could thus change when it enters the crystal. However, the difference in the refractive index was not taken into account in the calculation. The calculation can be modified by considering Snell's law, as has been reported in Chapter 4 [14]. Even so, Snell's law can only explain changes in the measurement sensitivity and angle range based on the measurement trend line. It cannot explain the difference in the contours of the SHG spectrum.

Taking closer identification in the measurement trend line, the split peak was the main cause of the measurement sensitivity discrepancy, as was shown in the calculation. Figure 12 displays an exemplification of the split peak. The single peak is also plotted in the figure for comparison. A split peak of the second harmonic wave spectrum appeared when the crystal was rotated by 6147.77 arc-second from its initial position. In contrast, only one peak appeared when the crystal was rotated by 6753.64 arc-second.

Table 5.3 Angle measurement result in several crystal positions

Crystal position mm	Peak wavelength range nm	Angle range arc-second	Sensitivity nm/arc-second	Resolution arc-second
30	765.44 – 802.88	13328.38	0.00294	6.80
	755.84 – 760.80	3506.75	0.00139	14.39
	747.04 – 751.04	2163.18	0.00185	10.81
50	765.60 – 802.88	13203.10	0.00294	6.80
	756.32 – 761.12	3499.81	0.00142	14.08
	747.84 – 752.00	3245.53	0.00202	9.90
70	765.44 – 803.20	13339.97	0.00294	6.80
	756.32 – 761.28	3382.52	0.00143	13.99
	746.40 – 751.36	2534.10	0.00223	8.97

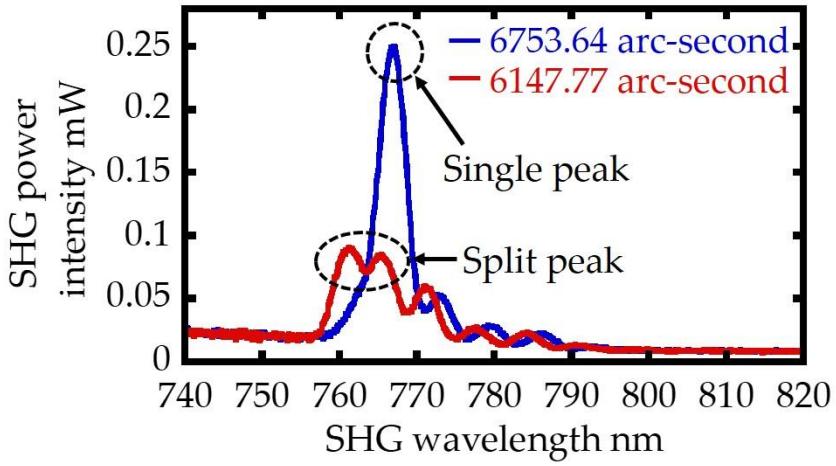

Figure 5.22 The comparison spectrum of the split peak and single peak area.

5.5 Summary

The optimization of the wavelength-dependent SHG angle sensor has been demonstrated in this chapter. The optimization is done by employing the collimated beam with a higher power as the laser source and verifying the feasibility of the proposed angle sensor to overcome the problem of target misalignment along the beam propagation direction, the Z-axis. The calculation evaluation for the proposed

configuration is done to predict the measurement tendency using the plane-wave approximation scheme. The result shows the discrepancy in the measurement trend due to the presence of a split peak. Two different measurement sensitivities with respective angles and wavelength ranges are detected by the calculation.

In the experiment, intensifying the collimated beam by applying the Keplerian lenses configuration with a focal length of 75 mm and 150 mm successfully reduces the beamwidth to half of its initial beamwidth. The beam reduction becomes important since the second harmonic wave can only be generated by the sufficient laser power density that cannot be fulfilled by the initial femtosecond laser output. Hereafter, the angle detection is conducted by observing the SHG peak with respect to angular position change of the crystal around the phase matching angle of the wavelength range from 1480 nm to 1640 nm. In order to verify the feasibility of the angle sensor to overcome the problem of target misalignment along the Z-axis, the experiments have been conducted for several crystal positions: 30 mm, 50 mm, and 70 mm. It is confirmed that the most extended angle range of all crystal positions has an identical measurement sensitivity of 0.00294 nm/arc-second and resolution of 6.803 arc-second. Since the sensor has used the second harmonic waves transformation in the crystal, the angle sensor can offer configuration for non-contact inspection. In addition, this angle sensor is not limited by the type of target material, providing the advantage of overcoming problems that are often encountered in the use of conventional angle sensors.

5.6 References

1. Kumar, A.S.A.; George, B.; Mukhopadhyay, C. Technologies and applications of angle sensors: A review. *IEEE Sensors Journal* **2021**, *6*, 7195-7206.
2. Wan, B.F.; Zhou, Z.W.; Xu, Y.; Zhang, H.F. A theoretical proposal for a refractive index and angle sensor based on one-dimensional photonic crystals. *IEEE Sensors Journal* **2021**, *21(1)*, 331-338.
3. Hou, B.; Zhou, B.; Song, M.; Lin, Z.; Zhang, R. A novel single-excitation capacitive angular position sensor design. *Sensors* **2016**, *16*, 1196.

4. Kumar, A.S.A.; George, B. A noncontact angle sensor based on Eddy current technique. *IEEE Transactions on Instrumentation and Measurement* **2020**, *64(4)*, 1275-1283.

5. Brajon, B.; Lugani, L.; Close, G. Hybrid magnetic-inductive angular sensor with 360º range and stray-field immunity. *Sensors* **2022**, *22*, 2153.

6. Ripka, P.; Blažek, J.; Mirzaei, M.; Lipovský, P.; Šmelko, M.; Draganowá, K. Inductive position and speed sensors. *Sensors* **2019**, *20*, 65.

7. Li, R.; Zhou, M.; Konyakhin, I.; Di, K.; Lu, Y.; Guo, J.; Liu, Y. Cube-corner autocollimator with expanded measurement range. *Optics express* **2019**, *25*, 5.

8. Matsukuma, H.; Asumi, Y.; Nagaoka, M.; Shimizu, Y.; Gao, W. An autocollimator with a mid-infrared laser for angular measurement of rough surfaces. *Precision Engineering* **2021**, *67*, 89-99.

9. Peredes, F.; Herrojo, C.; Martin, F. Position sensors for industrial applications based on electromagnetic encoders. *Sensors* **2020**, *21*, 2738.

10. Li, X.; Ye, G.; Liu, H.; Ban, Y.; Shi, Y.; Yin, L.; Lu, B. A novel optical rotary encoder with eccentricity self-detection ability. *Review of Scientific Instrument* **2017**, *88*, 115005

11. Smith, S.T.; Seugling, R.M. Sensor and actuator considerations for precision, small machines. *Precision engineering* **2006**, *30*, 245-264.

12. Zhang, Z.; Yan, J.; Kuriyagawa, T. Manufacturing technologies toward extreme precision. *International Journal of Extreme Manufacturing* **2019**, *1*, 022001.

13. Matsukuma, H.; Madokoro, S.; Astuti, W.D.; Shimizu, Y.; Gao, W. A new optical angle measurement method based on second harmonic generation with a mode-locked femtosecond laser. *Nanomanufacturing and Metrology* **2019**, *2*, 187-198

14. Astuti, W.D.; Matsukuma, H.; Nakao, M.; Li, K.; Shimizu, Y.; Gao, W. An optical frequency domain angle measurement method based on second harmonic generation. *Sensors* **2021**, *21*, 670.

15. Boyd, R.W. *Nonlinear Optics*, 4rd ed.; Academic Press: San Diego, United States, **2020**; pp. 1-63.

16. Kato, N. Optical second harmonic generation microscopy' application to the sensitive detection of cell membrane damage. *Biophysical Reviews* **2019**, *3*, 399-408.

17. Nuriya, M.; Fukushima, S.; Momotake, A.; Shinotsuka, T.; Yasui, M.; Arai, T. Multimode two-photon imaging using a second harmonic generation-specific dye. *Nature Communications* **2016**, *7*, 11557.

18. Bonacina, L.; Brevet, P.F.; Finazzi, M. Harmonic generation at the nanoscale. *Journal of Applied Physics* **2020**, *127*, 230901.

19. Baskey, S.J.; Andreana, M.; Lanteigne, E.; Ridsdale, A.; Stolow A.; Schweitzer, M.E. Pre-clinical translation of second harmonic microscopy of meniscal and articular cartilage using a prototype nonlinear microendoscope. *Medical Imaging and Diagnostic Radiology* **2019**, *7*, 1800211.

20. Chen, X.; Sanchez G.N.; Schnitzer M.J.; Delp, S.L. Microendoscopy detects altered muscular contractile dynamics in a mouse model of amyotrophic lateral sclerosis, *Scientific Reports* **2020**, *10*, 457.

21. Hooper, S.C.; Kuppe, C.; Wang, D.; Wang, W.; Guan, J.; Odom, T.W.; Valev, V.K. Second harmonic spectroscopy of surface lattice resonances. *Nano Letters* **2019**, *19*, 165-172.

22. Aharon, H.; Shavit, O.; Galanty, M.; Salomon, A. Second harmonic generation for moisture monitoring in dimethoxyethane at a gold-solvent interface using plasmonic structures. *Nanomaterials* **2019**, *9*, 1788.

23. Dmitriev, V.G.; Gurzadyan, G.G.; Nikogosyan, D.N. *Handbook of Nonlinear Optical Crystals*, 3rd ed.; Springe: Berlin, Germany, 1999; pp. 5-66.

24. Sutherland, R.L. *Handbook of Nonliear Optics*, 2nd ed.; CRC Press; Boca Raton, United States, **2003**; pp. 55-74.

25. Zhu, H.; Wang, T.; Zheng, W.; Yuan, P.; Qian, L. Efficient second harmonic generation of femtosecond laser at 1 μm, *Optics Express* **2004**, *12*, 2150-2155.

26. Astuti, W.D.; Li, K.; Sato, R.; Matsukuma, H.; Shimizu, Y.; Gao, W. A second harmonic wave angle sensor with a collimated beam of femtosecond laser. *Appl. Sci.* **2022**, *12*, 5211.

Chapter 6
Conclusion

Conclusions from research on angle measurement based on SHG will be summarized in this section. As mentioned in Chapter 1, the main objective of this research is to develop a new method for detecting the angular displacement of the target which can overcome the problems commonly encountered in the use of conventional angle sensors, especially in angle sensors operating based on lasers and optical configurations.

Chapter 2

The concept of second harmonic generation (SHG) has been introduced in this chapter. SHG is one nonlinear optical phenomenon in which a fundamental wavelength interaction with nonlinear material can generate the second harmonic wave with doubled frequency. The basic equation of the generating second harmonic wave has been explained in this chapter too, in which the phase-matching condition is the important parameter related to the given wavelength. Since the phase-matching

can occur in the one angle matching for its respective wavelength, the Fs laser that contains a wide range of wavelengths is the suitable laser source for the proposed angle sensor instead of the monochromatic laser source. Based on that, the change in the SHG spectrum can be used to indicate the change of angular position of the target represented by NLO crystals. However, the NLO crystals have respective characteristics. Therefore, the theoretical evaluation of several NLO crystals is presented as well. With the given Fs wavelength from 1480 nm to 1640 nm, the negative uniaxial crystal, such as BBO, $LiIO_3$, and $MgO:LiNbO_3$ is evaluated to predict the measurement trend based on the phase-matching characteristic of the crystals. The results show that BBO has the dispersive angle of 0.08° between the phase-matching angle range from 19.85° to 19.93°, $LiIO_3$ has the dispersive angle of 1.50° between the angular positions of 20.55° and 22.05° from the optical axis of the crystal and $MgO:LiNbO_3$ has angular dispersion of approximately 2.87° between the angular positions of 48.50° and 51.37° from the optical axis of the crystal. The angular dispersion characteristics of the crystal are then used to choose the suitable NLO crystal employed in the proposed angle sensor.

Chapter 3

In this chapter, the intensity-dependent angle sensor based on SHG is proposed. The theoretical analysis has clarified that the BBO crystal is suitable for the proposed angle measurement method when a mode-locked femtosecond laser source having a spectrum ranging from 1580 to 1620 nm is employed. It has been demonstrated by theoretical analysis and experiment that a focused femtosecond laser beam is effective in realizing SHG-based angle measurement for a femtosecond laser source with a small power where the intensity of a collimated beam from such a femtosecond laser source is too small to make SHG. Experimental results with the developed measurement system have demonstrated the feasibility of the proposed angular measurement. Meanwhile, the sensitivity observed in the experiments is lower than that predicted in the theoretical calculation. Investigations have been carried out based

on ray tracing to clarify the discrepancy between the results of theoretical calculation and those of the experiments. It has been defined that chromatic aberration has been one of the leading root causes of these problems, considering the results of ray tracing and observed second harmonic spectra. It has also been clarified that the shorter focal length of the focusing lens has made the influence of chromatic aberration stronger and has made the effective crystal length L_{eff} shorter, resulting in the degradation of the sensitivity.

Chapter 4

In this chapter, a novel optical angle measurement method based on SHG in the wavelength-dependent measurement has been proposed utilizing the high peak power characteristics and wide spectral range of a femtosecond laser pulse, which can generate second harmonic waves over a wide spectral range. This method allows absolute angle measurement by measuring the SHG spectrum. In experiments, the MgO:$LiNbO_3$ is used in the angle sensor configuration due to its wide angle of dispersion and it has been proven the validity of using parabolic mirrors to overcome the chromatic aberration of the focused beam that causes localization of SHG in previous studies. The experimental results with the developed measurement system have shown the feasibility of the proposed angle measurement. In addition, it has been clarified that the difference in refractive index between air and nonlinear optical crystals must be taken into account. As a result, a measured range of 10,752 arcseconds and a measurement resolution of 3.00 arcseconds has been achieved. The proposed method is expected to be able to make reliable measurements of the tilt angle movement of the machine tool spindle as well as reliable geometric measurements, such as precise measurement of the workpiece surface profile.

Chapter 5

In this chapter, the optimization of the wavelength-dependent angle sensor based on SHG is discussed to improve the performance of the angle sensor based on the

second harmonic wave generated by the focused beam of the Fs laser. Since the focused beam laser limits the working distance of the angle sensor in which the measurement target must be placed in the focal point of the focused beam, and the misalignment in the Z-axis is likely to occur, the new configuration to solve the problem is proposed. The new configuration employs the collimated Fs laser beam with higher output power to generate SHG by emitting it into the MgO:$LiNbO_3$ with a similar measurement principle as the previously proposed angle sensor. With the assumption that the collimated beam has no significant properties change as it propagates, it gives the advantage of prolonging the working distance of the angle sensor. The theoretical calculation is conducted to predict the measurement trend of the angle sensor by using the plane wave approximation equation of SHG. The experiment was demonstrated at the various position of the crystal along the laser propagation direction Z-axis, 30 mm, 50 mm, and 70 mm. The results of all positioned crystals show a similar tendency with the appearance of three measurement trend lines with respective measurement sensitivity. A measurement sensitivity of 0.000294 nm/arc-second and a resolution of 6.80 arc-second was achieved in the most extended observable angle range at all crystal positioned variations on the Z-axis. It indicates that the proposed angle sensor can overcome the problem of target misalignment along the Fs laser propagation direction. The configuration of the angle sensor is suitable for non-contact inspection as well as not being limited by the type of material target, providing the solution to the problems encountered in the use of conventional angle sensors. For these reasons, the proposed angle sensor is expected to have many potential applications, especially in the inspection process in the manufacturing industry.

Acknowledgements

First and foremost. I would like to sincerely thank Professor Wei Gao, my supervisor, for his valuable guidance during my studies. I am honored to have been given the opportunity to join his Precision Nanometrology Laboratory. He inspired me in many ways, especially with his work attitude and passion for research. His support has contributed to my academic development, especially increasing my confidence in conducting independent and rigorous research. My doctoral research was an enjoyable experience with his skilled supervision and inspiring advice.

I would like to thank Professor Yuki Shimizu from Hokkaido University for his advice and supervision of my research, especially his assistance in writing the manuscript so that I can publish a high quality paper. I also appreciate and thank Professor Hiraku Matsukuma for his insights and assistance in my research, as well as his direction in leading a disciplined research life. I would like to sincerely thank the laboratory members who have already graduated, Xin Xiong, Chong Chen, Qiaolin Li, Kai Zhang and others, who cannot be mentioned one by one who have helped me adapt to the laboratory environment, especially during my early days in this laboratory, Lue Quan who has helped in preparation for graduation, as well as other lab members who made great contributions to my personal development during my studies. In addition, I would like to thank the Japanese ministry for financial support (MEXT scholarship).

I would like to express a special thanks to my parents, my sister, and my brother for their invaluable and irreplaceable support. Also, I am especially grateful to my husband, Prastowo Murti, for the love, patience and encouragement that has always been given to me to complete this long journey. He was the first to introduce me to Tohoku University and encourage me to pursue my dream in this laboratory. He had taken care of everything without complaining. His loyal support is greatly appreciated.

Lastly, I would like to thank the Tahsin community (Halida R., Farah W., M. Insan Kamil G., M. Izzat Nugraha, Alfiyandy H., Hanif S.R., and others), the mentoring community, and all alumni of Universitas Gadjah Mada in Sendai who always help me during my time in Sendai.

Sincerely,
Wijayanti Dwi Astuti
Sendai, Japan.

List of Publications

Journal Papers:

1. Hiraku Matsukuma, Shuhei Madokoro, **Wijayanti Dwi Astuti**, Yuki Shimizu, and Wei Gao. A new optical angle measurement on second harmonic generation with femtosecond laser for angle measurement. *Nanomanufacturing and Metrology* **2019**, *2*, 187-198.
2. **Wijayanti Dwi Astuti**, Hiraku Matsukuma, Masaru Nakao, Kuangyi Li, Yuki Shimizu, Wei Gao. An optical frequency domain angle measurement method based on second harmonic generation. *Sensors* **2020**, *21*, 670.
3. Kuangyi Li, **Wijayanti Dwi Astuti**, Ryo Sato, Hiraku MAtsukuma, Wei Gao. Theoretical investigation for angle measurement based on femtosecond maker fringe. *Appl. Sci.* **2022**, *12*, 3702.
4. **Wijayanti Dwi Astuti**, Kuangyi Li, Ryo Sato, Hiraku Matsukuma, Yuki Shimizu, and Wei Gao. A second harmonic wave angle sensor with a collimated beam of femtosecond laser. *Appl. Sci.* **2022**, *12*, 5211.

International Conference Presentations:

Wijayanti Dwi Astuti, Hiraku Matsukuma, Li Kuangyi, Yuki Shimizu, and Wei Gao. Angular measurement method utilizing second harmonic generation. *The 7th International Conference on Nanomanufaturing*, October 15-17th (2021), Xi'an, China.

Domestic Conference Proceedings:

Wijayanti Dwi Astuti, Shuhei Madokoro, Masaru Nakao, Hiraku Matsukuma, Yuki Shimizu, and Wei Gao. (2020). Theoretical investigation on second harmonic generation with femtosecond laser for angle measurement. *The Proceedings of Conference of Tohoku Branch*, 55, 161.